



**Michigan
Technological
University**

Michigan Technological University
Digital Commons @ Michigan Tech

Dissertations, Master's Theses and Master's Reports

2018

PHYSICOCHEMICAL, SPECTROSCOPIC PROPERTIES, AND DIFFUSION MECHANISMS OF SMALL HYDROCARBON MOLECULES IN MOF-74-MG/ZN: A QUANTUM CHEMICAL INVESTIGATION

Gemechis Degaga


Michigan Technological University, gdegaga@mtu.edu

Copyright 2018 Gemechis Degaga

Recommended Citation

Degaga, Gemechis, "PHYSICOCHEMICAL, SPECTROSCOPIC PROPERTIES, AND DIFFUSION MECHANISMS OF SMALL HYDROCARBON MOLECULES IN MOF-74-MG/ZN: A QUANTUM CHEMICAL INVESTIGATION", Open Access Dissertation, Michigan Technological University, 2018.
<https://doi.org/10.37099/mtu.dc.etr/571>

Follow this and additional works at: <https://digitalcommons.mtu.edu/etr>

 Part of the [Materials Chemistry Commons](#), and the [Physical Chemistry Commons](#)

PHYSICOCHEMICAL, SPECTROSCOPIC PROPERTIES,
AND DIFFUSION MECHANISMS OF SMALL HYDROCARBON MOLECULES IN
MOF-74-MG/ZN: A QUANTUM CHEMICAL INVESTIGATION

By

Gemechis D. Degaga

A DISSERTATION

Submitted in partial fulfillment of the requirements for the degree of

DOCTOR OF PHILOSOPHY

In Chemistry

MICHIGAN TECHNOLOGICAL UNIVERSITY

2018

© 2018 Gemechis D. Degaga

This dissertation has been approved in partial fulfillment of the requirements for the Degree of DOCTOR OF PHILOSOPHY in Chemistry.

Department of Chemistry

Dissertation Advisor: *Dr. Loredana Valenzano*

Committee Member: *Dr. Rudy L. Luck*

Committee Member: *Dr. Kathryn A. Perrine*

Committee Member: *Dr. Ravindra Pandey*

Department Chair: *Dr. Cary F. Chabalowski*

Table of Contents

List of figures.....	vi
List of tables.....	viii
Preface.....	ix
Acknowledgements.....	x
List of abbreviations	xi
Abstract.....	xii
1 Introduction.....	1
1.1 Metal-Organic Frameworks (MOFs).....	1
1.2 Synthesis of MOFs	2
1.3 MOFs: Technological and Industrial Applications	4
1.3.1 Gas Storage	4
1.3.2 Toxic Gas Sensing	6
1.3.3 Gas Mixture Separation	6
1.3.4 Heterogonous Catalysis	7
1.4 Motivation of the Dissertation.....	8
2 Computational Methods and Details.....	11
2.1 Born-Oppenheimer Approximation	11
2.2 Hartree-Fock Method	13
2.3 Density Functional Theory	15
2.3.1 The Kohn-Sham Formulation	18
2.3.2 Exchange-Correlation Functionals.....	20
2.3.3 Local Spin Density Approximation	20
2.3.4 Generalized Gradient Approximation.....	21
2.3 Hybrid Functionals.....	22
2.3.5 Self-consistent Scheme to the KS Equation.....	23
2.4 Basis set.....	24
2.4.1 Linear Combination of Atomic Orbitals	24
2.4.2 Basis Set Superposition Error	26
2.4.3 Plane-wave (PW) Method.....	27
2.4.4 Pseudo-potentials	29
2.5 Periodic Systems	30
2.6 Dispersion Correction.....	31

2.6.1	The Grimme Dispersion Correction.....	32
2.6.2	The vdW-DF Dispersion Correction.....	33
2.7	Normal Vibrational Modes in Molecules and Crystals	33
2.8	Climbing Image Nudged Elastic Band Method	36
3	Results: Binding Energies of Hydrocarbons Addressed via MOF-74-Mg/Zn Molecular Cluster Models.....	38
3.1	Introduction	38
3.2	Theoretical Models and Computational Details	39
3.3	PBC: Relaxed Bulk Structures	42
3.4	Molecular Cluster Models: Geometrical Orientation of Adsorbed C ₂ -C ₄ Molecules.....	44
3.5	Molecular Cluster Models: Binding Energies (BE) of Adsorbed C ₂ -C ₄ Molecules.....	46
3.6	Summary	49
4	Results: Heats of Adsorptions of Hydrocarbon Molecules Addressed via MOF-74- Mg/Zn Periodic Boundary Condition (PBC) Models	51
4.1	Introduction	51
4.2	Computational Methods and Models	52
4.3	PBC: Structural Orientation of Adsorbed Ethylene and Ethane	55
4.4	PBC: Binding Energies and BSSE Corrected <i>BE</i>	56
4.5	PBC: Heats of Adsorption of Ethylene and Ethane	58
4.6	PBC: Spatial Orientation of Adsorbed C ₂ , C ₃ , and C ₄ Molecules.....	59
4.7	Binding Energies (BE), BSSE Corrections, and Dispersion Contributions for C ₂ , C ₃ , and C ₄ Adsorbed in MOF-Mg/Zn.....	61
4.8	Effect of Lateral Interaction on the Choice of the Model, and Molecular Loading	66
4.9	Heat of Adsorptions (ΔH^0) for C ₂ , C ₃ , and C ₄	67
4.10	Summary	69
5	Results: Spectroscopic Properties of C ₁ -C ₂ Hydrocarbon Molecules.....	71
5.1	Introduction	71
5.2	Computational Methods and Models	73
5.3	Geometrical Features for Molecules in the Gas Phase and Framework.....	78
5.3.1	CH ₄ – Methane.....	78

5.3.2	C ₂ H ₂ – Acetylene	79
5.3.3	C ₂ H ₄ – Ethylene	81
5.3.4	C ₂ H ₆ – Ethane	82
5.4	Infrared Spectra for Molecules in the Gas Phase and in the Framework	84
5.4.1	CH ₄ – Methane.....	85
5.4.2	C ₂ H ₂ – Acetylene	87
5.4.3	C ₂ H ₄ – Ethylene	90
5.4.4	C ₂ H ₆ – Ethane	92
5.5	Summary	96
6	Results: Diffusion Properties of C ₁ -C ₂ Hydrocarbon Molecules in MOF-74-Mg....	98
6.1	Introduction	98
6.2	Computational Details.....	99
6.3	Results and Discussion.....	101
6.4	Summary	107
7	Summary and Future Perspectives.....	109
7.1	Summary	109
7.2	Future Perspective	111
	Appendix A Permission to use Figure 1.1	114
	Appendix B Permission to use Figure 1.2	115
	Appendix C Permission to use Figure 1.3	116
	Appendix D Permission to use Figure 1.4	117
	Appendix E Permission to use Figure 1.5.....	118
	Appendix F Permission to use materials in Chapter 3	119
	Appendix G Permission to use materials in Chapter 4	120
	Appendix H Permission to use materials in Chapter 5	121
	Bibliography	122

List of Figures

Figure 1.1 Simple SBUs in less complex MOF structures	2
Figure 1.2 Examples of synthesized porous MOFs structures.....	3
Figure 1.3 Iso-reticular structures of the MOF-5	5
Figure 1.4 CO ₂ /CH ₄ gas mixture separation in Mg-MOF-74.....	7
Figure 1.5 Publication trend for various application areas	9
Figure 2.1 Self-consistent field (SCF) scheme to solve the KS equation.	25
Figure 2.2 Comparison of the wave function and the Coulomb potential	29
Figure 3.1 A depiction of the 3D structure of bulk MOF-74-M.	41
Figure 3.2 3MB and 6MB cluster models.....	42
Figure 3.3 a) 3MB cluster loaded with one ethane molecule.....	43
Figure 3.4 Molecular Cluster: Molecular orientation	45
Figure 3.5 Molecular Cluster: Trend for the binding energies	50
Figure 3.6 Molecular Cluster: Trend for the dispersion contribution	50
Figure 4.1 C ₂ H ₆ adsorbed in MOF-74-Mg.....	55
Figure 4.2 PBC: Molecular orientation of adsorbed ethylene	56
Figure 4.3 Molecular orientation.	61
Figure 4.5 Dispersion contribution	66
Figure 4.6 Binding energies reported for the three loading cases.....	67
Figure 5.1 Individual general molecular arrangements	73
Figure 5.2 IR spectra: (a) CH ₄ in the range.....	86
Figure 5.3 IR spectra for C ₂ H ₄	89
Figure 5.4 IR spectra for C ₂ H ₆	93
Figure 6.1 Bulk structure of MOF-74-Mg a) cross-sectional view of the channels	100

Figure 6.2 Molecular spatial orientation	103
Figure 6.3 Diffusion mechanisms, (a) <i>M1a</i> refers to the diffusion mechanism.....	103
Figure 6.4 Diffusion profile of water molecule in pristine MOF-74-Mg	104
Figure 6.5 Diffusion profiles for the diffusion processes.	106
Figure 6.6 Diffusion mechanism M1b. (a) Diffusion from one open metal.	107
Figure 6.7 Diffusion profile comparison: pristine MOF cavity.	108

List of Tables

Table 3.1 Long range dispersion parameters for the atoms constituting	40
Table 3.2 A comparison of calculated lattice parameters	44
Table 3.3 Molecular Cluster: Interatomic distances.....	47
Table 3.4 Molecular Cluster: Interatomic distances (in Å) between the open metal	48
Table 3.5 Molecular Cluster: Binding energies	49
Table 4.1 Binding energy (BE), basis set superposition error correction to the BE	58
Table 4.2 PBC: Zero-point energy (ZPE), thermal correction (TC)	59
Table 4.3 PBC: Comparison between ethylene and ethane heats of adsorptions	60
Table 4.4 Interatomic distances between open metal sites.....	62
Table 4.6 Binding energy (BE), basis set superposition error (BSSE) correction	63
Table 4.7 Binding energy (BE), basis set superposition error (BSSE) correction	65
Table 4.8 Olefin/paraffin differential binding energies.	68
Table 4.9 Binding energies (BEBSSE), zero-point energy (Δ ZPE).....	68
Table 5.1 CH ₄ : Atomic distances (Å) and angles (°).....	74
Table 5.2 C ₂ H ₂ : Atomic distances (Å) and angles (°)	75
Table 5.3 C ₂ H ₄ : Atomic distances (Å) and angles (°)	77
Table 5.4 Intramolecular atomic distances (Å) for C ₂ H ₆	77
Table 5.5 Intramolecular angles (°) for C ₂ H ₆ the different molecular loadings	79
Table 5.6 Arrangement (distances (Å) and angles (°)).....	80
Table 5.7 Calculated (raw data), scaled (0.965), experimental vibrational modes	83
Table 5.8 Calculated (raw data) and scaled (0.965) vibrational modes	85
Table 6.1 Comparison of the calculated binding energies	102

Preface

This dissertation is submitted in partial fulfillment of the requirements for the Doctor of Philosophy degree in Chemistry. Density functional theory was used to explore the physicochemical adsorption, spectroscopic properties, and diffusion mechanisms of small hydrocarbon molecules in MOF-74-Mg/Zn. All the works in this dissertation were supervised by Dr. Loredana Valenzano in the Department of Chemistry at Michigan Technological University. The research that this dissertation is composed of has been published in three peer-reviewed papers with one additional manuscript recently submitted.

The work on MOFs' molecular cluster models in Chapter 3 is reproduced from the *Chem. Phys. Lett.* 2016, 660, 313-319 paper with the permission of ELSEVIER Publishing.

The work on MOFs' 3D periodic models in Chapter 4 is reproduced from the *Chem. Phys. Lett.* 2017, 682, 168-174 paper with the permission of ELSEVIER Publishing.

Chapter 5 on spectroscopic properties of hydrocarbon molecules in MOF-74-Mg is adapted from the *Theor. Chem. Acc.* 2018, 137:42 paper with the permission from Springer Publishing.

The work on diffusion properties of C₁-C₂ hydrocarbon molecules in MOF-74-Mg in Chapter 6 was done in collaboration with Dr. Kenneth M. Flurchick from North Carolina A&T University and submitted recently to Physical Review Letters from APS Publishing.

Acknowledgements

The successful completion of this dissertation would not have been possible without the help and support from numerous people.

First and foremost, I want to thank my advisor Dr. Loredana Valenzano. I am thankful for the opportunity to work in her group, for the consistent guidance, encouragement, and support during my graduate studies at Michigan Tech. I have been lucky to have an advisor who cares so much about my research work. Her passion toward research and optimistic attitude toward life will always encourage me throughout my future professional career and life endeavors.

I would like to thank Dr. Ravindra Pandey for allowing me to attend his weekly research group meetings which gave me the opportunity to present not only my research progress, which foster my presentation and communication skills, but also the opportunity to expand my scientific knowledge and curiosity thanks to many interesting discussions.

I would like to thank my PhD committee members Dr. Rudy L. Luck, Dr. Kathryn A. Perrine, and Dr. Ravindra Pandey.

I would like to thank all faculty and staff members in the Department of Chemistry at Michigan Tech for supporting and helping me during my graduate studies in one way or the other. Thank you for resolving every issue I encountered during my study and stay at Michigan Tech.

I would like to thank the Department of Chemistry and Graduate School at Michigan Tech for the Teaching and Research Assistant support and Finishing Fellowship, respectively.

I am thankful for the computational resources obtained through the use of Superior, a high-performance computing cluster at Michigan Technological University and Athena, a high-performance computing facility at North Carolina A&T University. Mainly, I would like to thank Dr. Flurchick for the generous opportunity to access Athena which allowed for the successful completion of the diffusion project.

Last but not least, I would like to thank my parents, brothers, and friends for always being supportive and for encouraging me at every step of my academic career and life. Special gratitude goes to my wife-to-be, Erica J. Anderson, for constant support throughout the struggles of life and for proof-reading my research papers and this dissertation.

List of abbreviations

B3LYP: Becke, 3-Parameter, Lee-Yang-Parr

BSSE: Basis Set Superposition Error

CI-NEB: Climbing Image-Nudge Elastic Band

DFT: Density Functional Theory

GGA: Generalized Density Approximation

LCAO: Linear Combination of Atomic Orbitals

LDA: Local Density Approximation

MOF: Metal-Organic Framework

PBC: Periodic Boundary Conditions

PBE: Perdew-Burke-Ernzerhof

PES: Potential Energy Surface

PW: Plan-Wave

UPP: Ultrasoft Pseudo-Potential

vdW-DF: van der Waals Density Functional

ZPE: Zero Point Energy

Abstract

In petroleum refining industries, the fracturing process allows for the cracking of long-chain hydrocarbons into a mixture of small olefin and paraffin molecules that are then separated via the energetically and monetarily demanding cryogenic distillation process. In an attempt to mitigate both energetic and capital consumptions, selective sorption of light hydrocarbons by tunable sorbents, such as metal-organic frameworks (MOFs), appears to be the most promising alternative for a more efficient gas separation process. MOFs are novel porous materials assembled from inorganic *bricks* connected by organic *linkers*. From a crystal engineering stand point, MOFs are advantageous in creating a range of microporous (0.2–2.0 nm) to mesoporous (>50 nm) void cavities, presenting unique opportunities for the functionalization of both the organic *linkers* and the void. Of significant importance is the MOF-74-M family (M = metal), characterized by a high density of open metal sites, that is not fully coordinated metal centers. This family of MOF is also known as CPO-27-M. MOF-74 have demonstrated more separation potential than other known MOFs and zeolites. Density functional theory (DFT), as implemented within a linear combination of atomic orbital (LCAO) approach, has been used to investigate the selective sorption of C₁-C₄ hydrocarbons in MOF-74-Mg/Zn. The study was first implemented by adopting a molecular cluster approach, and later by applying periodic boundary conditions (PBC). While both modellistic approaches agree in showing significant differences in binding energies between olefins and paraffins adsorbed at the MOFs' open metal sites, results reported at the molecular cluster level show underestimation when compared to those obtained at the PBC level. The use of PBC models allow for the correcting of binding energies for basis set superposition error (BSSE), molecular lateral interaction (LI), zero-point energy (ZPE), and thermal energy (TE) contributions. As such, results obtained at the PBC level are directly comparable to experimental calorimetric values (*i.e.*, heat of adsorptions). This work discusses, for the first time, the origin of the fictitious agreement between binding energies obtained with molecular clusters and experimental heats of adsorption, identifying its origin as due to compensation of errors. Spectroscopy studies based on the intensities and frequency shifts

with respect to the molecules in the gas phase are presented as a further investigation of the interaction of the small hydrocarbons (C_1 - C_2) with the open metal sites in MOF-74-Mg. In an attempt to provide a more comprehensive description of the behavior of the hydrocarbon molecules, results from diffusion mechanism studies are also presented. The investigations of the diffusion mechanisms are based on the use of climbing-image nudge elastic band (CI-NEB) simulations, coupled with van der Waals functional (vdW-DF) and ultra-soft pseudopotentials as implemented within the plane-wave (PW) DFT approach. The CI-NEB studies showed that paraffin molecules are more energetically favored to diffuse within and along the cavity of MOF-74-Mg with respect to their olefin counterparts.

1 Introduction

1.1 Metal-Organic Frameworks (MOFs)

In the last century, our civilization was mostly based on materials such as metals, metal alloys, composites, metal oxides, polymers, silicon, and concretes. However, the need for societal and technological advancement demands the development of exotic material properties which are parallel and serial in their operation; extensively functionalized in their structure, capable of allowing counting, sorting, and coding, environmentally green, and capable of robust electronic, thermal and chemical dynamics.¹⁻² Along with nano-materials, graphene based materials, 2D transition metal dichalcogenides (TMDCs) to mention a few, metal-organic frameworks (MOFs) have emerged among the most promising materials of the future.³⁻⁶

MOFs are novel one-, two-, and three-dimensional materials assembled from inorganic *bricks* connected by organic *linkers*. The inorganic *bricks* are metal-ions (alkaline earth, transitional metals and lanthanides) or metal-oxide ions while the organic *linkers* are mostly organic molecules with one or more N- or O-donor atoms. These particular atoms are common in molecules such as pyridyl and cyano groups, carboxylates, phosphonates, crown ethers, and polyamines (in particular those derived from benzene, imidazole and oxalic acid).⁷ From a crystal engineering stand point, MOFs are advantageous in creating a range of microporous (0.2-2.0 nm) to mesoporous (>50 nm) sized cavities, with easy functionalization of both the organic *linkers* and the void. MOFs can therefore exhibit interesting properties such as thermal stability, well-defined ordered structure, high surface area, easy synthesis process, functionalized void and moieties with other materials, and other wide ranging properties suited for electronic, physical, and chemical applications.⁸⁻⁹ Unlike other porous materials, such as zeolites, MOFs allow a high precision control of shape, size, and functionalization of either the inorganic joints or the connecting *linkers* during the synthesis process.¹⁰

During the last two decades, enormous promising research results have been reported on MOFs and the number of publications based on MOFs is exponentially ascending every year for all their possible applications. The construction, properties, and precision reaction for the MOFs synthesis have resulted in a new branch of chemistry called reticular chemistry; the chemistry of linking molecular building blocks by strong bonds to make extended crystalline porous 3D structures. This new chemical approach has resulted in the design of materials for which structures, compositions, and even properties can be predetermined. In particular, highly porous MOFs characterized by strong metal–oxygen–carbon bonds showing exceptionally large surface area and excellent gas uptake and storage, have been synthesized. In addition, they can be systematically varied and functionalized with predetermined structures.^{8, 11}

1.2 Synthesis of MOFs

The process of MOFs synthesis starts from the mixing of the primary building units (PBUs), the inorganic *bricks* and the organic *linkers*. The final structure and properties of the synthesized MOFs relies on the PBUs used during the synthesis process. However, the MOFs synthesis approach requires other important factors such as temperature, solvent, kinetics, pH, pressure, to be considered carefully.¹²⁻¹³ Several MOFs structures have been synthesized combining O- or N-donor molecules with several elements of the periodic table, mainly transition metals.^{12, 14-15}

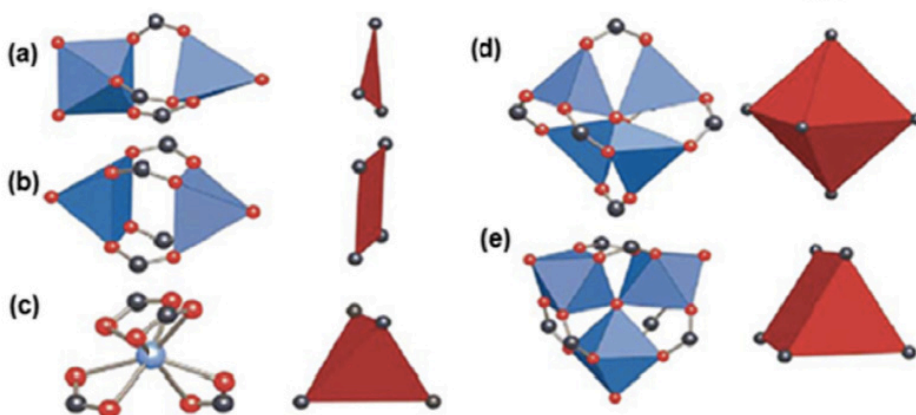


Figure 1.1 Simple SBUs in less complex MOF structures: (a) triangle, (b) square planar, (c) tetrahedron, (d) octahedron, and (e) trigonal prism (reprinted with permission from Ref. [8]. Copyright 2003; Springer Nature).

To make accurate pre-synthesis predictions of MOFs structures, the concept of SBUs has been adopted. The MOFs' material topology contains secondary building units (SBUs), consisting of a metal-oxide cluster at each joint in the MOFs' structure. Although, it is not easy to predict the MOFs' structure only on the basis of which PBUs were used.

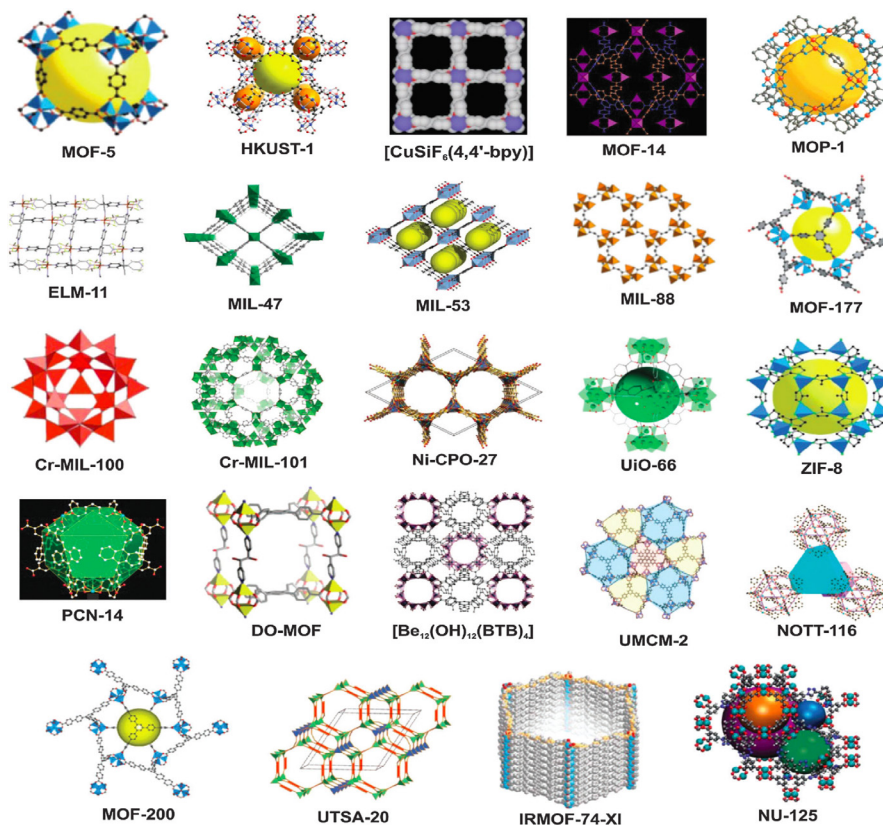


Figure 1.2 Examples of synthesized porous MOFs structures prepared by numerous research groups for various technological applications. (reprinted with permission from Ref. [6]. Copyright 2002; The American Association for the Advancement of Science).

The organic *linkers* play the role of connecting the SBUs in the MOFs assembly. The development of MOFs through the use and understanding of the SBUs has brought a new way of designing porous crystalline materials through molecular clusters.¹⁶ The SBUs take various shapes, for example triangles, squares, tetrahedrons and octahedrons. Figure 1.1 illustrates the simple SBUs for less complex MOFs geometrical structures. Numerous kinds of SBU connections with organic *linkers* have led to the synthesis of thousands of MOFs structures. This has led to the isolation of several highly porous MOFs structures over the years, of which some examples are reported in Figure 1.2.

The most striking property of MOFs is the functionality and tunability of their pores. The pore sizes are controlled by adjusting the length of the organic *linkers* connecting the SBUs. For example, Figure. 1.3 shows the iso-reticular structures of MOF-5 (IR-MOF-1) for twelve derivatives characterized by different pore sizes. All these structures have the same SBU ZnO_4 clusters connected by different linear dicarboxylic acids of different lengths, to form cubic lattices.

One of the most challenging task in MOFs synthesis is the preparation of extended (larger size) single crystals and ton-scale production, which mainly determine which synthetic method should be followed. The final application and functionality of MOFs is tailored employing several distinct synthetic procedures. However, industrial-level synthesis prefers faster and energy efficient approaches. The most common MOFs synthesis techniques include: slow diffusion, hydro(solvo)thermal, electrochemical, mechano-chemical, micro-wave assisted heating, ultrasonic, and one-pot. The details of each technique and the advantages and disadvantages associated with them, go beyond the scope of this work but can be found in the literature.^{6,9}

1.3 MOFs: Technological and Industrial Applications

MOFs unique structural properties (porosity, surface area, and pore size), and wide chemical functionality have brought them to the attention of researchers in both academia and industry. In the following subsections, the most promising applications of MOFs are briefly presented.

1.3.1 Gas Storage

The storage and/or transportation of molecular gaseous species of technological and environmental importance such as hydrogen (H_2), methane (CH_4), and carbon dioxide (CO_2) are among the most challenging tasks faced by chemists today. H_2 is the most environmentally clean and high energy density fuel. In recent years, improvements in the performance of hydrogen-fueled vehicles and H_2 energy-based technologies have relied on new materials able to guarantee more competitive hydrogen uptake and kinetics. In

addition, properties such as the capability of recharging and discharging at ambient temperatures and relatively low pressures are, ideally, expected to be attained.¹⁷⁻¹⁸

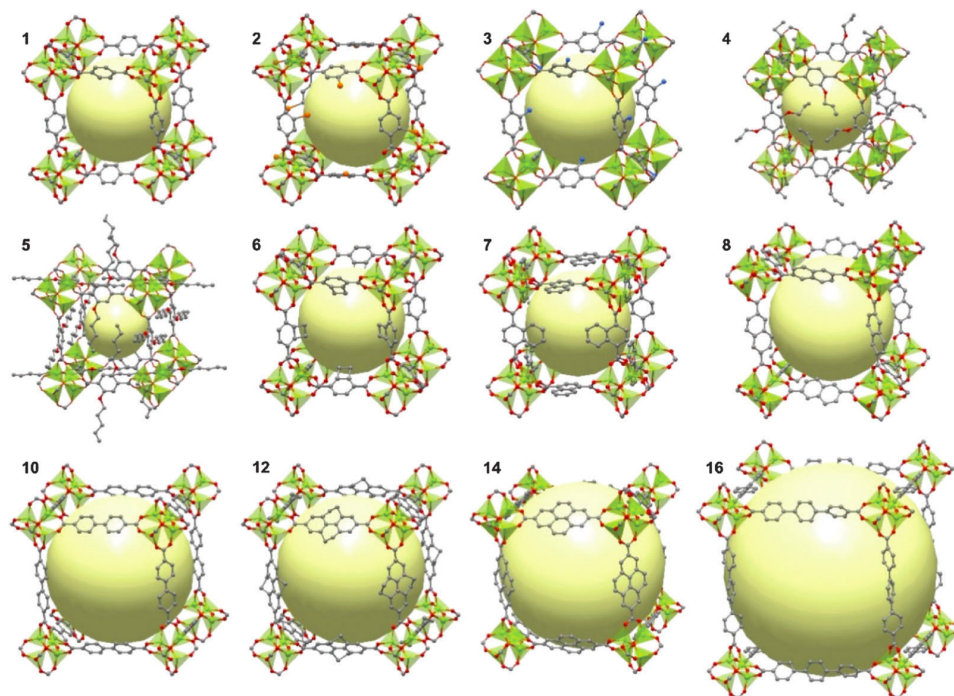


Figure 1.3 Iso-reticular structures of the MOF-5. The IR-MOF-5 family is prepared using organic molecules derived from different linear dicarboxylic acids. The linkers differ in functionality of the pendant groups, with the later expansion resulting in the increase of the IR-MOF-5 internal void space. The large yellow spheres represent the void cavities of the frameworks (reprinted with permission from Ref. [18]. Copyright 2002; The American Association for the Advancement of Science).

Despite extensive research on metal-hydrides, various carbon-based porous systems and zeolites, none were able to meet the standards set by the Department of Energy (DOE) for H₂ storage and transportation applications due to their associated high costs, low weight uptake, inadequate kinetic properties, and susceptibility to contamination. In contrast, several works have shown that MOFs are the most promising porous alternative materials for H₂ storage and transportation.¹⁹⁻²⁰

With fast energy combustion conversion and because of its abundance, natural gas (CH₄) is also ranked as one of the cleanest fuels. The means of storing CH₄ however, have been challenging due to the aspiration of finding inexpensive, safe, and convenient ways to storage it. Recently though, MOFs have shown considerable potential with respect to CH₄ storage.

Carbon dioxide (CO₂) is environmentally harmful, and dramatically contributes to greenhouse effect. The development of efficient materials for CO₂ capture and sequestration has been an active field of research. Due to their larger surface area, several MOFs have been designed to be used for CO₂ capture and storage.²¹⁻²²

1.3.2 Toxic Gas Sensing

Large quantities of environmentally harmful compounds are expelled from various industrial chemical processes, combustion of natural gas, deliberate emission of chemical warfare species, and use of fungicides in agriculture practices. Among others, NO_x, CO_x, H₂S, NH₃, PH₃, and volatile organic compounds (VOCs) are the most common.²³ In addition to atmospheric and environmental effects, human exposure to hazardous chemicals result in the manifestation of health related issues, such as severe disorder of the respiratory and sensory systems, cancer, endocrine system diseases, and disruption of the nervous system.²⁴ In this perspective some MOFs have emerged as ideal materials for sensing and removing toxic and hazardous molecules from the environment. In particular, recent investigations have reported on functionalized MOFs structures with uncommon sensing properties toward toxic gas removal.^{6, 25-26}

1.3.3 Gas Mixture Separation

The use of MOFs as selective gas mixture separation sieves and adsorption-desorption separating materials, has attracted wide interest at both technological and industrial level. Molecular separation methods imply selective gas separation based on the relative affinities of different chemical species with respect to the surfaces or adsorption sites provided by the chosen adsorbent materials.²⁷⁻²⁸ While the mixing of gases is a spontaneous process due to the second law of thermodynamics, gas mixture separation is not, and requires economically significant energy consumption. For this reason, research efforts devoted to the search, manufacture and use of alternative efficient and less expensive materials to tackle the separation task are currently of strategic importance. This includes looking for

alternative methods able to replace the current both energetically and monetarily inefficient and expensive cryogenic distillation and/or separation methods.²⁹

Among others, the removal of CO₂ for clean production of fuel gases such as natural gas is of paramount technological importance. An ideal material for such an application is required to preserve structure stability over many cycles. In addition, it requires an energy efficient discharge of CO₂ at the end of the separation process. The utilization of materials such as zeolites, amine solutions, and porous membranes resulted in inefficient and technologically inconvenient results. This negative outcome led researchers to use MOFs as a new class of materials for molecular gas separation applications. The work by *Britt et al.*, for example, has shown the extraordinary performance of MOF-74-Mg in purifying CH₄ by removing CO₂ (see Figure 1.4).³⁰

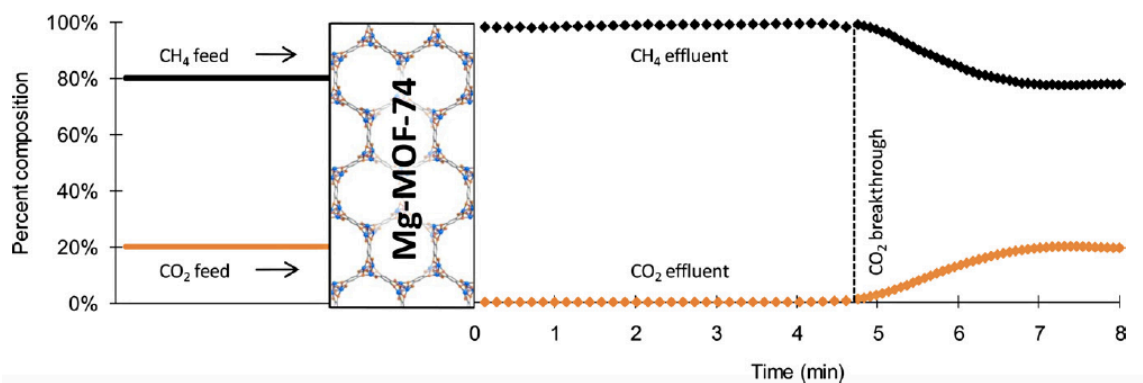


Figure 1.4 CO₂/CH₄ gas mixture separation in Mg-MOF-74, indicating complete retention of CO₂ until saturation. (reprinted with permission from Ref. [30] Copyright 2009; PNAS).

1.3.4 Heterogeneous Catalysis

Due to their porous functionality and structural similarity with zeolites, MOFs have attracted interest also for their potential use in heterogeneous catalysis.³¹⁻³² In addition, MOFs' large surface area, pores uniformity, active sites, channel sizes, and even robust structures under extreme conditions like those required by catalytic processes, have made them good alternative candidates for heterogeneous catalytic applications.²⁶ To ensure better catalytic activity, a MOF catalyst needs to fulfill several requirements. This would

include, but is not limited to, having unsaturated: open metal sites, functionalized organic linkers, large surface area, the potential to incorporate metal complexes into the organic linker and the pore, and the functionalization of organic *linkers*.³³ The design of catalytic MOFs and the enhancement of their catalytic activity are achieved mainly using two common strategies: (i) the encapsulation of metallic nano-particles or other compounds³⁴⁻³⁵ into the porous structures which would act as host matrices and (ii) post-synthetic modifications of the porous inner surface within the pore channel. Such design strategies have been used in recent catalytic applications of MOFs. For instance, some recent investigations have shown catalytic MOFs to be promising for aerobic oxidation of alcohols,³⁶ C–C coupling reactions,³⁷ CO to CO₂ oxidation,³⁸ and Knoevenagel condensation reactions.³⁹

Due to great tunability and chemical functionality of the *linkers* and the void, MOFs have also reached into other realms of technological and industrial applications such as luminescence, magnetism, drug delivery, and the textile industry. The overall publication trend for the last two decades (Figure 1.5) shows how in each field of research, MOFs have been getting more and more attention.⁹

1.4 Motivation of the Dissertation

In the petroleum refining industry, the separation of hydrocarbon mixtures into their various fractional components necessary for the production of fuels and chemical feedstocks is conducted at an enormous scale.⁴⁰ The fracturing step of the refining process results in hundreds of thousands of chemicals which vary in their percentage composition of hydrocarbons. Based on the various hydrocarbons' boiling points, petroleum is divided into its different fractional components such as butane and the lighter, gasoline, naphtha, kerosene, gas oil, and residues.⁴⁰

As previously mentioned, due to the high costs associated with many of the critical separation processes, which are mainly based on cryogenic fractional distillation, the design and synthesis of an energy efficient hydrocarbon gas mixture separation technology

is a field of active research interest. In this regard, MOFs are one of the most recent candidates for these specific application.^{29, 41-54} Their structural features, flexibility and versatility make them promising for selective separation of hydrocarbon gas mixtures, which is the topic of this dissertation.

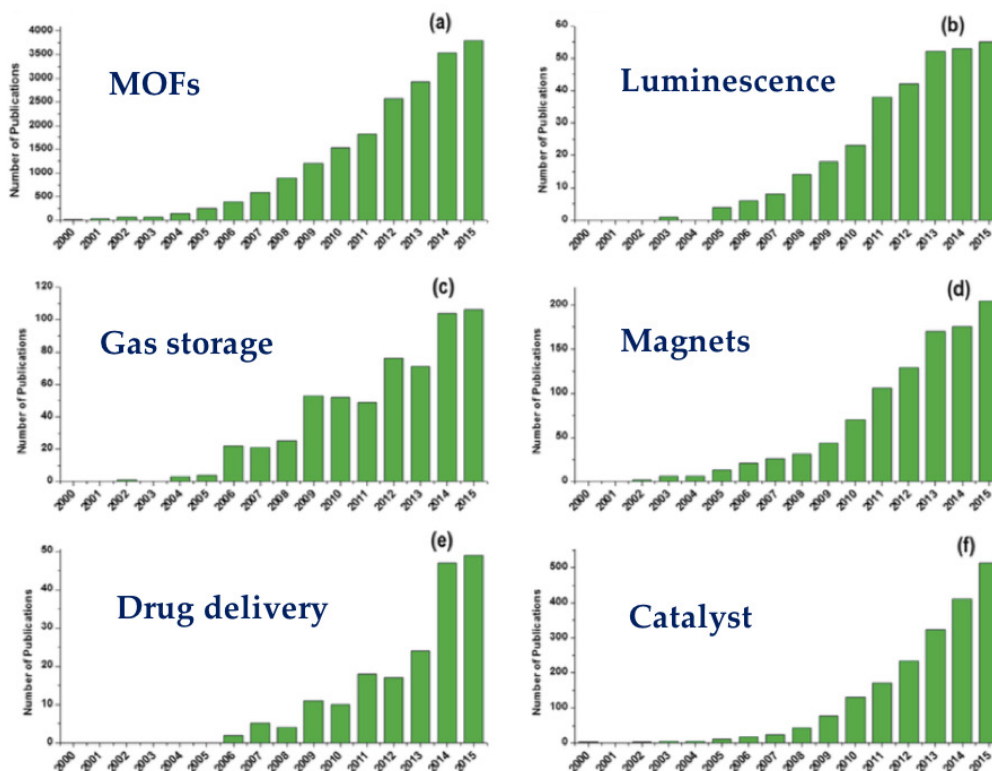


Figure 1.5 Publication trend for various application areas involving MOFs from 2000 to 2015. Application include (a) MOFs in general, (b) as luminescent materials, (c) for gas storage, (d) as magnets, (e) in drug delivery, and (f) in catalysis (reprinted with permission from Ref [9]. Copyright 2016; Springer Nature).

Several computational studies have recently addressed the adsorption of small molecules (H_2 , CO , N_2 , CO_2 , H_2O , H_2S , NH_3 , CH_4 , etc.) at the MOF-74-M open metal site(s) ($M=Mg$, Zn , Fe , Co , Ni , etc.).⁵⁵⁻⁵⁹ The computational investigation of these materials for the separation of light hydrocarbons however, is still in its infancy. Several experimental studies were published recently on the interaction of C_1 - C_4 with MOF-74-Mg/Co/Fe/Ni,^{48, 60-62} but, in contrast not many computational reports. For example, MOF-74-Fe has been shown to be effective in the separation of light hydrocarbons with a difference in binding energies between ethylene and ethane on the order of 20 kJ/mol.⁶³⁻⁶⁴

Using density functional theory (DFT) as the tool of research, this dissertation has multiple objectives. From a *fundamental stand point*, it seeks to:

1. Identify the structural and thermodynamic nature of the interaction of C₁-C₄ molecules within the MOFs framework.
2. Address the extent to which the use of molecular cluster models adopted to approximate the periodic structure of crystalline MOFs material is reliable for the investigation of the sorption of molecules containing more than four atoms.
3. Investigate the spectroscopic properties of each molecule at the open metal sites in the MOF structures.
4. Study diffusion mechanisms of the hydrocarbon molecules within and along the cavity of the MOF structures.

From an *applied stand point*, this work provides an understanding of the difference in the selective sorption of MOF-74-Mg/Zn for the separation of C₁-C₄ mixtures.

This dissertation is organized as follows: Chapter 2 lays out the computational and theoretical fundamentals and application of DFT while Chapters 3 and 4 focus on molecular cluster and periodic boundary condition (PBC) models, respectively, to address structural and thermodynamic properties of the interaction of C₁-C₄ hydrocarbons (CH₄, C₂H₂, C₂H₄, C₂H₆, C₃H₆, C₃H₈, C₄H₈, and C₄H₁₀) with the host MOF-74-M (M=Mg, Zn) frameworks. Chapter 5 details the results from the study of the infrared (IR) spectra of methane, acetylene, ethylene, and ethane in MOF-74-Mg. In that chapter, the intensities and frequency shifts with respect to the molecules in the gas phase are described and discussed with respect to geometrical arrangements and structural modifications of the molecules adsorbed in the framework. Chapter 6 discusses the diffusion properties of C₁-C₂ hydrocarbons (CH₄, C₂H₂, C₂H₄, C₂H₆) within and along the cavity of MOF-74-Mg. Lastly, Chapter 7 presents conclusions along with future study perspectives for which this dissertation sets solid foundations.

2 Computational Methods and Details

First-principle density functional theory (DFT) was used to investigate the adsorption, spectroscopic properties, and diffusion mechanisms of C₁-C₄ hydrocarbons in MOF-74-Mg/Zn. Physicochemical adsorption and spectroscopic properties were addressed with the use of CRYSTAL14,⁶⁵ a linear combination of atomic orbital (LCAO) code. Molecular diffusion mechanisms were investigated with QUANTUM ESPRESSO,⁶⁶ a plane-wave (PW) code. DFT is an approximate ground-state theory that allows for the study of many-body systems.⁶⁷ In the past few decades, DFT has been very successful due to the availability of more accurate *exchange-correlation* functionals and more powerful and efficient computational resources. In this chapter, a description of the theoretical foundations and approximations used will be laid out.

2.1 Born-Oppenheimer Approximation

The *Born-Oppenheimer approximation* allows for simplifying the treatment of the electrons-nuclei mutual interaction in many-body systems.⁶⁸ For a many-body system of interacting nuclei and electrons, the total wave function of the system, Ψ_{total} , will depend upon the nuclear coordinates, \mathbf{R} , and the electronic coordinates, \mathbf{r} . For n electrons subjected to the potential energy of N nuclei, the Schrödinger equation states that

$$\mathbf{H}\Psi_{total}(\mathbf{R},\mathbf{r}) = E\Psi_{total}(\mathbf{R},\mathbf{r}) \quad (2.1)$$

where E is the total energy of the system. The Hamiltonian \mathbf{H} is the sum of the kinetic energy of the nuclei, \mathbf{T}_N , the Coulomb repulsion between nuclei, V_{NN} , the Coulomb attraction between nuclei and electrons, V_{eN} , the kinetic energy of electrons, \mathbf{T}_e , and the Coulomb repulsion between electrons, V_{ee} . These terms are given by

$$\begin{aligned} \mathbf{T}_N &= \sum_{k=1}^N \frac{\hbar^2}{2M_k} \nabla_k^2, \\ \mathbf{T}_e &= \sum_{i=1}^n \frac{\hbar^2}{2m_e} \nabla_i^2, \\ V_{NN} &= \frac{e^2}{2} \sum_{k \neq l} \frac{Z_k Z_l}{|\mathbf{R}_k - \mathbf{R}_l|}, \end{aligned}$$

$$V_{ee} = -\frac{e^2}{2} \sum_{i \neq j} \frac{1}{|\mathbf{r}_i - \mathbf{r}_j|}, \quad \text{and}$$

$$V_{eN} = -\frac{e^2}{2} \sum_{k=1}^N \sum_{i=1}^n \frac{Z_k}{|\mathbf{R}_k - \mathbf{r}_i|}$$

where M_k and m_e are the mass of k^{th} nucleus and of the electron, respectively. The Laplacian operators ∇_k^2 and ∇_i^2 are the second partial derivative with respect to \mathbf{R}_k (the k^{th} nuclear coordinate) and \mathbf{r}_i (the i^{th} electron coordinate), respectively.

The arduous problem of dealing with electrons and nuclei mutual interaction, is treated, within the *Born-Oppenheimer approximation* is solved by determining the wave functions in two simpler steps. First, the mass difference between electrons and nuclei is exploited in order to separate the problem into an electronic part for a fixed nucleus and a nuclear problem under an effective potential generated by the electrons. This treatment is also known as *adiabatic approximation*. Following this idea, the wave function of a given system is broken into its nuclear, $\phi(\mathbf{R})$, and electronic, $\psi_R(\mathbf{r})$, parts as

$$\Psi_{total}(\mathbf{R}_k, \mathbf{r}_i) = \phi(\mathbf{R})\psi_R(\mathbf{r}) \quad (2.2)$$

The main assumption is that the electronic part of the wave function is independent of the nuclear dynamics since $M_k \gg m_e$ such that

$$\nabla_R \psi_R(\mathbf{r}) \approx 0 \quad (2.3)$$

where ∇_R is the gradient with respect to the nuclear positions.

In the first step of the approximation, the electronic Schrödinger equation is solved, yielding the wave function $\psi_R(\mathbf{r})$, which depends solely on the positions of electrons

$$(T_e + V_{ee} + V_{eN})\psi_R(\mathbf{r}) = E(\mathbf{R})\psi_R(\mathbf{r}) \quad (2.4)$$

where $E(\mathbf{R})$ is now the potential energy surface (PES).

In the second step of the approximation, the obtained $E(\mathbf{R})$ is used again to solve the nuclear Schrödinger equation

$$(\mathbf{T}_N + \mathbf{V}_{NN} + E(\mathbf{R}))\phi(\mathbf{R}) = E\phi(\mathbf{R}) \quad (2.5)$$

2.2 Hartree-Fock Method

The Hartree theory allows for writing the total wave function of an N -particle system as the product of the particles' spin-orbitals⁶⁹

$$\Psi(\mathbf{X}_1, \mathbf{X}_2, \dots, \mathbf{X}_N) = \prod_i^N \phi_i(\mathbf{X}_i) \quad (2.7)$$

where the single-particle spin-orbitals are orthonormal

$$\int \phi_i(\mathbf{X}_1) \phi_j(\mathbf{X}_1) d\mathbf{X}_1 = \delta_{ij}, \quad \delta_{ij} = \begin{cases} 1, & \text{for } i = j \\ 0, & \text{for } i \neq j \end{cases} \quad (2.8)$$

and here the variable \mathbf{X} refers to both spatial (\mathbf{r}) and spin states (σ), that is $\mathbf{X} \equiv (\mathbf{r}; \sigma)$. The integral is equivalent to the sum of integrations in spatial coordinates over all the spin components. Although ingenious, the Hartree wave function is affected by a dramatic shortcoming: it fails to satisfy the required antisymmetric property which fermions must obey it, stating that a fermion wave function changes sign under odd permutations of the electronic variables.

The introduction of the concept of Slater determinant allows for the fulfillment of the proper form for the solution of the multi-electronic system. The Slater determinant is given by⁷⁰

$$\Psi(\mathbf{X}_1, \mathbf{X}_2, \dots, \mathbf{X}_N) = \frac{1}{\sqrt{N!}} \begin{vmatrix} \phi_1(\mathbf{X}_1) & \cdots & \phi_1(\mathbf{X}_N) \\ \vdots & \ddots & \vdots \\ \phi_N(\mathbf{X}_1) & \cdots & \phi_N(\mathbf{X}_N) \end{vmatrix} \quad (2.9)$$

In (2.9), all the components of a given column refer to the same spin-orbital, whereas all the components in the same row refer to the same electron. Due to the known properties of determinants, the exchange of two particles is equivalent to the exchange of two columns; this translates into a change of sign in the wave function. Moreover, if two rows are equal, the determinant is null. This property implies that all orbitals must be different and thus is consistent with the Pauli exclusion principle which states that no two or more identical electrons can take similar quantum states. The Hamiltonian of such a system is expressed as

$$H = \sum_i^N f_i + \sum_{i \neq j}^N g_{ij} \quad (2.10)$$

where the one-body operator f_i and the two-body operator g_{ij} are given, respectively, by

$$f_i = \frac{\nabla_i^2}{2} - \frac{Z}{r_i} \quad (2.11)$$

and

$$g_{ij} = \frac{1}{r_{ij}} \quad (2.12)$$

The expectation value of the Hamiltonian is then given by

$$\begin{aligned} \langle \Psi | H | \Psi \rangle = & \sum_i \phi_i^*(\mathbf{X}_1) f_i \phi_i(\mathbf{X}_1) d\mathbf{X}_1 + \sum_{i \neq j} \int \phi_i^*(\mathbf{X}_1) \phi_j(\mathbf{X}_2) g_{ij} [\phi_i(\mathbf{X}_1) \phi_j(\mathbf{X}_2) \\ & - \delta(\sigma_i, \sigma_j) \phi_j(\mathbf{X}_1) \phi_i(\mathbf{X}_2)] d\mathbf{X}_1 d\mathbf{X}_2 \end{aligned} \quad (2.13)$$

After proper mathematical manipulation,⁷⁰ the Hartree-Fock equation assumes the form

$$\mathbf{f}_k \phi_k(\mathbf{X}_1) + \mathbf{V}_H(\mathbf{X}_1) \phi_k(\mathbf{X}_1) + (\mathbf{V}_x \phi_k)(\mathbf{X}_1) = \varepsilon_k \phi_k(\mathbf{X}_1) \quad (2.14)$$

Equation (2.14) differs from the Hartree equation by the presence of an additional term known as the *exchange* term. The Hartree potential (*i.e.*, electrostatic potential from the electron density), V_H , the electron density, ρ , and the exchange potential term (corresponding to the exchange energy), $V_x \phi_k$, are given by

$$V_H(\mathbf{X}_1) = \sum_j \int \phi_j^*(\mathbf{X}_2) \mathbf{g}_{12} \phi_j(\mathbf{X}_2) d\mathbf{X}_2 = \int \rho(\mathbf{X}_2) \mathbf{g}_{12} d\mathbf{X}_2 \quad (2.15)$$

with

$$\rho(\mathbf{X}_2) = \sum_j \phi_j^*(\mathbf{X}_2) \phi_j(\mathbf{X}_2) \quad (2.16)$$

and

$$(\mathbf{V}_x \phi_k)(\mathbf{X}_1) = \sum_j \delta(\sigma_k, \sigma_j) \int \phi_j(\mathbf{X}_2) \mathbf{g}_{12} \phi_k(\mathbf{X}_2) \phi_j(\mathbf{X}_1) d\mathbf{X}_2 \quad (2.17)$$

For a quantum chemical system, the exchange energy is the energy difference between the Hartree energy and the true ground-state energy of the system. As an operator, the integral nature of the exchange term introduces considerable complexity which makes the Hartree-Fock equation (and the post Hartree-Fock methods thereof) extremely challenging to solve.

2.3 Density Functional Theory

In the last few decades, density functional theory (DFT) has gained huge momentum in describing the ground-state structural and electronic properties of many-body systems ranging from molecules to extended solids. DFT is fundamentally based on the concept of electron density. This makes it a more practical way of treating the ground-state of multi-electronic systems. The main character, in DFT, is the multi-electronic density, $n(\mathbf{r})$, rather than the wave function, as in Hartree-Fock based theories. As such, DFT substantially alleviates the arduous task of working with a $3N$ dimensional wave function; in fact now,

$n(\mathbf{r})$ which is a function of only three Cartesian coordinates is considered. The foundation of modern DFT is based on two fundamental theorems which were formulated in the 1960s by Hohenberg and Kohn.⁷¹⁻⁷²

First Hohenberg-Kohn Theorem: *The ground-state electron density, $n(\mathbf{r})$, of a many-body quantum system immersed in an external potential, $v(\mathbf{r})$, uniquely determines the potential.*

This theorem can be proved by *reductio ad-absurdum*, considering a many-electron Hamiltonian associated to a ground-state wave function, Ψ , given by

$$\mathbf{H} = \mathbf{T} + \mathbf{U} + \mathbf{V} \quad (2.18)$$

where \mathbf{T} is the kinetic energy, \mathbf{U} is the electron-electron interaction, and \mathbf{V} is the external potential operators. The electron density, $n(\mathbf{r})$, is defined as

$$n(\mathbf{r}) = N \int |\Psi(\mathbf{r}, \mathbf{r}_2, \mathbf{r}_3, \dots, \mathbf{r}_N)|^2 d^3\mathbf{r}_2 d^3\mathbf{r}_3 \dots d^3\mathbf{r}_N \quad (2.19)$$

For any other ground-state wave function, Ψ' , a different Hamiltonian

$$\mathbf{H}' = \mathbf{T} + \mathbf{U} + \mathbf{V}' \quad (2.20)$$

exists such that

$$\mathbf{V} - \mathbf{V}' \neq \text{constant} \quad (2.21)$$

Under the assumption that the two ground-state electron densities associated to the two different Hamiltonian are the same, the following relationships hold true

$$E' = \langle \Psi' | \mathbf{H}' | \Psi' \rangle < \langle \Psi | \mathbf{H}' | \Psi \rangle < \langle \Psi | \mathbf{H} + \mathbf{V}' - \mathbf{V} | \Psi \rangle \quad (2.22)$$

thus implying

$$E' < E + \int (n(v') - n(v))n(\mathbf{r})d\mathbf{r} \quad (2.23)$$

On the other hand,

$$E = \langle \Psi | \mathbf{H} | \Psi \rangle < \langle \Psi | \mathbf{H}' | \Psi \rangle < \langle \Psi | \mathbf{H} + \mathbf{V} - \mathbf{V}' | \Psi \rangle \quad (2.24)$$

that translated into

$$E < E' + \int (n(v) - n(v'))n(\mathbf{r})d\mathbf{r} \quad (2.25)$$

The addition of Equation 2.23 and Equation 2.25 gives

$$E' + E < E + E' \quad (2.26)$$

which is an absurd statement indicating that no two different potentials can share the same electron density.

Second Hohenberg-Kohn Theorem: *The ground-state energy, E , is uniquely determined by the ground-state electron density. The density that minimizes the total energy is the exact ground-state density.*

This is a straightforward consequence of the first theorem. In mathematical terms, E is a functional (function of electron density which in turn is a function of space, $n(\mathbf{r})$) given by

$$\begin{aligned} E[n(\mathbf{r})] &= \langle \Psi | \mathbf{T} + \mathbf{U} + \mathbf{V} | \Psi \rangle = \langle \Psi | \mathbf{T} + \mathbf{U} | \Psi \rangle + \langle \Psi | \mathbf{V} | \Psi \rangle \\ &= F[n(\mathbf{r})] + \int n(\mathbf{r})v(\mathbf{r})d\mathbf{r} \end{aligned} \quad (2.27)$$

Having proved that $n(\mathbf{r})$ determines $v(\mathbf{r})$, which in turn determines the Hamiltonian \mathbf{H} associated to the ground-state wave function Ψ , implies that Ψ is a functional of $n(\mathbf{r})$. Therefore, the expectation value of any arbitrary operator \mathbf{F} is

$$\langle \Psi | \mathbf{F} | \Psi \rangle = F[n(\mathbf{r})] \quad (2.28)$$

A density that is the ground-state of some external potential is known as *v-representable*.⁷²

As a consequence, a *v-representable* energy functional $E[n(\mathbf{r})]$ can be defined as

$$\begin{aligned} E_v[n'(\mathbf{r})] &= \int n'(\mathbf{r})v(\mathbf{r})d\mathbf{r} + F[n'(\mathbf{r})] \\ &= \langle \Psi' | \mathbf{F} + \mathbf{V} | \Psi' \rangle \end{aligned} \quad (2.29)$$

where $v(\mathbf{r})$ is the external potential.

The application of the variational principle provides⁷³

$$\langle \Psi' | \mathbf{F} + \mathbf{V} | \Psi' \rangle > \langle \Psi | \mathbf{F} + \mathbf{V} | \Psi \rangle \quad (2.30)$$

that is,

$$\int n'(\mathbf{r})v(\mathbf{r})d\mathbf{r} + F[n'(\mathbf{r})] > \int n(\mathbf{r})v(\mathbf{r})d\mathbf{r} + F[n(\mathbf{r})] \quad (2.31)$$

which allows for stating the second Hohenberg-Kohn theorem as

$$E_v[n'(\mathbf{r})] > E_v[n(\mathbf{r})] \quad (2.32)$$

2.3.1 The Kohn-Sham Formulation

The practical application of DFT was made possible by the formulation developed by Kohn and Sham (KS), which maps the system of interacting electrons as a fictitious system of non-interacting electrons sharing the same ground-state electron density, $n(\mathbf{r})$. Such density is expressed as a sum over the one-electron KS orbitals $\psi_i(\mathbf{r})$ ⁷¹

$$n(\mathbf{r}) = \sum_{i=1}^N |\psi_i(\mathbf{r})|^2 \quad (2.33)$$

These KS orbitals are the solution to the one-electron KS equation, which resembles the Schrödinger equation

$$\left(-\frac{\hbar^2}{2m_e}\nabla^2 + V_{KS}(\mathbf{r})\right)\psi_i(\mathbf{r}) = \varepsilon_i\psi_i(\mathbf{r}) \quad (2.34)$$

where m_e is the mass of an electron and ε_i is the orbital energy of the corresponding KS orbital, ψ_i . The orbitals are required to be orthonormal, that is

$$\int \psi_i^*(\mathbf{r})\psi_j(\mathbf{r})d\mathbf{r} = \delta_{ij} \quad (2.35)$$

The KS potential V_{KS} is unique and exists as a consequence of the Hohenberg and Kohn theorems.⁷¹⁻⁷² In fact, such a potential always exists, and its formulation is always valid regardless of the form the electron-electron interactions characterizing the system of interest takes on. The KS potential (also commonly known as the effective potential) is given by

$$V_{KS}(\mathbf{r}) = V_H(\mathbf{r}) + V_{ex}(\mathbf{r}) + V(\mathbf{r}) \quad (2.36)$$

The corresponding KS Hamiltonian (H_{KS}) takes the form

$$H_{KS} = -\frac{\hbar^2}{2m_e}\nabla^2 + V_H(\mathbf{r}) + V_{ex}(\mathbf{r}) + V(\mathbf{r}) \quad (2.37)$$

where the Hartree and *exchange-correlation* potential are expressed as

$$V_H(\mathbf{r}) = e^2 \int \frac{n(\mathbf{r}')}{|\mathbf{r} - \mathbf{r}'|} d\mathbf{r}' \quad (2.38)$$

and

$$V_{ex}[n(\mathbf{r})] = \frac{\delta E_{ex}}{\delta n(\mathbf{r})} \quad (2.39)$$

respectively, and where E_{ex} is the *exchange-correlation* energy functional. Approximations to the common *exchange-correlation* energy functionals are discussed in the following subsections.

2.3.2 Exchange-Correlation Functionals

DFT is, in principle, an exact and complete theory. However, though all the functional terms in the KS formalism can be expressed and calculated explicitly, there is no complete expression for the *exchange-correlation* energy functional.⁷² As a consequence, different approximations have been proposed to use DFT as a practical tool for *first-principle* electronic structure calculations.⁷⁴ In the following three subsections, the original and most frequently used approximations to the *exchange-correlation* functional will be discussed.

2.3.3 Local Spin Density Approximation

The first (and simplest) approximation for the *exchange-correlation* energy to have been developed was the local spin density approximation (LSDA).⁷² LSDA depends on the electron density at each point in space and is derived from the homogeneous electron gas (HEG) model.^{71, 75} Within this approximation, the treatment of magnetic material (spin polarized systems) is made by considering each electron spin state density ($n^\alpha(\mathbf{r}), n^\beta(\mathbf{r})$). LSDA functional takes the form

$$E_{xc}^{LSDA}[n^\alpha(\mathbf{r}), n^\beta(\mathbf{r})] = \int \varepsilon_{xc}^{hom}(n^\alpha(\mathbf{r}), n^\beta(\mathbf{r}))n(\mathbf{r})d\mathbf{r} \quad (2.40)$$

where ε_{xc}^{hom} is the *exchange-correlation* energy of the homogeneous electron gas given by

$$\varepsilon_{xc}^{hom}(n(\mathbf{r})) = -\frac{3}{4\pi}(3\pi^2n(\mathbf{r}))^{\frac{1}{3}} \quad (2.41)$$

where the relative spin-polarization is introduced as

$$\zeta(\mathbf{r}) = \frac{n^\alpha(\mathbf{r}) - n^\beta(\mathbf{r})}{n(\mathbf{r})}, \quad n(\mathbf{r}) = n^\alpha(\mathbf{r}) + n^\beta(\mathbf{r}) \quad (2.42)$$

The case $\zeta=0$ corresponds to a paramagnetic spin-unpolarized situation where the two electron spin densities are equal while $\zeta = \pm 1$ correspond to the ferromagnetic spin-polarized situation, where one of the spin densities disappears. The potential corresponding to the *exchange-correlation* energy is given by Equation 2.39.

Although LSDA has resulted in a good description of the atomic structure and elastic and vibrational properties for a wide range of systems, it is generally not accurate enough to describe the energetics of chemical reactions and binding energies.⁷⁶⁻⁷⁷ In fact, the electron density is not necessarily uniformly dependent on the spatial positions as generally assumed in the formulation of LSDA functionals. Thus, this approximation is not a useful choice for systems in which the uniform electron density does not represent a reliable assumption.

2.3.4 Generalized Gradient Approximation

The generalized gradient approximation (GGA) represented the first attempt to overcome the limitations of LSDA.⁷⁴ In fact, these functionals depend on both the density and its local variation and are generally expressed as

$$E_{xc}^{GGA}[n] = \int \varepsilon_{xc}^{hom}(n(\mathbf{r}), \nabla n(\mathbf{r})) n(\mathbf{r}) d\mathbf{r} \quad (2.43)$$

GGA showed a considerable improvement over LSDA in describing energy barriers and dissociative adsorptions, although, it is still limited to achieve desirable chemical accuracy.⁷⁸⁻⁷⁹

Meta-GGA functionals add on to GGA by depending not only on the local electron density (as in LSDA) and on the gradient of the density (as in GGA), but also on the Laplacian of the density, $\nabla^2 n(\mathbf{r})$, also known as the Kohn-Sham kinetic energy density⁸⁰

$$\tau(\mathbf{r}) = \frac{1}{2} \sum_{i=1}^N |\nabla \psi_i(\mathbf{r})|^2 \quad (2.44)$$

Therefore, meta-GGA functionals are generally written as

$$E_{xc}^{MGGA} = \int \varepsilon_{xc}^{hom}(n(r), \nabla n(r), \nabla^2 n(r), \tau(r)) n(r) dr \quad (2.45)$$

Meta-GGA functionals have shown the ability to predict more accurately band gaps, binding energies, and reaction coordinates for a wide range of systems.⁸¹⁻⁸³

2.3 Hybrid Functionals

Hybrid functionals capture more non-local dependence by incorporating the non-local HF exchange which makes them more accurate than meta-GGA.^{74, 84} These are the most extensively used class of approximations where the exchange part of the exchange-correlation energy functional is a mixture of a portion of exact-exchange from Hartree–Fock (E_x^{HF}) theory and exchange contribution coming from ab-initio or empirical DFT (E_x^{DFT}). The correlation part of the exchange-correlation energy is a portion of the DFT correlation (E_c^{DFT}). Generally, such functionals are given in the form

$$E_{xc}^{Hybrid} = aE_x^{HF}[\{\psi_i\}] + (1 - a)E_x^{DFT} + aE_c^{DFT} \quad (2.47)$$

The most commonly used hybrid functionals include B3LYP⁸⁵ and PBE⁸⁵⁻⁸⁶. For example, the B3LYP exchange-correlation energy term is expressed as

$$E_{xc}^{B3LYP} = (1 - a)E_x^{LDA} + aE_x^{HF} + b\Delta E_x^{B88} + (1 - c)E_c^{LDA} + cE_c^{LYP} \quad (2.48)$$

where $a = 0.20$, $b = 0.72$, and $c = 0.80$. The E_x^{B88} and E_c^{LYP} are Becke’s 1988 exchange functionals, and Lee Yang and Parr’s correlation functionals, respectively.⁸³

PBE⁸⁷ functionals generally mix the Perdew-Burke-Ernzerhof (PBE) exchange energy and the exact Hartree-Fock exchange energy. For example, for PBE0 (the simplest form of PBE), the ratio of HF exchange to PBE exchange (a:b) is 1 to 3. The correlation part of PBE0 is a fully PBE correlation energy functional, E_c^{PBE} , given by

$$E_{xc}^{PBE0} = aE_x^{HF} + bE_x^{PBE} + E_c^{PBE} \quad (2.49)$$

Hybrid functionals constitute the biggest family of approximations ever developed for the quantum mechanical description of electrons in molecules and materials. Among the most recent and most successful developments, one of the frequently used semi-empirical hybrid *exchange-correlation* functionals, based on meta-GGA, is provided by the M06⁸⁸ family of functionals. These meta-hybrid GGA functionals are constructed based on various functional forms parametrized from high-quality benchmark molecular databases. M06 generally gives good results for systems containing dispersion forces, which amends one of the biggest deficiencies of standard DFT methods.

2.3.5 Self-consistent Scheme to the KS Equation

From a practical stand point, when DFT calculations are performed, the Kohn-Sham equation is solved *self-consistently*. The term means that the calculation starts with a guessed value of the electron density, (\mathbf{r}) , that is used to construct the effective KS potential. A KS equation (Equation 2.34) is then solved to obtain the energy eigenvalues, ϵ_i , and KS eigenstates, (\mathbf{r}) . The electron density is subsequently evaluated to check if the convergence criteria are achieved. Convergence is said to be achieved when the newly obtained (\mathbf{r}) is numerically the same with respect to the one used to construct the previously effective KS potential. If convergence is not achieved, the effective potential is reevaluated based on the new electron density in replacement of the value of the electron density during the previous step, and the diagonalization of the KS equations is performed again. This iteration loop is repeated until the convergence criteria are satisfied. The electronic properties of the system are then calculated based on the ground-state electron density (\mathbf{r}) .

This iterative procedure for the computation of the ground-state electron density is usually called the self-consistent field (SCF) method. Figure 2.1 shows the schematic diagram of the described SCF scheme.

2.4 Basis set

In computational chemistry, basis sets are used to transform the original integro-differential problem into a more solvable algebraic form.⁸⁹ In the study of quantum mechanical systems, a quantum state is an element belonging to an infinite-dimensional vector-space. Elements of a vector space can be built as a linear combination of basis vectors. For a given state $\psi_n(\mathbf{r})$, an infinite number of basis sets are required to represent it properly. The basis set is said to be complete if any element of the space can be written as a linear combination of basis vectors.^{72, 89}

2.4.1 Linear Combination of Atomic Orbitals

In the linear combination of atomic orbitals (LCAO) approach⁸⁹, the wave function is expressed as the sum of atomic orbitals (AOs), χ_i

$$\psi(\mathbf{r}) = \sum_i c_i \chi_i \quad (2.49)$$

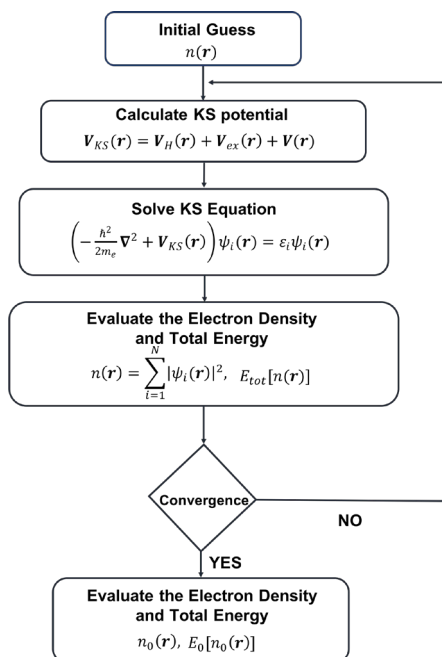


Figure 2.1 Self-consistent field (SCF) scheme to solve the KS equation.

In the early stage of chemical theory development, each atomic orbital was represented by Slater-type orbitals (STOs). STOs are written as the product of spherical harmonics, $Y_{l,m}(\theta, \varphi)$ and a radial function

$$\chi(r, \theta, \varphi) = NY_{l,m}(r, \theta, \varphi)r^{n-1}e^{-\zeta r} \quad (2.50)$$

where n is the index for different orbitals, (r, θ, φ) are the spherical coordinates, and (l, m) are the indices for the orbital angular momentum. As there are several orbitals with the same angular dependence but different radial dependence, these are conventionally called multiple- ζ basis.

Even though STOs possess attractive features due to their efficiency in resembling hydrogenic AOs, there is no analytical solution available for their associated integrals. In order to tackle this problem, alternative (*i.e.*, analytically tractable) basis functions are constructed from STOs by changing the radial part from e^{-r} into e^{-r^2} . These functions are known as Gaussian-type orbitals (GTOs), and are written as

$$\chi(r, \theta, \varphi) = N Y_{l,m}(r, \theta, \varphi) r^{n-1} e^{-\zeta r^2} \quad (2.51)$$

Currently, in modern computational methods, advanced basis functions are constructed in such a way that they satisfy four main requirements: i) To treat core and valence electrons differently, ii) To account for correlation effects with basis functions with correlation consistent behaviors, iii) To accurately account for molecular geometry predictions through polarized functions, and iv) To handle excited electronic states and ionic systems with functions exhibiting diffusive behavior.

2.4.2 Basis Set Superposition Error

In LCAO-based codes, basis function representing chemical species under investigation overlap. This implies that each atom is fictitiously augmented by the basis set functions of its neighboring atoms. This translates into an artificial strengthening of the intermolecular interaction known as basis set superposition error (BSSE). The BSSE manifests, in particular, in the calculation of (non-covalent) binding energies, where the energies of the fragments are overestimated as a consequence of the overlapping of the basis set of the constitutive molecular species. The BSSE can be corrected via the counterpoise (CP) method.⁹⁰ The CP correction allows for compensating the mentioned additional contribution arising from the basis set of neighboring atoms, with the introduction of a *ghost fragment* described by the BS of the constituent atoms that does not carry over any electron. The binding energy of two chemical entities A and B (ΔE) is given by

$$\Delta E = E_{AB} + E^{cp} \quad (2.52)$$

where ΔE is the counterpoise corrected energy, E_{AB} is the total energy of system AB, and the counterpoise correction is obtained through

$$E^{cp} = (E_A - E_{AB'}) + (E_B - E_{A'B}) \quad (2.53)$$

E_{AB} is the energy of fragment A in the basis sets of the combined fragments AB and $E_{A'B}$ is the energy of fragment B in the basis sets of the combined fragments AB, where the AOs are replaced by the so-called *ghost orbitals* at the atomic positions in fragment B.

2.4.3 Plane-wave (PW) Method

In plane-wave (PW) DFT based methods, widely used in solid-state physics, the wave function is expressed as the sum of plane waves

$$\psi_{kv}(\mathbf{r}) = \frac{1}{(\Omega)^{1/2}} \sum_{\mathbf{G}} c_v(\mathbf{k} + \mathbf{G}) e^{i(\mathbf{k} + \mathbf{G}) \cdot \mathbf{r}} \quad (2.54)$$

where Ω is the volume of the unit cell, \mathbf{G} is the reciprocal lattice vector, v indicates the band index, and \mathbf{k} is a continuous wave vector that is confined to the first Brillouin zone (FBZ) of the reciprocal lattice. The coefficients $c_v(\mathbf{k} + \mathbf{G})$ are normalized to satisfy the normalization condition such that

$$\sum_{\mathbf{G}} |c_v(\mathbf{k} + \mathbf{G})|^2 = 1 \quad (2.55)$$

The use of a PW-based basis set allows for the implementation of efficient algorithms based on the concept of Fast Fourier Transform (FFT) that provide a straightforward way to move back and forth from the direct to the reciprocal space, making the computational exploration of material properties quite practical.

The KS equation (Equation 2.34) can now be written in terms of reciprocal space vectors as

$$\sum_{\mathbf{G}} \left[\frac{\hbar^2}{2m_e} |\mathbf{k} + \mathbf{G}|^2 + v_H(\mathbf{G} - \mathbf{G}') + v_{ex}(\mathbf{G} + \mathbf{G}') + v_{ext}(\mathbf{G}, \mathbf{G}') \right] c_v(\mathbf{k} + \mathbf{G}) = \varepsilon_{kv} c_v(\mathbf{k} + \mathbf{G}) \quad (2.56)$$

Such an expression indicates that the Hamiltonian will assume a block diagonal form with respect to the \mathbf{k} -vectors and diagonalization can thus be done within each of these blocks separately.

For the study of ground-state properties of a system, for each \mathbf{k} -point, only a finite number of the lowest-energy electronic states on which all the electrons of the system can be accommodated are needed to be computed to obtain the charge density. This quantity is then used to construct a new guess of the potential to be reintroduced in the KS equations for the successive step of the iterative diagonalization.

While plane-wave expansion is exact in the limit of infinite number of \mathbf{G} -vectors, in practical calculations, a finite number of plane waves are included; these correspond to those plane-waves contained in a sphere of maximum kinetic energy. This artificial theoretical threshold is called *energy cut-off* (E_{cut}) and it is formally written as

$$\frac{\hbar^2}{2m_e} |\mathbf{k} + \mathbf{G}|^2 \leq E_{cut} \quad (2.57)$$

Given this approximation, the accuracy obtained in solving the KS equation under the condition is dictated by Equation 2.57. This means that, once E_{cut} is fixed, all the wave functions of the system whose variation takes place over distances larger than or equal to $2\pi\hbar/\sqrt{2m_e E_{cut}}$ are well described.⁹¹ The integration in the expression for the electron density in the FBZ is

$$n(\mathbf{r}) = \frac{\Omega}{(2\pi)^3} \sum_{i=1}^{N_e} \int f_i |\psi_i(\mathbf{k}, \mathbf{r})|^2 d\mathbf{k} \quad (2.58)$$

where f_i is the occupation number of the i -th state, N_e number of electronic states, and Ω is the cell volume, which is approximated by the discrete sum over a set of the q^3 special \mathbf{k} -point grids, generated within the FBZ (Equation 2.55). In actual electronic structure calculations, a fine mesh is generated, and the sum is converted to an integral over the FBZ of the \mathbf{k} -points and summing over the band index ν . For the purposes of the dissertation projects, the mesh points were generated by using the Monkhorst and Pack method.⁹¹ According to this method, for a given integer numbers r a sequence of m_r real number are generated by the relation

$$m_r = \frac{2r-q-1}{2q}, \quad r = 1, 2, 3, \dots, q \quad (2.59)$$

where q is an integer that determines the number of special k -points in the set. These discretized points are related to the symmetry of the Bravais-lattice and this theoretical framework allows for writing the electron density as

$$n(\mathbf{r}) = \sum_{i=1}^{N_e} \sum_{j=i}^{q^3} f_i w_j |\psi_i(\mathbf{k}_j, \mathbf{r})|^2 d\mathbf{k} \quad (2.60)$$

2.4.4 Pseudo-potentials

The use of pseudopotentials (PP)⁹² is based on the assumption that the most relevant physicochemical properties of a system are carried by valence electrons, while the core electrons can be considered as *frozen* in their electronic configurations. The valence electrons thus move in the effective external field produced by these inert core electrons. Pseudopotentials allow for accurate calculation of the core electron potential on the valence electrons without explicitly including the core electron states in the calculations. Pseudopotentials are constructed to mimic the valence orbitals with respect to a radius cutoff, numerically tuned (see Figure 2.2). The two most common forms of pseudopotential used in modern plane-wave electronic structure codes are norm-conserving and ultrasoft pseudopotentials.⁹³⁻⁹⁴

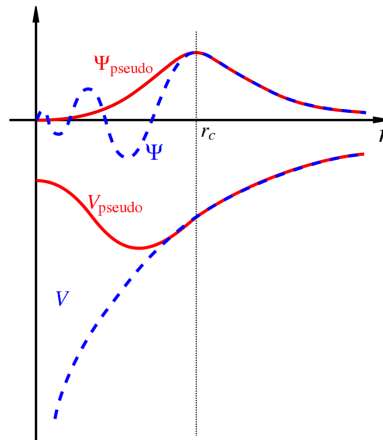


Figure 2.2 Comparison of the wave function and the Coulomb potential of the nucleus (blue) to the corresponding pseudo-potential (red). The real and the pseudo wave function and potentials match above a certain cutoff radius.

2.5 Periodic Systems

In solid state physics or chemistry, DFT studies of periodic systems are performed by placing atoms at their equilibrium lattice points which are infinitely and periodically repeated. The electrons in the materials then dwell under the effect of the external potential given by

$$V(\mathbf{r} + \mathbf{R}) = V(\mathbf{r}) \quad (2.61)$$

where \mathbf{R} translates through the direct lattice of the system under consideration and is given by

$$\mathbf{R} = \sum_{i=1,3} n_i \mathbf{a}_i \quad (2.62)$$

where n is an integer and \mathbf{a} is the direct lattice vector which determines the periodicity of the lattice in the three independent spatial coordinates. The electronic Hamiltonian and the physical quantities used to describe the system also exhibit the translational invariance of the lattice. Under these theoretical promises, the Bloch theorem applies which allows for writing the single particle electronic wave function as

$$\psi_{\mathbf{k}v} = e^{i\mathbf{k} \cdot \mathbf{r}} u_{\mathbf{k}v}(\mathbf{r}) \quad (2.63)$$

where \mathbf{k} is the crystal momentum of the electrons, v runs on the states associated to the same \mathbf{k} -vector and $u_{\mathbf{k}v}$ is a function with the same periodicity of the solid-state system under investigation

$$u_{\mathbf{k}v}(\mathbf{r} + \mathbf{R}) = u_{\mathbf{k}v}(\mathbf{r}) \quad (2.64)$$

The \mathbf{k} -vectors are defined within the First Brillouin Zone (FBZ) of the reciprocal space as

$$\mathbf{k} = \sum_{i=1,3} m_i \mathbf{b}_i \quad (2.65)$$

where \mathbf{b} is reciprocal lattice vector related to the direct lattice vector \mathbf{a} through the scalar product

$$\mathbf{b}_i \cdot \mathbf{a}_j = 2\pi\delta_{ij}, \quad i, j = 1, 2, 3 \quad (2.66)$$

Considering a lattice defined by the primitive translation vectors \mathbf{a}_1 , \mathbf{a}_2 , and \mathbf{a}_3 , the associated primitive reciprocal-lattice vectors are given by the following vector products.

$$\mathbf{b}_1 = \frac{2\pi}{\Omega} \mathbf{a}_2 \times \mathbf{a}_3, \quad \mathbf{b}_2 = \frac{2\pi}{\Omega} \mathbf{a}_3 \times \mathbf{a}_1, \quad \mathbf{b}_3 = \frac{2\pi}{\Omega} \mathbf{a}_1 \times \mathbf{a}_2 \quad (2.67)$$

where Ω is the volume of the unit cell, and \mathbf{b}_1 , \mathbf{b}_2 , and \mathbf{b}_3 span the reciprocal lattice within the FBZ volume $8\pi^3/v$. With the generated m_r numbers (Equation 2.59), the vector

$$\mathbf{k}_{prs} = m_p \mathbf{b}_1 + m_r \mathbf{b}_2 + m_s \mathbf{b}_3 \quad (2.68)$$

can be now be defined which gives q^3 distinct k-points grids uniformly spaced in the FBZ.

2.6 Dispersion Correction

Dispersion energy arises from instantaneous charge fluctuations (*i.e.*, correlated motion of electrons) such as induced dipoles. DFT generally fails to correctly describe the long-range dispersion interaction between molecules or atoms of interacting systems. In fact, the asymptotic behavior (r^{-6}) of long-range interactions is not intrinsically incorporated in the DFT formulation; this aspect limits the applicability of DFT to systems where dispersion interactions are significant. In order to overcome such limitation, in this work, *a posteriori* correction scheme by Grimme dispersion correction⁹⁵ and the vdW-DF (*exchange-correlation* functional correction scheme)⁹⁶ have been employed. As such, they are discussed in more details in the next two sections.

2.6.1 The Grimme Dispersion Correction

According to Grimme's dispersion approach (DFT-D), the DFT total energy obtained by an *exchange correlation* functional can be augmented with a quite simple and straightforward dispersion correction of the form

$$E_{DFT+D} = E_{DFT} + E^D \quad (2.69)$$

where the two-body component of the empirical dispersion energy is given by

$$E^D = - \sum_{i < j} \sum_{n=6,8,10,\dots} s_n \frac{C_{n,ij}}{r_{ij}^n} f_{damp,n}(r_{ij}) \quad (2.70)$$

In Equation 2.70 the first sum runs over all unique pairs of i and j atoms, $C_{n,ij}$ are isotropic n^{th} -order dispersion coefficients for the atom pair ij , r_{ij} is the inter-atomic distances between atom i and atom j , s_n are global, density functional dependent scaling parameters, and $f_{damp}(r_{ij})$ is a damping function. In the construction of DFT-D (and its derived approach such as DFT-D2), the iteration of dispersion models is truncated at $n=6$, with chemically insensitive dispersion coefficients, $C_{6,ij}$, and the sum of atomic van der Waals radii, $r_{0,ij}$. The damping function is represented by the Fermi function and takes the form

$$f_{damp,6}^{D2} = \left[1 + \exp\left[-\alpha \left(\frac{r_{ij}}{r_{0,ij}} - 1 \right) \right] \right]^{-1} \quad (2.71)$$

where α is generally fixed at a given value. One of the most important advantages of DFT-D (and D2) implementation is that it is computationally inexpensive as per Equation 2.71, as no update is needed to the wave functions during computational iterations. In fact, the addition of dispersion contribution, affects only the geometry relaxation of the system as the atomic forces are computed from the total energy.

The latest Grimme dispersion correction is known as DFT-D3, and is constructed in such a way that $C_{n,ij}$ coefficients set to be weakly dependent upon the chemical environment and the sum in Equation 2.72 extends to include the $n=8$ term.⁹⁷

2.6.2 The vdW-DF Dispersion Correction

In the vdW-DF approach⁹⁶, the dispersion correction contribution is built by including a new term in the expression for the *exchange correlation* functional. The former contribution arises from the exchange energy determined by the revised PBE⁹⁸ functional; the latter contribution arises from the correlation energy term determined at LDA level and from the non-local correlation that contributes due to the long-range van der Waals dispersion

$$E_{xc}^{vdw-DF} = E_x^{revPBE} + E_c^{LDA} + E_c^{nl} \quad (2.72)$$

where

$$E_c^{nl}[n(\mathbf{r})] = \frac{1}{2} \int n(\mathbf{r}) \phi(\mathbf{r}, \mathbf{r}') n(\mathbf{r}') d\mathbf{r} d\mathbf{r}' \quad (2.73)$$

Its more recent version is the vdW-DF2 method⁹⁹ where the more repulsive exchange functional revPBE is replaced by the PW86¹⁰⁰ exchange, resulting in an overall general improvement in equilibrium spacing between non-covalently bound complexes, as well as binding energies, especially in systems where hydrogen bonds play a significant role.

2.7 Normal Vibrational Modes in Molecules and Crystals

Vibrational normal modes of molecules and periodic system are, to a first approximation, calculated within the harmonic approximation^{72, 101-102} where the PES is approximated by a parabolic function. Here, the treatment of molecular cases is described first, followed by the treatment of periodic structures.

The Born–Oppenheimer potential energy surface of a system with N nuclei, $V(\mathbf{x})$, is a function of vector \mathbf{x} of the $3N$ coordinates of the atoms in a system. In the harmonic approximation, such potential takes the form

$$V(0) = \frac{1}{2} \sum_{\alpha\beta} u_{\alpha} H_{\alpha\beta} u_{\beta} \quad (2.74)$$

where u_{α} represents the displacement of the α -th Cartesian coordinate from equilibrium and 0 refers to equilibrium. The Hessian matrix $H_{\alpha\beta}$ (*i.e.*, the second derivatives of $V(\mathbf{x})$ with respect to the displacements) evaluated at equilibrium is given by

$$H_{\alpha\beta} = \frac{1}{2} \left[\frac{\partial^2 V(\mathbf{x})}{\partial u_{\alpha} \partial u_{\beta}} \right]_0 \quad (2.75)$$

When weighted displacement coordinates $q_{\alpha} = \sqrt{m_{\alpha}} u_{\alpha}$ are introduced, with m_{α} indicating the mass of the atom associated with α -th coordinate, the classical vibrational Hamiltonian for a polyatomic molecule becomes

$$\begin{aligned} H = T + V &= V_0 + \frac{1}{2} \left(\sum_{\alpha} m_{\alpha} \dot{u}_{\alpha}^2 + \sum_{\alpha\beta} u_{\alpha} H_{\alpha\beta} u_{\beta} \right) \\ &= V_0 + \frac{1}{2} (\langle p|p \rangle + \langle q|W|q \rangle) \end{aligned} \quad (2.76)$$

where $p_{\alpha} = \dot{q}_{\alpha}$, V_0 is the electron potential, and

$$W_{\alpha\beta} = \frac{H_{\alpha\beta}}{\sqrt{m_{\alpha} m_{\beta}}} \quad (2.78)$$

is the weighted Hessian. The eigenvalues k_{α} of the Hermitian matrix $W_{\alpha\beta}$ are the generalized force constants. Equation 2.78 can then be factorized into $3N$ one-dimensional

equation where each of the $3N-6$ vibrational modes can be seen as a collective oscillatory motion characterized by frequency

$$\omega_v = \frac{\sqrt{k_\alpha}}{2\pi} \quad (2.79)$$

This corresponds to using the basis of the generalized coordinates $q_\alpha(\mathbf{k})$ instead of the q_α coordinates defined previously for molecules. The generalized coordinates take the form

$$q_\alpha(\mathbf{k}) = N \sum_{\mathbf{G}} q_\alpha^{\mathbf{G}} e^{-i\mathbf{k} \cdot \mathbf{G}} \quad (2.80)$$

This allows to block-factorize the vibrational problem into a set of problems (one for each \mathbf{k} -point in the Brillouin zone) of dimension $3N$, where N is the number of atoms in the unit cell. The \mathbf{k} -th block of the \mathbf{k} -factorized W matrix takes the form

$$W_{\alpha\beta} = \sum_{\mathbf{G}} \frac{H_{\alpha\beta}^{0\mathbf{G}}}{\sqrt{m_\alpha m_\beta}} e^{-i\mathbf{k} \cdot \mathbf{G}} \quad (2.81)$$

where $H_{\alpha\beta}^{0\mathbf{G}}$ is the second derivative of $V(\mathbf{x})$ with respect to atom α in cell $\mathbf{0}$ (where translation invariance is exploited) and atom β in cell \mathbf{G} and as determined at equilibrium. When only the high symmetry point $\Gamma(0, 0, 0)$ is considered, the above equation reduces to

$$W_{\alpha\beta}(0) = \sum_{\mathbf{G}} \frac{H_{\alpha\beta}^{0\mathbf{G}}}{\sqrt{m_\alpha m_\beta}} \quad (2.82)$$

Frequencies at the Γ point are evaluated exactly in the same way as described for molecules: a set of $3N+1$ SCF calculations of the unit cell are performed at the equilibrium geometry.

The corresponding IR intensities are computed from the change in dipole-moments that allow to write the intensity of the p -th IR mode as

$$I_p \propto d_p \left| \frac{\partial \vec{\mu}}{\partial Q_p} \right|^2 \quad (2.83)$$

This equation indicates that each IR mode is proportional to the square of the modulus of the first derivative of the dipole moment, $\vec{\mu}$, with respect to displacement, \vec{Q}_p , along the normal mode direction Q_p , times the d_p degeneracy of the mode.

2.8 Climbing Image Nudged Elastic Band Method

The nudged elastic band (NEB)¹⁰³ is a chain-of-state¹⁰⁴ method in which a string of intermediate images is used to represent the minimum energy path (MEP) between two known minima (usually the initial and the final states). The images are connected by spring forces to ensure a quasi-equal spacing along the pathway. The intermediate images connecting the initial and final state along the NEB path are relaxed to MEP through a force projection scheme determined by the potential energy surface (PES). Given the parameter s , and considering the reaction path $\mathbf{X}(s)=(x_1(s), x_2(s), \dots, x_n(s))^T$, the unit tangent is given as $\mathbf{U}=(d\mathbf{X}/ds)/|d\mathbf{X}/ds|$. The force on an intermediate image g_i has two independent components:

$$\mathbf{F}_i^{NEB} = \mathbf{F}_i^\perp + \mathbf{F}_i^s \quad (2.84)$$

where \mathbf{F}_i^\perp is the component of the force perpendicular to the unit tangent:

$$\mathbf{F}_i^\perp = -P_t \nabla V(g_i), \quad P_t = \mathbf{U} - \mathbf{U}_i \mathbf{U}_i^T \quad (2.85)$$

$\nabla V(g_i)$ is the gradient of the PES, and \mathbf{F}_i^s is the spring force parallel to the direction of the MEP.

$$\mathbf{F}_i^s = k(|g_{i+1} - g_i| - |g_i - g_{i-1}|)\mathbf{U}_i \quad (2.86)$$

where k is the spring constant. Using an optimization algorithm, the MEP between the two images can be reached by updating the path in such a way that the perpendicular forces on each intermediate image numerically vanish.

Even though the NEB method is generally computationally inexpensive, it has the drawback to not necessarily provide an accurate transition state (TS). This flaw is resolved by the climbing image NEB (CI-NEB),¹⁰⁵⁻¹⁰⁶ a modified NEB method where spring forces are removed from the image with the highest energy after a nearly converged NEB calculation. The removal of the spring forces provides support to the image climb towards the TS.

3 Results: Binding Energies of Hydrocarbons Addressed via MOF-74-Mg/Zn Molecular Cluster Models

3.1 Introduction

In computational chemistry, a cluster is an assembly of aggregated atoms or molecules that is intermediate in size between a molecule and a bulk solid. Molecular cluster models are often used to approximately represent the periodic bulk systems in modeling studies. The main purposes of using molecular cluster models are to simplify the complex nature of the material to be modeled and to reduce the computational cost that it would otherwise take while using a rather complex bulk periodic structure model, which is usually at the cost of losing chemical accuracy. The importance of conducting accurate computational investigations on new materials is driven by the potential of designing new and smarter materials. Addressing the chemistry of the host-guest complex can suggest structural functionalization able to enhance (or quench) specific adsorption requirements. In this chapter, the investigation of the structural and binding nature of adsorbate molecules with open-metal sites and the difference/similarity in performance between MOF-74-Mg and MOF-74-Zn are explored. This work aims at addressing the selective separation capabilities of these materials with respect to small hydrocarbon molecules. MOF-74-M (M=Mg, Zn) isostructural species are characterized by a high density of coordinatively unsaturated open-metal sites. These materials are also known as CPO-27. MOF-74-M frameworks have demonstrated more separation potential than other known MOFs and zeolites.^{55, 107}

*The material contained in this chapter was previously published in Chemical Physics Letter Elsevier 2016, 660, 313–319 by Gemechis Degaga and Loredana Valenzano. See Appendix F for the reprint permission.

Structurally, MOF-74-M consist of a 3D hexagonal packing of a helicoidal MO₅ chain along the channel (*i.e.*, a not fully coordinated metal atom (M)) connected by 2,5-dihydroxyterephthalate organic (DOT) linkers (Figure 3.1). The unsaturated open metal cations, indicated as dark blue region in the electrostatic potential map (EPM) in Figure 3.1c, play a crucial role in the relative adsorption capability of MOF-74-M, serving as a primary site of adsorption for guest molecules.

In this chapter, first, results from the calculations on molecular cluster models of MOF-74-Mg/Zn for the investigation of the interaction between C₂-C₄ hydrocarbons (C₂H₄, C₂H₆, C₃H₆, C₃H₈, C₄H₈, and C₄H₁₀) and the open-metal site(s) are discussed. Next, the extent to which the use of molecular cluster models adopted to approximate the periodic structure of crystalline MOF materials are reliable for the investigation of the sorption of molecules containing more than four atoms is addressed. Finally, an appreciation of the difference in the selective sorption of MOF-74-Mg and MOF-74-Zn for the separation of C₂-C₄ mixtures is reported as assessed with respect to a molecular cluster approach.

3.2 Theoretical Models and Computational Details

DFT linear combination of atomic orbital calculations were performed with the CRYSTAL14 code.^{65, 101} The hybrid-GGA B3LYP⁸⁵ functional *a posteriori* corrected with a semi-empirical contribution accounting for the long-range $1/r^6$ dispersion term (B3LYP+D2*) was considered.^{95, 108} The adopted values for the modified atomic parameters are presented in Table 3.1. In addition, meta-hybrid GGA M06⁸⁸ was also employed; this functional has shown its efficiency in providing a good semi-empirical description of dispersion forces and in successfully describing organometallic materials. Following previous works by Valenzano *et al.*⁵⁷ a TZV basis set was chosen for Zn while a TZVP basis set was used for Mg. For H, C, and O, the standard Ahlrichs TZP basis sets were adopted.¹⁰⁹ An XLGRID DFT pruned-grid was used for the numerical integrations throughout all the calculations.⁶⁵

Prior to *cutting* the cluster out of its corresponding 3D bulk structure, periodic boundary condition (PBC) dynamic geometry optimizations were performed where the MOF-74-Mg experimental geometry was adopted as an initial starting point for both systems.¹¹⁰

Table 3.1 Long range dispersion parameters for the atoms constituting the molecular cluster models adopted from Valenzano et al.¹⁰⁸

Element	C_6 ($\text{J} \cdot \text{nm}^6 \cdot \text{mol}^{-6}$)	R_{vdW} (\AA)
Hydrogen	0.14	1.3000
Carbon	1.75	1.5246
Oxygen	0.70	1.4091
Magnesium	5.71	1.4322
Zinc	10.80	1.6401

Geometry relaxation was followed by vibrational frequency calculations at the Γ point to check the stability of the MOF structures.¹⁰¹ SCF convergence thresholds were set to 10^{-8} and 10^{-10} Hartrees for geometry optimization and vibrational frequency calculations, respectively. The Monkhorst-Pack⁹¹ shrinking factors for the sampling of the reciprocal space were set to a value of 2, corresponding to 4 k -points in the reciprocal space.

MOF molecular clusters (*i.e.*, finite-size models) were then extracted from the corresponding 3D fully optimized MOF-74-Mg/Zn bulk structures. Hydrogen atoms were added to ensure valence saturation of unsaturated bonds. Two different cluster sizes were built: 3MB and 6MB (MB=metal-benzene), corresponding to a single and double length of the conventional unit cell with respect to the c -direction, respectively. The 3MB notation refers to the smallest (47-atom) cluster size containing three adjacent metal sites and three benzene rings. In this model, only the central metal atom is five-fold coordinated resembling the MO_5 adsorption site as in the original framework. Since only one of the three metals is represented by a structurally complete MOF-74 sorption site, this model can host only one guest molecule.

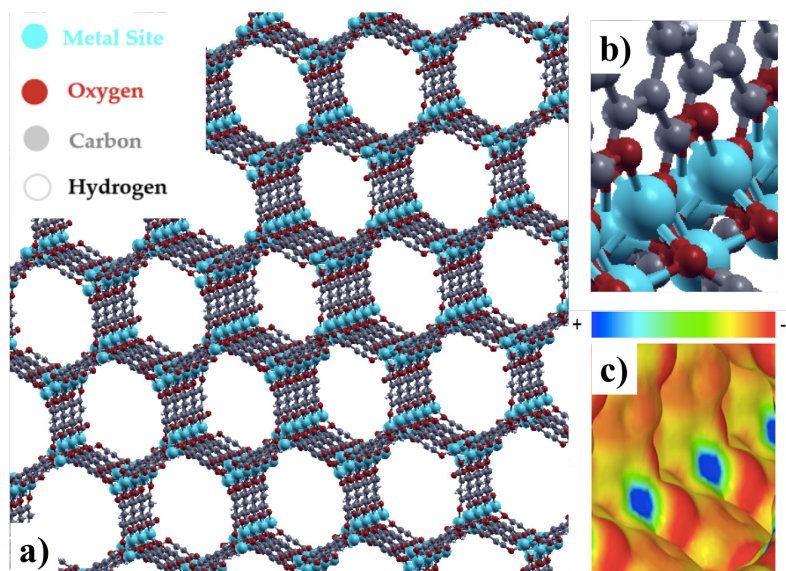


Figure 3.1 A depiction of the 3D structure of bulk MOF-74-M a) showing MOF cavity along the channel, b) emphasizes metal-oxide chain along the channel, and c) electrostatic potential map (EPM) along the metal-oxide chain showing charge deficit open metal centers.

A more chemically realistic situation is depicted by the larger 6MB cluster, a 92-atom model formed by six adjacent metal atoms and six benzene rings. In this case, four out of the six metal atoms are five-fold coordinated, leaving only the two peripheral ones uncompleted. Thus, the 6MB cluster allows for the investigation of the binding process of four guest molecules. Figure 3.2 shows the two cluster structures where, in both cases, the metal atoms resembling the MOF chemical environment are indicated with yellow spheres. Figure 3.3 shows the two clusters as loaded with ethane molecules.

The energetic interaction between the adsorbed molecules and the MOF framework was obtained by applying Hess's law to the electronic energy of the species involved in the adsorption process

$$\Delta E = (E_{C+n \cdot Mol} - (E_C + nE_{n \cdot Mol}))/n \quad (3.1)$$

where $C = 3MB$, and $n = 1$, or $C = 6MB$, and $n = 4$.

3.3 PBC: Relaxed Bulk Structures

With the imposition of PBC, both of the MOF-74-M structures were relaxed at the mentioned levels of theory. Results obtained for lattice parameters are in very good agreement with experimental¹¹⁰⁻¹¹¹ (x-ray diffraction and neutron power diffraction) and other computational (PBE+U)⁵⁸ works as presented in Table 3.2. The c/a ratio is consistent across methods with differences less than 0.3% for MOF-74-Mg. Deviations are more pronounced in the Zn species with B3LYP+D2*, overestimating the c/a ratio by 1.9%, and the average metal-oxygen bond length $\langle \text{M-O} \rangle$ by 0.8%. Since the structure of MOF-74 is mainly determined by the metal cluster center (MO_5) at the six corners of the framework's unit cells, shorter $\langle \text{M-O} \rangle$ lengths can be expected to induce a decrease in the cell volume.

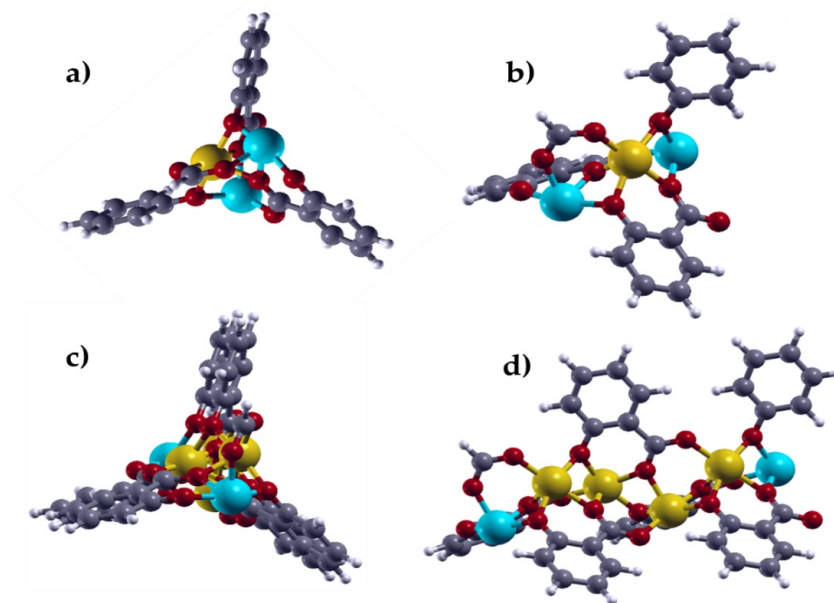


Figure 3.2 3MB and 6MB cluster models where 3MB viewed a) along the c -axis and b) perpendicular to the c -axis while 6MB is viewed c) along the c -axis and d) perpendicular to the c -axis. The yellow spheres represent the binding open metal sites.

This is consistent with the volumes reported in Table 3.2. It is worth mentioning that the choice to adopt M06 was first dictated by the presence of Mg in the framework. Given the negligible difference in volume and therefore in c/a ratio between M06-L and M06 when Zn is present, the latter functional was also adopted for MOF-74-Zn.

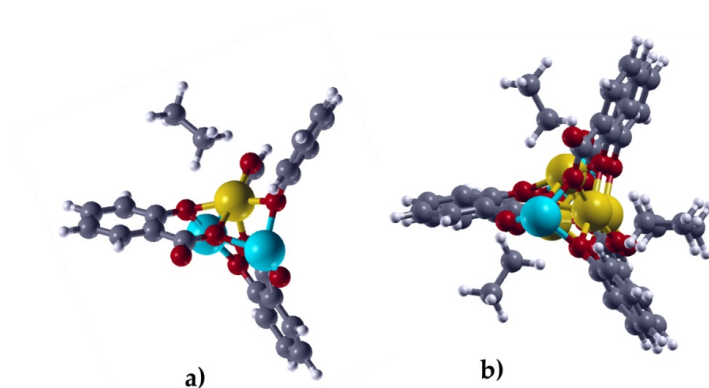


Figure 3.3 a) 3MB cluster loaded with one ethane molecule; b) 6MB cluster loaded with four ethane molecules. Both structures are viewed along the c-axis.

Spin-polarized calculations can also provide evidence of the strength of interaction these molecules have with MOF-74-M species containing transition metals. Recent computational studies showed that, unlike saturated hydrocarbons, for unsaturated light hydrocarbons a ferromagnetic-antiferromagnetic transition is observed upon their adsorption.⁶³⁻⁶⁴ This observation clearly indicates the stronger interaction of these molecules with the metal sites in the frameworks. Furthermore, structural distortion followed by electronic transition (*i.e.*, Jahn-Teller effect) upon the adsorption of guest molecules can provide information about the binding process.¹¹²

From an applied stand point, one cannot solely rely on the change in the energy of adsorption in order to identify the MOFs that are best able to efficiently deal with molecular selection. In fact, BET surface area and pore aperture/volume also need to be considered when adsorptive separation applications are concerned.

In this regard, MOF-74-Mg has by far a higher BET surface area (1332 m²/g) and pore aperture/volume (0.61 cm³/g) than MOF-74-Zn (885 m²/g, and 0.41 cm³/g).⁵² Adding to this aspect its higher selective sorption capability, MOF-74-Mg seems to show the same potential, if not greater than other MOF-74-M species.

Table 3.2 A comparison of calculated lattice parameters, average oxygen-metal bond length, and volume of bulk MOF-74-M (M=Mg, Zn) with results from experimental and theoretical literature. Distances are reported in Angstrom (Å), volumes in Å³.

Metal	Lattice constants (Å)		c/a	<M-O _i >	Volume	c/a
	a	c				
Mg	26.028	6.921	0.266	2.042	4060.51	B3LYP+D2* ¹
	25.967	6.901	0.265	2.041	4030.13	M06 ^a
	25.922	6.888	0.266	2.030	4008.60	M06-L ^a
	26.050	6.910	0.266	2.030		PBE+U ⁵⁸
	26.020	6.720	0.258			XRD ¹¹¹
	25.920	6.860	0.265	2.115		NPD ¹¹⁰
Zn	26.093	6.892	0.264	2.064	4063.44	B3LYP+D2* ^a
	25.979	6.811	0.262	2.047	3980.92	M06 ^a
	26.076	6.762	0.259	2.056	3982.17	M06-L ^a
	26.200	6.920	0.264	2.055		PBE+U ²⁶
	25.890	6.820	0.263			XRD ⁴⁶
	25.720	6.740	0.262	2.110		NPD ¹¹⁰

3.4 Molecular Cluster Models: Geometrical Orientation of Adsorbed C₂-C₄ Molecules

For the molecular cluster model investigations, atoms belonging to the clusters were *kept frozen* during the geometry relaxation process while the intra-atomic distances of the molecules and the molecular relative distances from the adsorption sites were allowed to relax. Geometries across the cluster models, functionals, and MOF species are compared in terms of distances between the metal atom and the two nearest carbons (M-C1 and M-C2) for olefins and the two nearest hydrogens (M-H1 and M-H2) for paraffins.

¹ this work, XRD = X-ray diffraction, NPD= Neutron Powder Diffraction

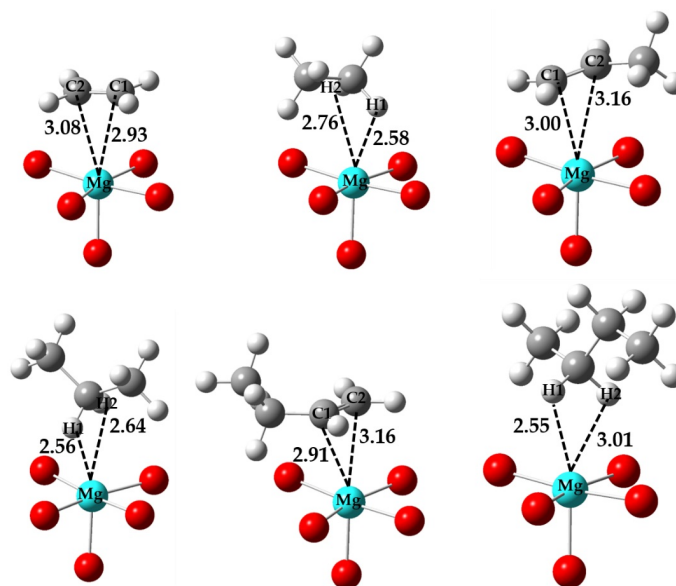


Figure 3.4 Molecular Cluster: Molecular orientation of C_2H_4 , C_2H_6 , C_3H_6 , (upper panel) C_3H_8 , C_4H_8 , and C_4H_{10} (lower panel) molecules at the open metal center of the 3MB molecular cluster of MOF-74-Mg (B3LYP+D2*). Magnesium, oxygen, carbon, and hydrogen atoms are represented by aqua, purple, red, gray, and white spheres, respectively. Distances are reported in Angstroms. Given the similarities of arrangement across the cluster models, the complete list of atomic distances is reported in the Table 3.3-3.4.

Figure 3.4 shows the orientation of adsorbed C_2 - C_4 molecules resulting from the MOF-74-Mg 3MB cluster model. Table 3.3-3.4 present the geometry orientations for olefins and paraffins, respectively, for both clusters, and functionals. The two functionals provide molecular spatial arrangements for ethane and ethylene which lie within 6% with respect to those observed at PBC level (PBC results are presented in Chapter 4), although, in the clusters ethane tends to bend toward the organic *ligand*. Such a difference is not surprising, and it can be related to molecular steric hindrance effects present in the MOF (PBC), but mostly absent in the cluster models where only one molecule is adsorbed. For ethylene (B3LYP+D2*), the distance of the Mg atoms from the two nearest carbons are found to be stretched out in the cluster model by about 3% (3MB), up to 4.5% (6MB) with respect to the PBC results. This change in distance was found to be comparable with that observed at M06 level for both the molecular clusters (up to 5.2%). While at B3LYP+D2* level, the Zn-C distances are elongated up to 7.1% and 7.9% in 3MB, and 6MB, respectively. M06 induces a rather mild stretch (up 2.9% in 3MB, and 4.2% in 6MB) in the cluster models. Results for the molecular orientation are confirmed at M06 level, indicating that the overall long-range interaction is not dramatically influenced by the choice of the functional. The

3MB cluster appears to be sufficient in providing binding energies which for ethane and ethylene are comparable to those obtained at PBC level.

3.5 Molecular Cluster Models: Binding Energies (BE) of Adsorbed C₂-C₄ Molecules

Figure 4a and 4b show the behavior for the binding energies with respect to all the six hydrocarbons and the two levels of theory respectively, for the two molecular cluster models of MOF-74-Mg and MOF-74-Zn. There are important differences between the two differently sized cluster models. The (B3LYP+D2*) trend indicates that the 3MB cluster underestimates the binding energies of the larger molecules by up to 6 kJ/mol, and 10 kJ/mol in MOF-74-Mg and MOF-74-Zn, respectively when compared to their corresponding 6MB cluster. Similarly, at M06 level the 3MB clusters underestimate the binding energies of larger molecules by about 6 kJ/mole, and 12 kJ/mole for MOF-74-Mg and for MOF-74-Zn, respectively.

It is evident that for the larger molecules, the interaction with the framework is not localized to the metal adsorption site only, implying that the long-range dispersion interaction also extends to the nearby carboxylate group of the organic *ligand*. This suggests that the use of a larger molecular cluster is necessary to fully describe the chemical environment, and the mutual interaction of the molecules within the MOF framework.

Table 3.3 Molecular Cluster: Interatomic distances (in Å) between the open metal sites and the two nearest carbon atoms (M-C, M=Mg, Zn) for olefin molecules adsorbed at the open metal sites of the 3MB and 6MB cluster, the average distances $\langle M_i-C \rangle$ for the four open metal sites are reported

Olefin	Metal	Distances	B3LYP+D2*		M06	
			3MB	6MB	3MB	6MB
C_2H_4	Mg	Mg-C1	2.922	2.990	3.094	3.005
		Mg-C2	3.083	3.080	3.017	3.028
	Zn	Zn-C1	2.999	3.020	2.880	2.920
		Zn-C2	3.130	3.155	3.016	3.015
C_3H_6	Mg	Mg-C1	3.004	2.990	2.955	2.945
		Mg-C2	3.157	3.218	3.120	3.250
	Zn	Zn-C1	3.025	3.018	2.896	2.870
		Zn-C2	3.194	3.270	2.931	3.070
C_4H_8	Mg	Mg-C1	2.955	2.953	2.936	2.928
		Mg-C2	3.155	3.140	3.139	3.123
	Zn	Zn-C1	2.568	2.973	2.778	2.673
		Zn-C2	3.364	3.165	3.010	3.295

Figure 3.5 can also be interpreted in terms of overall binding trends with respect to all the hydrocarbons assessed in this work as it stresses the relative binding energy differences between olefins, and paraffins. Both of the functionals agree in indicating differential binding energies ranging from 8 to 18 kJ/mol for Mg metal sites, and from 9 to 17 kJ/mol for Zn. These results show that a mixture of light hydrocarbons flowing through MOF-74-Mg/Zn pores can be selectively separated within either of the frameworks. Even though the cluster models can be expected to underestimate the calculated binding energies, the computed values for saturated and unsaturated hydrocarbons still provide significant

information, as they depict a qualitative trend in the relative difference in binding energy between the hydrocarbons.

Both MOFs show the same degree of olefin/paraffin separation capability differing only by 1-3 kJ/mol in all cases. For example, propylene/propane differential binding energy is found to be about 17 kJ/mol and 16 kJ/mol in MOF-74-Mg and MOF-74-Zn, respectively, at both levels of theory. These results are comparable with those of MOF-74-Fe reported by Thrular *et al.* (18.5 kJ/mol) while they are higher than that reported by Long *et al.* for HKUST-1 (about 13 kJ/mol).⁵³⁵⁴ Overall, the computed binding energies of C₂-C₄ in both MOFs are found to be slightly different for B3LYP+D2* and M06 functionals, ranging from 1 to 7 kJ/mol.

Table 3.4 Molecular Cluster: Interatomic distances (in Å) between the open metal sites and the two nearest hydrogen atoms (M-H, M=Mg, Zn) for paraffin molecules adsorbed at the open metal sites of the 3MB and 6MB molecular clusters computed at B3LYP+D2* adsorbed at the open metal sites of the 3MB and 6MB molecular clusters computed at B3LYP+D2* adsorbed at the open metal sites of the 3MB and 6MB cluster, the average distances <M_i-H> for the four open metal sites are reported.

Paraffin	Metal	Distances	B3LYP+D2*		M06	
			3MB	6MB	3MB	6MB
C ₂ H ₆	Mg	Mg-H1	2.579	2.683	2.510	2.500
		Mg-H2	2.759	2.700	2.547	2.553
	Zn	Zn-H1	2.519	2.685	2.438	2.458
		Zn-H2	2.875	2.828	2.516	2.595
C ₃ H ₈	Mg	Mg-H1	2.555	2.570	2.439	2.388
		Mg-H2	2.641	2.695	2.606	2.870
	Zn	Zn-H1	2.423	2.453	2.110	2.228
		Zn-H2	2.962	2.983	2.946	2.990
C ₄ H ₁₀	Mg	Mg-H1	2.545	2.465	2.399	2.388
		Mg-H2	3.007	2.913	2.964	3.013
	Zn	Zn-H1	2.279	2.295	2.129	2.258
		Zn-H2	3.178	2.850	2.883	3.098

Interestingly, for paraffins, the binding energy is solely governed by long-range dispersion forces, strongly indicating the impossibility of reliably describing such interactions with theories not able to include such weak electronic interactions. Overall, the dispersion contribution increases from the smallest (ethylene) to the largest paraffin (butane) in both cluster models for both MOFs.

Table 3.5 Molecular Cluster: Binding energies for C₂-C₄ adsorbed on the 3MB, and 6MB clusters for both Mg, and Zn. The pristine B3LYP, and the dispersion correction (D2*) contribution are indicated as they sum up to give the binding energies (BE). M06 results are reported for comparison. All energies are reported in kJ/mol.

Metal	Adsorbate	3MB-Cluster				6MB-Cluster			
		B3LYP+D2*			M06	B3LYP+D2*			M06
		B3LYP	D2*	BE		B3LYP	D2*	BE	
Mg	Ethylene	-9.99	-35.15	-45.14	-44.55	-12.48	-37.74	-45.65	-45.38
	Ethane	2.68	-32.13	-29.45	-31.65	2.71	-32.62	-29.91	-33.86
	Propylene	-5.43	-45.48	-50.91	-53.54	-3.06	-52.45	-55.51	-55.96
	Propane	3.16	-35.65	-32.49	-35.30	5.78	-44.47	-38.69	-39.35
	Butylene	-5.62	-47.52	-53.14	-54.14	-4.63	-53.56	-58.18	-57.28
	Butane	9.32	-46.76	-37.44	-43.11	13.04	-57.61	-44.58	-49.01
Zn	Ethylene	-8.92	-33.11	-42.03	-45.77	-6.37	-36.64	-43.01	-45.13
	Ethane	2.21	-29.24	-27.03	-34.00	4.10	-33.34	-29.24	-36.07
	Propylene	-5.74	-45.18	-50.91	-53.54	-2.37	-52.87	-55.24	-56.28
	Propane	3.59	-37.04	-33.45	-36.57	5.93	-45.54	-39.61	-39.35
	Butylene	-6.06	-47.65	-53.71	-56.12	-3.59	-53.88	-57.47	-59.53
	Butane	6.44	-46.20	-39.76	-44.86	11.03	-60.48	-49.45	-57.31

3.6 Summary

DFT calculations were performed to investigate the binding nature of C₂-C₄ hydrocarbons in MOF-74-Mg/Zn. B3LYP+D2* and M06 functionals were used to investigate molecular clusters representing the MOFs' region of chemical interest. Results show that olefins interact more energetically to the open metal sites than their corresponding paraffin counterparts with differential binding energies ranging from 8 to 18 kJ/mol. This indicates that a mixture of light hydrocarbons flowing through the MOF's cavities can be selectively separated. Both MOFs show the same degree of separation capability with respect to the two functionals, regardless of the size of the molecular cluster models.

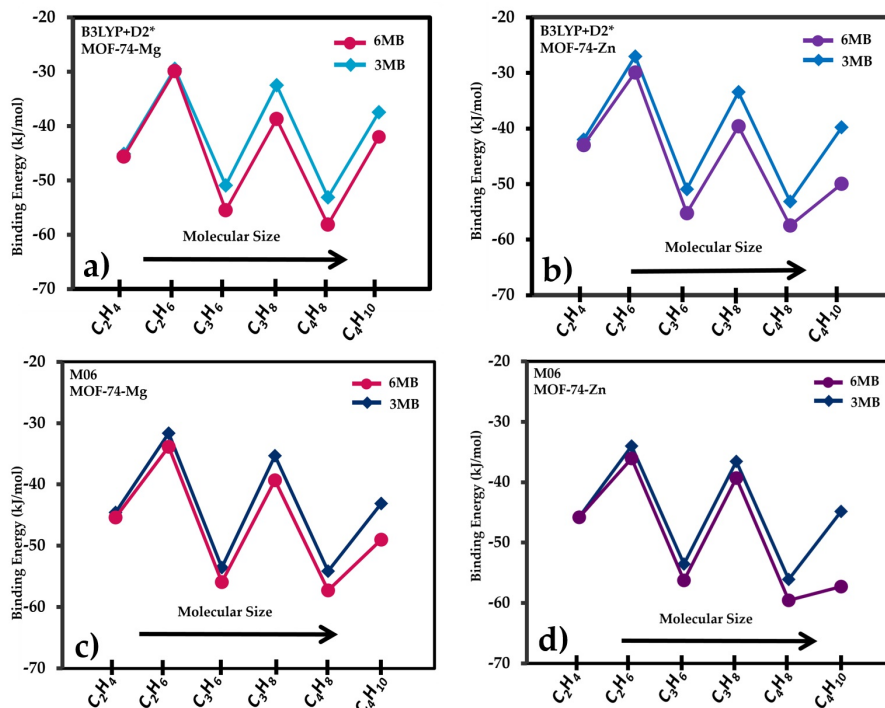


Figure 3.5 Molecular Cluster: Trend for the binding energies with respect to molecular size for 3MB and 6MB MOF-74-Mg molecular clusters: a) B3LYP+D2*, and b) M06; MOF-74-Zn molecular clusters: c) B3LYP+D2*, and d) M06.

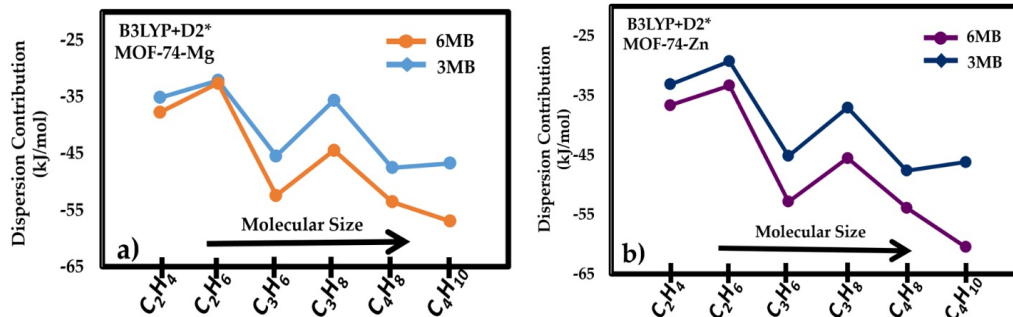


Figure 3.6 Molecular Cluster: Trend for the dispersion contribution (D2*) with respect to molecular size for 3MB and 6MB a) MOF-74-Mg and b) MOF-74-Zn cluster models.

Underestimation of the binding energies for butylene and butane observed at 3MB cluster level, indicates the importance of considering a more chemically meaningful cluster when larger molecules are adsorbed. In addition, for paraffins, dispersion forces are solely responsible for the strength of the interaction.

4 Results: Heats of Adsorptions of Hydrocarbon Molecules Addressed via MOF-74-Mg/Zn Periodic Boundary Condition (PBC) Models

4.1 Introduction

As demonstrated in the previous chapter, the contribution that accurate computational investigations on novel materials can provide is related to their potential to assess details (at the electronic, atomic and molecular scale) and eventually provide guidance in enhancing the properties of already available frameworks but also to support the *ad hoc* design of new and more efficient materials. In this regard, rigorous characterization and understanding of the structural and binding nature of guest molecules with respect to the open metal sites in the MOF structure, and assessment of the different behavior of various metal cations allow for revealing the potential about the performances of the chosen frameworks toward separation applications. In addition, the knowledge about the nature of the chemistry of the host-guest complex can suggest possible structural functionalization able to enhance (or quench) specific adsorption requirements. Despite being simpler and computationally less demanding, the use of molecular cluster models to assess light hydrocarbon separation encounters the risk of not always providing an accurate and realistic description of the interaction of the molecules at the open metal centers.

*The material contained in this chapter was previously published in two Chemical Physics Letter articles, (1) Elsevier 2016, 660, 313–319 (2) Elsevier 2017, 682, 168–174 both by Gemechis Degaga and Loredana Valenzano. See Appendix F and G for the reprint permission.

With the investigation of the molecular cluster models¹¹³, the influence that the chemical environments of the frameworks have on the assessment of molecular binding energies was discussed. This aspect indicated how a minimal cluster model was not able to properly describe the intermolecular interaction of the larger hydrocarbons with open metal sites; the outcome of that assessment was quite dramatic, indicating differences in the binding energies as large as 12 kJ/mol per metal site.

As a further step, in this chapter, density functional theory (DFT) is applied to full 3D periodic structures of MOF-74-Mg and MOF-74-Zn to investigate the role that, together with the chemical environment, basis set superposition error (BSSE)⁹⁰, zero-point energy (ZPE), and thermal energy corrections play to correct the binding energy results to get heats of adsorption which can, eventually, provide insights more directly comparable with experimental evidence. In addition, the role of the molecular lateral interaction is also addressed.

The focus of this chapter is therefore to address, at fundamental level, the effect that the chemical environment of the frameworks, the several physicochemical contributions (i.e., lateral interaction, ZPE, and thermal corrections) and the inevitable corrections arising from the application of theoretical approximations (i.e., from the semi-empirical treatment of dispersion forces to BSSE) have on the structure and on the binding nature of C₂-C₄ molecules adsorbed in MOF-74 treated as 3D periodic structures. The intent of this investigation is to provide an even more accurate, and refined description of the proposed problem as described at computational level in order for the results to be fully comparable with experimental data. In addition, with respect to the mentioned implications that the thematic discussed herein may have at application levels, this work aims at providing a better understanding of the efficiencies that MOF-74-Mg/Zn have for the separation of C₂-C₄ mixtures in petroleum refining processes.

4.2 Computational Methods and Models

Similarly to the approach described in the previous chapter, linear combination of atomic orbital (LCAO, all-electron Gaussian-type basis sets) DFT calculations were performed

with the Crystal14 code^{65, 114}. The hybrid-GGA B3LYP^{63, 85} functional *a posteriori* corrected with a semi-empirical contribution accounted for the long range $1/r^6$ dispersion term employed.⁹⁵ The original Grimme parametrization for the molecular species was modified to include the effect of periodic boundary conditions as implemented in the Crystal program.¹⁰⁸ The motivation for choosing these theoretical approaches lays in their efficiency, and capability of providing reliable quantitative information about the nature of the long-range interactions characterizing the addressed problem. The adopted values for the modified atomic parameters are listed in Table 3.1. Following previous works^{56-57, 113}, TZV and TZVP basis sets were chosen for Zn and Mg atoms, respectively. For H, C, and O, the standard Ahlrichs TZP basis set was adopted¹⁰⁹. Throughout all the calculations, the numerical integration task was achieved by applying an XLGRID pruned-grid.⁶⁵

Full 3D periodic boundary condition (PBC) dynamic geometry relaxations (*i.e.*, simultaneous relaxation of both lattice parameters, and atomic positions) were performed on both the 3D bulk structures of MOF-74-Mg/Zn starting from the experimentally refined geometry of MOF-74-Mg that was adopted as a guess solution for both systems.¹¹⁰ After full geometry relaxation, vibrational frequency calculations were performed to ensure the stability of the solutions, and to account for the zero-point and thermal energy corrections, which allow for correcting the binding energies and provide heats of adsorption. SCF convergence thresholds were set to 10^{-8} and 10^{-10} Hartrees for geometry optimization and vibrational frequency calculations, respectively. The Monkhorst-Pack⁹¹ shrinking factors for the reciprocal space sampling were set to 2 corresponding to four k-points in the reciprocal space.

The energetic interaction between the adsorbed molecule and the open metal sites in the MOFs was obtained by applying the Hess's law, following Equation 3.1. We shall refer to the different molecular loading as low (one molecule), medium (three molecules) and high (six molecules).

Binding energies obtained within a PBC approach were corrected for BSSE via the counterpoise correction method.^{90, 101} From the vibrational frequencies, the zero-point

vibrational energy E_{ZPV} and the thermal contribution (TE) to the standard enthalpy $H^0(T)$ at room temperature T were calculated for molecules in the gas phase as

$$H^0(T) = E_{trans}(T) + E_{rot}(T) + E_{vib}(T) + RT \quad (4.1)$$

where E_{trans} , E_{rot} , and E_{vib} are the translational, rotational, and vibrational contributions respectively, and RT is the correction from the PV term (*i.e.*, ideal gas approximation). For the unloaded (no molecules adsorbed) MOF-74 bulk structure

$$H^0(T) = E_{vib} \quad (4.2)$$

Overall, the enthalpy of adsorption at a given temperature T is calculated as

$$H_T^0 = E + E_{ZPE} + H^0(T) \quad (4.3)$$

and it corresponds to the experimentally observed heat of adsorption:

$$q_{ads}(T) = -H_T^0 \quad (4.4)$$

The zero-point vibrational energy E_{ZPV} and the thermal contribution to the enthalpy $H(T)$, at temperature $T=298.15\text{ K}$ and standard pressure P^0 were calculated for molecules in the gas phase following Equation 4.1 through Equation 4.4.

Three PBC models were put in place in order to investigate the role played by intermolecular lateral interactions on the molecular arrangement and binding energies of small hydrocarbons. A *frozen* MOF framework approach was considered where only the loaded molecules were allowed to relax while the pre-optimized (pristine) MOF frameworks remain geometrically *frozen* throughout the relaxation procedure. The

conventional unit cell of both MOF-74-Mg/Zn in their trigonal space group $\bar{R}3$ comprising 54 atoms is used. As mentioned, for both MOFs the initial geometries were set to that of the experimental refined MOF-74 structure with lattice parameters $a = b = 25.784 \text{ \AA}$, $c = 6.747 \text{ \AA}$, $\alpha = \beta = 90^\circ$ and $\gamma = 120^\circ$ ¹¹⁵. The three different molecular loadings are identified as low, medium and high loadings referring to one, three, and six molecules, respectively, symmetrically arranged at one, three, and six open metal sites in the MOF-74-Mg/Zn unit cells (see Figure 4.1).

In this chapter, full PBC calculation results for ethylene and ethane are first presented as benchmarking investigation by considering high molecular loading. PBC calculations in sections 4.2-4.5 refer to the case where geometry relaxation of both the atoms of the MOFs (hence the structure of frameworks) and spatial orientation of the molecules at the open metal sites are taken into consideration. PBC calculations in section 4.6-4.9 refer to the *frozen* MOF approach mentioned above.

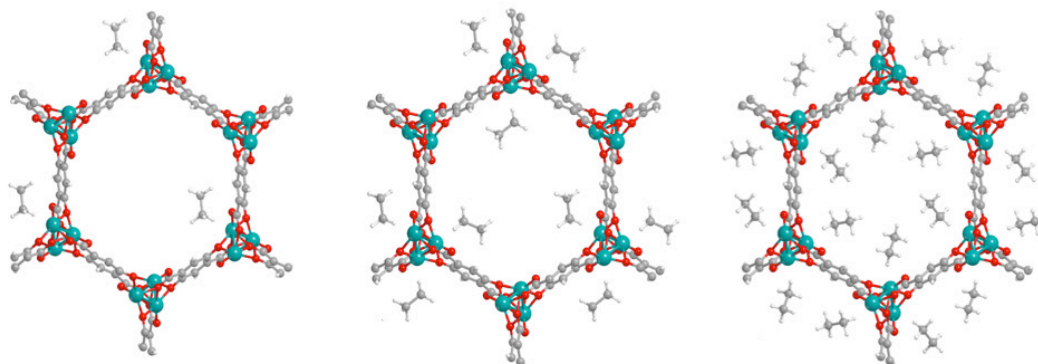


Figure 4.1 C_2H_6 adsorbed in MOF-74-Mg. a) Low loading (1:6) b) Medium loading (1:2), and c) High loading (1:1). The green, gray, red, and white spheres represent magnesium, carbon, oxygen, and hydrogen, respectively.

4.3 PBC: Structural Orientation of Adsorbed Ethylene and Ethane

Figures 4.2 and 4.3 show the orientations of adsorbed ethylene and ethane molecules in MOF-74-Mg. Results refer to fully optimized structures at both B3LYP+D2* and M06 levels. Similar figures for Zn are reported in Figures 4.4 and 4.5. In all cases, the cavities

are fully loaded (six molecules occupy the six open metal sites available per unit cell). The olefins are bound to the open metal site by their C-C double bond rather than C-H bonds, as in paraffin molecules. Geometries for the molecular arrangements are compared with respect to functionals and to the species of MOF.

Attention is devoted to interatomic distances between the metal atom and the two nearest carbons (M-C1 and M-C2) for olefins, and the two nearest hydrogens (M-H1 and M-H2) for paraffins. At first sight, similarities in molecular arrangement of ethylene and ethane across MOFs for the same methods can be identified; however, differences across the methods for the same MOF range from 0.3% to 18%, for the Mg and Zn frameworks, respectively. In all cases, M06 always shortens the distance between the molecules and the metal site (see Figures 3.4-3.7).

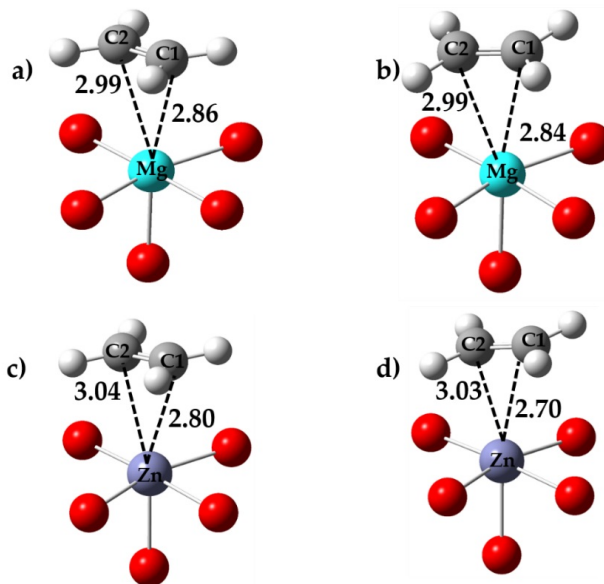


Figure 4.2 PBC: Molecular orientation of adsorbed ethylene corresponding to MOF-74-Mg (a) from B3LYP+D2* (b) from M06; MOF-74-Zn (c) from B3LYP+D2* (d) from M06. Magnesium, zinc, oxygen, carbon, and hydrogen atoms are represented by aqua, purple, red, gray, and white spheres, respectively. Distances are reported in Å.

4.4 PBC: Binding Energies and BSSE Corrected *BE*

The binding nature of light hydrocarbons in MOF-74-M can be interpreted via crystal field theory where the binding molecules form octahedral complexes by occupying the sixth

ligand site at the MOs open metal centers. Computationally, the nature of the electronic structure of the interaction of olefins/paraffins in MOF-74-M can be investigated in several ways. For example, at molecular and bulk level modifications in the highest occupied molecular (HOMO) energy levels, and changes in the density of states (DOS) of the bulk MOFs before and after the adsorption of guest molecules can be used, respectively. *Jung et al.*⁶⁴ showed that the HOMO of paraffins weakly interacts with Fe atoms in MOF-74-Fe with no indication of back donation, while the DOS of the framework significantly changed upon olefins adsorption. This aspect indicates the stronger interaction that olefins, versus paraffins, have with the metal site.

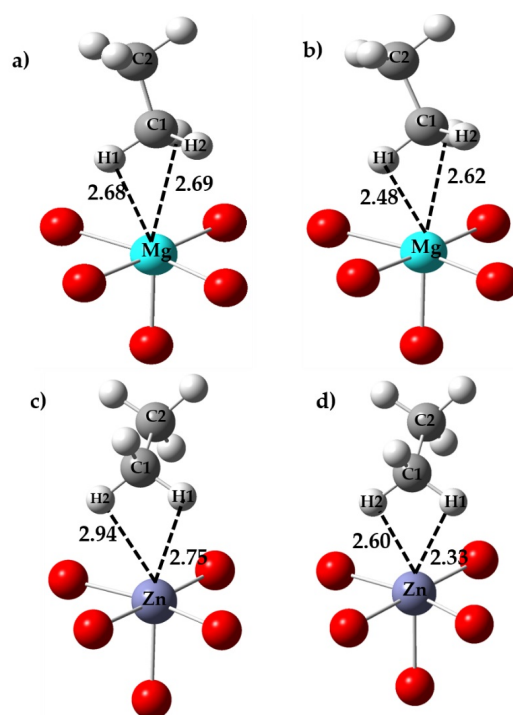


Figure 4.3 PBC: Molecular orientation of adsorbed ethane corresponding to MOF-74-Mg (a) from B3LYP+D2* (b) from M06; MOF-74-Zn (c) from B3LYP+D2* (d) from M06. Magnesium, zinc, oxygen, carbon, and hydrogen atoms are represented by aqua, purple, red, gray, and white spheres, respectively. Distances are reported in Å.

Even though the mentioned computational calculations give some insights about the nature of the interaction of olefins/paraffins with the frameworks, they do not actually provide quantitative information about the strength of the interactions. Such information is accessible through binding energies, heats of adsorption, and molecular frequency shifts.

Table 4.1 shows the calculated binding energies of ethylene and ethane molecules in MOF-74-Mg/Zn at both B3LYP+D2* and M06 levels. Calculations were performed by imposing a full 1:1 molecular loading for a total of six molecules per cavity.

The calculated binding energies of ethylene and ethane corresponding to the two MOFs are found to be comparable, with a maximum deviation of about 3 kJ/mol at both levels of theory. This indicates no significant molecular preference for either metal species explored. Nevertheless, when B3LYP+D2* binding energies are corrected for the basis set superposition error (BE_{BSSE}) results show that both ethylene and ethane tend to *prefer* MOF-74-Mg to MOF-74-Zn by about 2-3 kJ/mol. As well, a general trend is found in which M06 is always affected by a larger BSSE which translates into values for the BE_{BSSE} underestimated by about 1-5 kJ/mol.

Table 4.1 Binding energy (BE), basis set superposition error correction to the BE (BSSE), BSSE corrected BE (BEBSSE), and heats of adsorption computed (PBC) for ethylene and ethane with B3LYP+D2* and M06 in MOF-74-Mg/Zn. Zero-point energies, thermal correction, and lateral interaction are reported in Table 4.2.

Guest Molecule	Metal	kJ/mol				Method
		BE	BSSE	BE_{BSSE}	Heats of Adsorption	
Ethylene	Mg	-52.79	3.26	-49.52	-40.77	B3LYP+D2*
		-49.85	3.96	-45.89	-34.00	M06
	Zn	-51.38	4.69	-46.63	-38.36	B3LYP+D2*
		-53.85	7.14	-46.16	-33.68	M06
Ethane	Mg	-38.89	3.24	-35.65	-26.61	B3LYP+D2*
		-35.21	4.03	-31.18	-22.79	M06
	Zn	-39.58	5.56	-34.02	-27.40	B3LYP+D2*
		-39.99	7.33	-32.66	-24.04	M06

4.5 PBC: Heats of Adsorption of Ethylene and Ethane

In order to more accurately determine the separation efficiencies of the two MOFs, the zero-point energy (ΔZPE) and the thermal energy (ΔTE) corrections were also estimated, allowing for the determination of the heats of adsorption for the molecules (Equation 3.4). This investigation seeks to address how strongly the molecules interact with the metal in the MOFs, and to determine the difference in adsorption energy between alkanes and

alkenes, providing quantitative information as to which MOFs have the best potential for sorption selectivity. Table 4.1 reports binding energies and heats of adsorption for ethylene and ethane, Table 4.3 lists their relative changes in several different MOF-74-M species. When values for BE_{BSE} are compared, results show that the two MOFs have a comparable degree of separation (~ 14 kJ/mol). However, when results are corrected to obtain heats of adsorption, MOF-74-Mg seems to be favored over its Zn analogous with an energy separation gain equal to 3.2 kJ/mol (B3LYP+D2*) and 1.57 kJ/mol (M06) for ethylene over ethane. Overall, given this small difference in heat of adsorption, it can be concluded that both MOFs show a similar and appreciative potential toward separation.

4.6 PBC: Spatial Orientation of Adsorbed C₂, C₃, and C₄ Molecules

As reported in previous chapter,¹¹³ the calculated cell parameters from PBC optimized MOF-74-Mg/Zn bulk structure are in an excellent agreement with both experimental and other theoretical results with the c/a ratio remaining consistent within very small differences across the different loadings (less $\sim 2\%$) for both MOFs.

Table 4.2 PBC: Zero-point energy (ZPE), thermal correction (TC), and molecular lateral interaction contribution from PBC calculations for full loaded (six molecules) MOF-74-Mg/Zn. All energies are reported in kJ/mol.

Molecule	Metal	ΔZPE	ΔTE	Lateral Interaction	Method
Ethylene	Mg	5.34	3.41	-1.17	B3LYP+D2*
	Zn	4.78	3.50	-1.02	
Ethane	Mg	4.62	4.42	-3.30	
	Zn	4.78	1.84	-2.40	
Ethylene	Mg	9.21	2.74	-0.77	M06
	Zn	9.92	2.56	-0.10	
Ethane	Mg	5.15	3.71	-0.39	
	Zn	5.48	3.13	-1.37	

As mentioned, with frozen MOF approach, all the atoms belonging to the frameworks were kept fixed in their original bulk configurations while the intramolecular distances within the molecules and the molecular relative distances from the adsorption open metal sites were allowed to relax. The attention is therefore devoted to the analysis of the geometrical

orientations across the different loadings in relation to the distances between the metal atom and the nearest two carbon atoms (M-C1 and M-C2) for olefins, and the nearest two hydrogen atoms (M-H1 and M-H2) for paraffins. Figure 4.4 shows the orientation of the six hydrocarbons adsorbed in MOF-74-M. Table 4.4, and 4.5 report the full assessment of the atomic distances with respect to Mg, and Zn for all the species.

Table 4.3 PBC: Comparison between ethylene and ethane heats of adsorptions and their corresponding changes in MOF-74-M (M=Mg, Zn, Fe, Mn, Co) from various computational and experimental works. Numbers in square brackets correspond to binding energies. Numbers in parenthesis correspond to heats of adsorption.

Metal	kJ/mol		Method
	H_{ads}^0	ΔH_{ads}^0	
Mg	(-40.77, -26.61)	-14.16	B3LYP+D2* ²
	(-34.00, -22.79)	-11.21	M06 ^a
	(-43, -27)	-16.00	Diffusion-Kinetics ¹¹⁶
	[-40, -35]	-5.00	vdW+DF2+U ⁵⁸
	(-43, -27.5)	-16.50	NPD ¹¹⁷
Zn	(-38.36, -27.40)	-10.96	B3LYP+D2* ^a
	(-33.68, -24.04)	-9.64	M06 ^a
	(-38.5, -25.2)	-13.30	NPD ¹¹⁷
Fe	[-40, -35]	-5.00	vdW+DF2+U ⁵⁸
	[-41.4, -22.5]	-18.40	R(PBE)+D2+U ⁶⁴
	(-45, -25)	-20.00	NPD ¹¹⁸
	(-44, -26.50)	-17.50	NPD ¹¹⁷
Mn	(-44.5, -27)	-17.50	NPD ¹¹⁷
Co	(-43.5, 25.1)	-18.40	NPD ¹¹⁷

Overall, while no dramatic differences in orientation are observed across olefins in either MOFs, averaged M-C1/C2 distances range from 3.007 to 3.143 Å for high and low loadings, respectively, corresponding to a 4% increase in distance from the metal site. In general, olefins adsorbed on Zn have the tendency to lie further from the metal than with respect to Mg. This trend may be related to the difference in ionic radii for five-fold coordinated Mg and Zn for which values of 0.66 Å, and 0.68 Å are reported, respectively.¹¹⁹ As for paraffins, the long-range force contributions acting between the two hydrogen atoms pointing toward the metal sites is reflected by the more compact geometrical arrangement that the host-guest adducts show. A comparison with the results obtained in our previous

² this work, XRD = X-ray diffraction, NPD= Neutron Powder Diffraction

work where cluster models were employed (chapter 3),¹¹³ reveals a consistent decrease in the adsorbate-metal distance; such trend, as discussed later, can be ascribed to the presence of the MOFs' chemical environment which is mostly neglected when cluster models are employed.

4.7 Binding Energies (BE), BSSE Corrections, and Dispersion Contributions for C₂, C₃, and C₄ Adsorbed in MOF-Mg/Zn

While the calculated binding energies were found not to be affected by different molecular loadings in the case of the smallest hydrocarbons (ethane, and ethylene), for the largest molecules (butane, and butylene) the change in binding energies related to the different loadings reaches the non-negligible amount of 8 kJ/mol. Table 4.6 and Table 4.7 list binding energy (BE), basis set superposition error (BSSE) correction, BSSE corrected BE, and lateral interaction (LI) computed for adsorbed molecules in both the frameworks with respect to the three different molecular loadings.

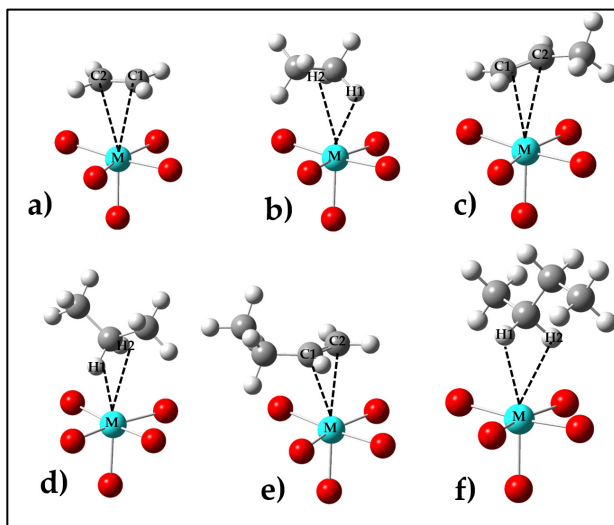


Figure 4.4 Molecular orientation of adsorbed ethylene (a), ethane (b), propene (c), propane (d), butane (e), and butylene (f) corresponding to high loaded MOF-74-M. Metal atom, oxygen, carbon, and hydrogen atoms are represented by aqua, red, gray, and white sphere respectively. Distances are reported in Angstrom. Distance for all the molecules are reported in Table 4.4, and Table 4.5.

The BSSE corrections for ethane, and ethylene are comparable with those published in our previous work where PBC results for the fully relaxed structures (*i.e.*, MOFs and molecules

allowed to dynamically relax) are reported (Chapter 3 section 3.3.4)¹¹³. Also, within this approach, the BSSE contributions referring to the Mg framework are consistently smaller than those for Zn, indicating the possibility of further improving the accuracy of the results by adopting a higher-level basis set. As far as Mg goes, the only oddity is reported in the case of a full C₄H₁₀ loading for which a BSSE close to 8 kJ/mol was obtained. This seems to be related to the dimension of the molecules which also clearly strongly influences the LI (+13.5 kJ/mol). The same behavior can be observed for the adsorption on Zn.

Table 4.4 Interatomic distances between open metal sites to the nearest two hydrogen atoms (M-C, M=Mg, Zn) for olefin molecules adsorbed at the open metal sites with respect to three different loadings. See also Figure 4.2.

Olefin	Metal	Distances (Å)	Loadings		
			High	Medium	Low
C ₂ H ₄	Mg	M-C1	2.948	2.960	2.927
		M-C2	3.073	3.076	3.121
	Zn	M-C1	2.943	2.929	2.940
		M-C2	3.233	3.238	3.227
C ₃ H ₆	Mg	M-C1	2.987	2.975	2.976
		M-C2	3.300	3.320	3.314
	Zn	M-C1	2.996	2.997	2.991
		M-C2	3.392	3.388	3.397
C ₄ H ₈	Mg	M-C1	2.958	2.976	2.971
		M-C2	3.142	3.318	3.138
	Zn	M-C1	2.986	3.030	3.022
		M-C2	3.172	3.164	3.166

Figure 4.5 shows an overall comparison of the role played by the dispersion contribution across the different computational models: from the smallest (3MB) to the largest (6MB) cluster models¹¹³ to the different loadings as per PBC calculations. For both the frameworks, dramatic differences can be observed in the increasing of the dispersion contribution with respect to the size of the adsorbed molecule. While such contribution remains stable within 10 kJ/mol for the small C₂ species, it doubles for C₃ to then reach a value as big as 40 kJ/mol in the case of the biggest hydrocarbon, C₄H₁₀.

Table 4.5 Interatomic distances between open metal sites to the nearest two carbon atoms (M-H, M=Mg, Zn) for paraffin molecules adsorbed at the open metal sites with respect to three different loadings. See Figure 4.2.

Paraffin	Metal	Distances (Å)	Loadings		
			High	Medium	Low
C ₂ H ₆	Mg	M-H1	2.711	2.644	2.627
		M-H2	2.717	2.687	2.685
	Zn	M-H1	2.709	2.849	2.758
		M-H2	2.918	2.857	2.877
C ₃ H ₈	Mg	M-H1	2.360	2.446	2.456
		M-H2	3.103	2.831	2.819
	Zn	M-H1	2.289	2.562	2.563
		M-H2	3.461	3.996	4.002
C ₄ H ₁₀	Mg	M-H1	2.641	2.692	2.697
		M-H2	2.847	2.755	2.762
	Zn	M-H1	3.220	2.635	2.643
		M-H2	3.495	3.067	3.073

These results suggest that the models employed strongly effect the quantitative results on the binding energy this has a major impact on the validity of the conclusions drawn to discuss the potential capabilities of the investigated materials. This comment applies particularly to the choice of a molecular cluster model due to the lack of the chemical environment provided by the framework, and therefore not experienced by the adsorbed guest molecules. This contribution plays a dramatic role in the determination of the binding energies calculated at the molecular cluster level when compared to results obtained with PBC are imposed. Overall, the underestimation of the binding energy ranges from 5 kJ/mol to 25 kJ/mol and 4 kJ/mol to 20 kJ/mol from the smallest C₂ to the biggest C₄ hydrocarbon molecule, respectively for MOF-74-Mg and MOF-74-Zn (Figure 4.6). In order to provide a common baseline for the comparison of the obtained results, Table 4.9 lists the differential binding energies for all the three different loadings in the periodic framework cavity together with the results for the two cluster models. As discussed above, while the effect of the cluster size is negligible for C₂, it becomes more pertinent for the larger molecules.

Table 4.6 Binding energy (BE), basis set superposition error (BSSE) correction to the BE, BSSE corrected BE, and lateral interaction (LI) computed for adsorbed molecules in MOF-74-Mg with respect to different loadings.

Molecules	Loading	kJ/mol			
		BE	BSSE	BE(BSSE)	LI
CH ₄	6	-29.12	3.08	-26.04	2.07
	3	-28.49	3.23	-25.27	1.86
	1	-27.61	2.03	-25.58	0.00
C ₂ H ₂	6	-45.90	4.09	-41.80	1.59
	3	-46.20	4.40	-41.79	1.06
	1	-48.25	4.47	-43.78	0.00
C ₂ H ₄	6	-50.08	3.08	-46.99	1.58
	3	-49.52	3.14	-46.39	0.29
	1	-49.16	3.24	-45.92	0.00
C ₂ H ₆	6	-38.26	2.96	-35.30	2.08
	3	-36.89	3.04	-33.85	0.69
	1	-36.57	3.06	-33.51	0.00
C ₃ H ₆	6	-65.14	4.45	-60.69	2.76
	3	-61.98	4.57	-57.42	0.82
	1	-61.62	4.67	-56.95	0.00
C ₃ H ₈	6	-49.51	3.96	-45.56	5.16
	3	-44.75	3.80	-40.95	1.38
	1	-44.06	3.88	-40.18	0.00
C ₄ H ₈	6	-71.20	4.95	-66.26	7.80
	3	-66.06	4.85	-61.20	1.17
	1	-64.93	4.92	-60.00	0.00
C ₄ H ₁₀	6	-62.18	7.72	-54.46	13.52
	3	-55.87	5.05	-50.82	4.86
	1	-54.53	5.14	-49.39	0.00

On the contrary, when PBC results are examined for the different loading, a net decrease in differential binding energy can be appreciated already for C₂ species. Referring to the two models that are most comparable and for which the lateral interaction contribution is absent (*i.e.*, the low loading PBC model, and the 3 MB -the smallest- molecular cluster model) allows one to better appreciate the differences in the results. These show a consistent decrease in the values for the differential binding energies for all the molecules

(from the negligible 0.90 kJ/mol up to the rather significant 5.3 kJ/mol) for both the MOFs, with the only exception of MOF-74-Zn/C4 (1.20 kJ/mol). This unique oddity in the trend, though, is likely to be due to the larger BSSE consistently observed for the Zn-based framework.

Table 4.7 Binding energy (BE), basis set superposition error (BSSE) correction to the BE, BSSE corrected BE, BE (BSSE) and lateral interaction (LI) computed for adsorbed molecules in MOF-74-Zn with respect to different loadings.

Molecules	Loading	(kJ/mol)			
		BE	BSSE	BE(BSSE)	LI
CH ₄	6	-28.78	2.90	-25.88	2.38
	3	-28.64	2.36	-26.28	1.79
	1	-29.90	1.64	-28.26	0.00
C ₂ H ₂	6	-44.32	4.05	-40.27	1.88
	3	-44.41	3.03	-41.38	1.41
	1	-44.41	2.28	-42.13	0.00
C ₂ H ₄	6	-47.68	5.34	-42.34	1.63
	3	-46.92	5.32	-41.60	0.41
	1	-46.75	5.33	-41.42	0.00
C ₂ H ₆	6	-38.05	5.19	-32.86	1.62
	3	-35.02	5.25	-29.77	0.27
	1	-34.62	5.24	-29.38	0.00
C ₃ H ₆	6	-66.35	7.21	-59.14	2.81
	3	-63.07	7.06	-56.01	0.81
	1	-62.51	7.12	-55.39	0.00
C ₃ H ₈	6	-54.10	7.45	-46.65	4.28
	3	-50.40	7.04	-43.36	1.17
	1	-49.34	6.94	-42.40	0.00
C ₄ H ₈	6	-72.54	7.59	-64.95	8.17
	3	-66.06	7.56	-58.50	1.37
	1	-64.73	7.46	-57.27	0.00
C ₄ H ₁₀	6	-57.14	7.06	-50.08	16.09
	3	-51.55	6.95	-44.60	3.09
	1	-49.64	6.92	-42.72	0.00

4.8 Effect of Lateral Interaction on the Choice of the Model, and Molecular Loading

As expected, the intermolecular lateral interaction (LI) energy is found to be repulsive, ranging from 2 to 16 kJ/mol from the smallest C₂ to the biggest C₄ hydrocarbon molecule, respectively. Not surprisingly, no dramatic differences are observed in the LI contributions for the smallest molecules with respect to the different loadings with maximum values in the range of 1.50-2.00 kJ/mol for the 1:1 loading. This can be explained by invoking intuitive geometrical and steric hindrance considerations referring to the dimension of these molecules with respect to that of the MOF cavity; these are in fact different enough to allow the framework to accept a full molecular loading without having the molecules interact with each other.

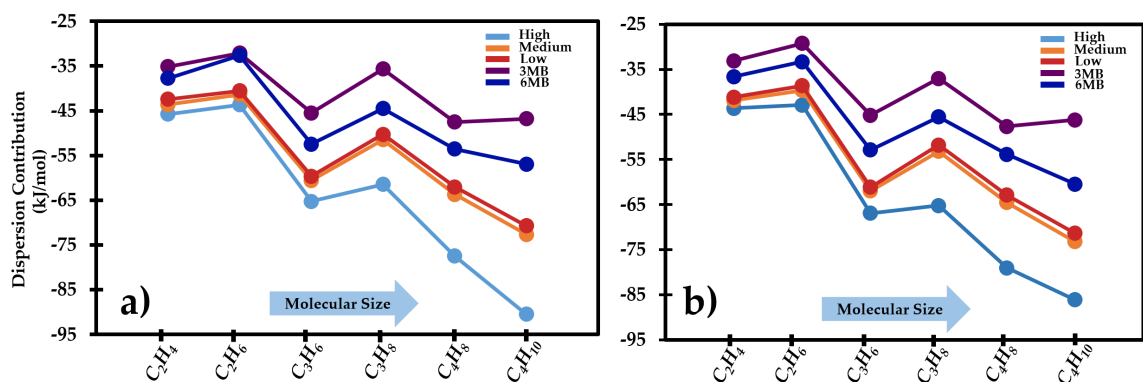


Figure 4.5 Dispersion contribution reported for the three loading cases, and for the 3MB and 6MB molecular cluster models for (a) MOF-74-Mg (b) MOF-74-Zn.

The closest distance between the two carbon atoms of the adsorbed molecules confirms the results: 4.01 Å for ethane, and 4.37 Å for ethylene. LI becomes more significant for the C₃ species, effected by contributions ranging from 2.70 kJ/mol up to almost 5.20 kJ/mol reflecting molecular distances of 3.92 Å and 4.22 Å for propane, and propene, respectively for the full loading scenario. Nevertheless, LI contributions are almost negligible in the case of the 1:2 loading where molecules are over 5.00 Å apart. As expected, given the vicinity of the molecules (3.49 Å, and 3.62 Å), the most dramatic results are reported for butane, and butylene for which values ranging from 8.00 up to 16.00 kJ/mol are observed.

This indicates the potential for competition among the largest molecules with respect to the adsorption into the MOF cavity. Investigations on the diffusion process for these species, and a comparison with the behavior observed for the smallest ones is discussed in the next chapter.

4.9 Heat of Adsorptions (ΔH^0) for C₂, C₃, and C₄

In order to more accurately determine the separation efficiencies of the two MOFs, zero-point energy (ΔZPE) and thermal energy (ΔTE , determined at room temperature) corrections were estimated; this allows for determining the heats of adsorption as per Eq. 4. The inclusion of these corrections not only provides a more complete information about

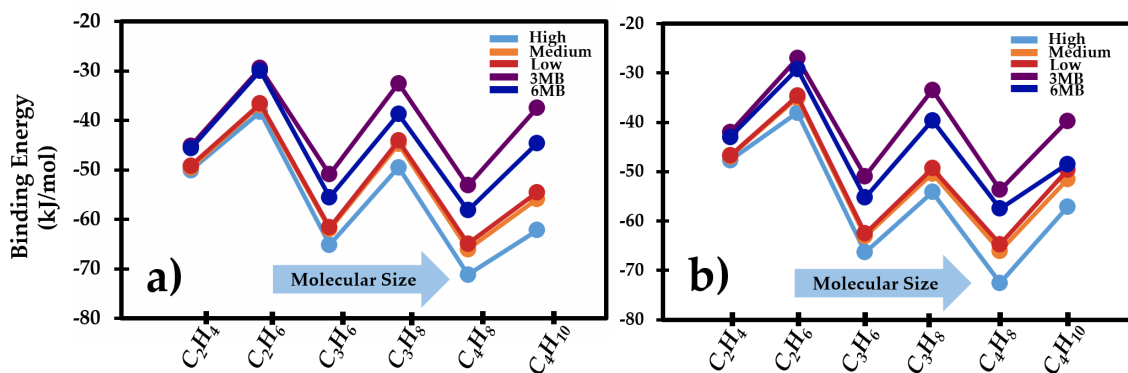


Figure 4.6 Binding energies reported for the three loading cases, and for the 3MB and 6MB molecular models from both MOFs

olefins-paraffins behavior in the MOFs, but it is a result that can be directly compared with experimental evidence. A comparison for heats of adsorption determined in this work for the full loading scenario, and available experimental values is reported in Table 4.10. The overall excellent agreement demonstrates the capability of the applied method to reliably estimate the behavior of the molecules in the MOFs within the experimental error bar, and it provides a good mean for the prediction of the energetic behavior of those hydrocarbons for which experimental evidence is still lacking. Nevertheless, the most compelling conclusion that should be drawn from the reported results is that this work provides for the first time the most adequate approach to correctly confirm and predict heats of adsorption

for hydrocarbons in MOFs.

Table 4.8 Olefin/paraffin differential binding energies for C2, C3 and C4 hydrocarbons for different loading sizes and two molecular cluster models for MOF-74-Mg/Zn.

Olefin/Paraffin	Metal	Differential binding energies (kJ/mol)				
		High	Medium	Low	3MB	6MB
C ₂ H ₄ /C ₂ H ₆	Mg	-11.82	-12.64	-12.59	-15.68	-15.74
	Zn	-9.62	-11.90	-12.13	-15.00	-13.77
C ₃ H ₆ /C ₃ H ₈	Mg	-15.63	-17.23	-17.56	-18.42	-16.82
	Zn	-12.24	-12.68	-13.18	-17.46	-15.62
C ₄ H ₈ /C ₄ H ₁₀	Mg	-9.02	-10.19	-10.39	-15.69	-13.61
	Zn	-15.40	-14.51	-15.09	-13.95	-9.02

Table 4.9 Binding energies (BEBSSE), zero-point energy (Δ ZPE), and thermal energy correction (Δ TE) providing heats of adsorption (Δ H) of C2-C4 for high molecular loadings in both MOF-74-Mg/Zn. Available experimental results are also reported¹¹⁶⁻¹¹⁷ to assess the differential enthalpy for the same molecule between the two MOFs (column 8), and for the same MOF with respect to the olefin/paraffin pairs (last column). All the energies are reported in kJ/mol.

Guest Molecule	Metal	kJ/mol						
		BE _{BSSE}	ΔZPE	ΔTE	ΔH		Differential ΔH Cal. (Exp.)	
					Cal.	Exp.	Same molecule different MOFs	Same MOF olefin-paraffin pair
CH ₄	Mg	-26.04	4.69	3.32	-18.04	-18.0 ¹²⁰ -18.5 ¹¹⁸	+2.38 (+1.1) ^{107, 120}	Mg: -13.53 (17.0) ¹²⁰⁻¹²¹ Zn: -10.15 (-5.9) ¹²⁰⁻¹²¹
	Zn	-25.88	3.65	1.81	-20.42	-19.1 ¹⁰⁷ -18.3 ¹¹⁸		
C ₂ H ₂	Mg	-41.81	7.99	2.25	-31.57	-35.0 ¹²¹	-1.0 (-10.0) ¹²¹	
	Zn	-40.27	7.10	2.60	-30.57	-25.0 ¹²¹		
C ₂ H ₄	Mg	-46.99	5.29	3.40	-38.31	-42.6 ¹¹⁶ , -41.3 ¹¹⁷	-2.98 (-2.80) ¹¹⁷	Mg: -11.86 (-13.80) ¹¹⁷ , (-7.2) ¹¹⁶ Zn: -10.95 (-13.00) ¹¹⁷
	Zn	-42.34	4.39	2.61	-35.33	-38.50 ¹¹⁷		
C ₂ H ₆	Mg	-35.30	4.29	4.55	-26.45	-35.4 ¹¹⁶ -27.5 ¹¹⁷	-2.07 (-2.00) ¹¹⁷	
	Zn	-32.86	3.67	4.82	-24.38	-25.50 ¹¹⁷		
C ₃ H ₆	Mg	-60.69	4.77	3.82	-52.11	-60.50 ¹¹⁶ -48.1 ¹¹⁷	-2.49 (+0.10) ¹¹⁷	Mg: -14.53 (-12.5) ¹¹⁷ , (-26.6) ¹¹⁶ Zn: -13.63 (-12.2) ¹¹⁷
	Zn	-59.14	6.07	3.44	-49.62	-48.2 ¹¹⁷		
C ₃ H ₈	Mg	-45.56	3.39	4.59	-37.58	-33.90 ¹¹⁶ -35.6 ¹¹⁷	-1.59 (+0.40) ¹¹⁷	
	Zn	-43.36	2.65	4.72	-35.99	-36.0 ¹¹⁷		
C ₄ H ₈	Mg	-66.26	5.84	3.69	-56.73	-	-1.28	Mg: -12.10 Zn: -14.76
	Zn	-64.95	5.78	3.72	-55.45	-		
C ₄ H ₁₀	Mg	-54.46	6.37	3.47	-44.63	-	-3.94	
	Zn	-50.08	5.75	3.64	-40.69	-		

In fact, it shows that the good agreement between the binding energies (Δ E) obtained with

the use of a molecular cluster approach and the experimental heats of adsorption (ΔH) is accidental and arises from compensation of errors in the neglecting of: (i) the chemical environment provided by the MOF, and (ii) the lack of ΔZPE and ΔTE corrections. In particular, the latter contributions allow for determining the proper thermodynamic property of interest.

4.10 Summary

Using a DFT-based first-principle approach able to account for the long-range interaction between the adsorbed molecules and the open metal site, PBC calculations on periodic structures of MOF-74-Mg/Zn were performed to investigate the role of the inclusion of the MOF chemical environment and the influence of the lateral interaction on the binding energies of adsorbed C₂-C₄ hydrocarbons molecules. For these purposes, three different molecular loadings were imposed. The inclusion of these effects allows for a more complete appreciation of the importance of accounting for the presence of the framework, which is otherwise partially excluded when molecular cluster models are adopted. In addition, binding energies corrected for basis set superposition error (BSSE) are determined and are further corrected to include the contributions due to zero-point energy and finite-temperature thermal energy which allows for a comparison of calculated results (enthalpies) with available experimental heats of adsorption.

Based on our computed binding energies, the inter-molecular distances between small molecules are large enough to only minimally influence the results even in the high loading case. As molecular size increases, however, a clear trend is observed where the binding energy increases with the increasing of the repulsive lateral interaction, which is reported to be as high 16 kJ/mol for butylene, the biggest hydrocarbon considered. It is worth stressing that inability to accurately account for dispersions contribution may play a significant role in the underestimation of binding energies calculated from molecular cluster models when compared to that obtained within PBC approaches.

This work shows, how the inclusion of the proper chemical environment plays a crucial role for a better estimation of the binding energies of molecules adsorbed in MOFs. In addition, PBC models allow for the inclusion of energetic contributions of vital importance for a fair comparison with experimental heats of adsorption.

5 Results: Spectroscopic Properties of C₁-C₂ Hydrocarbon Molecules in MOF-74-Mg

5.1 Introduction

MOFs, despite their interesting potential industrial applications, are subjected to structural instability under certain thermal and hydrothermal conditions.¹²² Recent studies have pointed out such issues must be evaluated and addressed before MOFs are used in real world practical applications. For instant, one of the major concern for using MOFs in gas storage and separation is their chemical instability under humidity.¹²³⁻¹²⁴ Despite their outstanding promising performance in H₂, and CO₂ storage, X-ray diffraction studies have shown that some commonly investigated MOFs including MOF-5 and MOF-177 have failed to maintain their structural integrity under the presence of water molecules.¹²⁵⁻¹²⁷ According to *Greathous et al.*, molecular dynamic modeling of MOF-5-Zn showed structural instability in the presence of the water molecule which weaken the interaction between metal atom inorganic bricks and oxygen atoms of the *ligand*.¹²⁷ This is an excellent agreement with an experimental work of *Saha et al.* that demonstrated the strong interaction between water to the frame-works can result in a complete distraction of the MOF structure, leading to hydrolysis and formation of the original *linkers* and metal oxides.¹²⁸ Some recent investigation on the potential application of olefin-paraffin gas mixture separation in MOF-74-Mg/Co/Fe/Ni,^{48, 60-62, 113, 129} have shown promising impression. Though MOFs have shown extraordinary volumetric gas uptake, decayed adsorption is observed and assumed to be resulting in polymerization reaction in some cases.¹³⁰

*The material contained in this chapter was previously published in Theoretical Chemistry Accounts, in Springer Journals 2018, 137(42), 1-18 by Gemechis Degaga and Loredana Valenzano. See Appendix H for the reprint permission.

Understanding the interaction of molecules of interest is an essential to determine the practical application of MOFs. Among the experimental techniques used to assess stability, reversibility, and the potential of MOF toward molecular recognition and separation, spectroscopic techniques such as IR, Raman, and UV/Vis are of great utility. In particular, the combined use of Langmuir isotherm curves able to determine heats (*i.e.*, enthalpies) of adsorption and spectroscopic techniques able to shed light on the nature of the guest/host interaction, have been used experimentally to describe at microscopic level situations ruled by electrostatic attractive forces and also by long-range dispersion forces. When possible, the additional information provided by the use of theoretical/computational models (from quantum mechanical electronic structure based methods to classical dynamics molecular simulations) have been proved not only to enrich the interpretation of experimental evidence, but have been also used as powerful predictive tools^{56, 113, 131-132}. Despite their limitations in determining the reactive sites in MOFs, IR and RAMAN studies have been used extensively in investigating the interaction of small molecules with MOF structures.¹³³⁻¹³⁴ It has been demonstrated that interaction of molecules to the reactive sites in the MOF structure can be altered by the presence of other similar molecules (loading sizes) due to intermolecular interactions.^{59, 129} In their NMR chemical shielding study of H₂, CO₂ and H₂O in MOMF-74-Mg, Lopez et al showed significant dependence of change in NMR chemical shielding on molecular loading sizes, that can be measurable experimentally, despite their smaller molecular sizes with respect to inter-molecular distances.

In this regard, this work is thought as a practical and alternative guide to the interpretation of experimental IR spectra of light hydrocarbons in MOF-74-Mg/Zn and, as such, it provides an original effort to describe IR *signature* associated with the presence of C₁-C₄ hydrocarbon molecules in the MOF-74-Mg cavity. The investigation is conducted at an electronic structure density functional theory (DFT) level as implemented in the Crystal14 program based on a linear combination of atomic orbital (LCAO) approach⁶⁵. After a description of the computational methods employed and their motivations, results are described in terms of: (i) Enthalpies of adsorption; (ii) Geometrical arrangement of the

molecules with respect to the open metal site and the organic *linkers* of the framework; (iii) IR spectra described in terms of the molecular vibrational frequency shifts observed with respect to the molecules in the gas phase; and, (iv) IR intensities. In order to provide an even more valuable contribution to the community of experimental spectroscopists, different molecular loadings and their impact on the calculated intensities together with the appearance of original band features are also described.

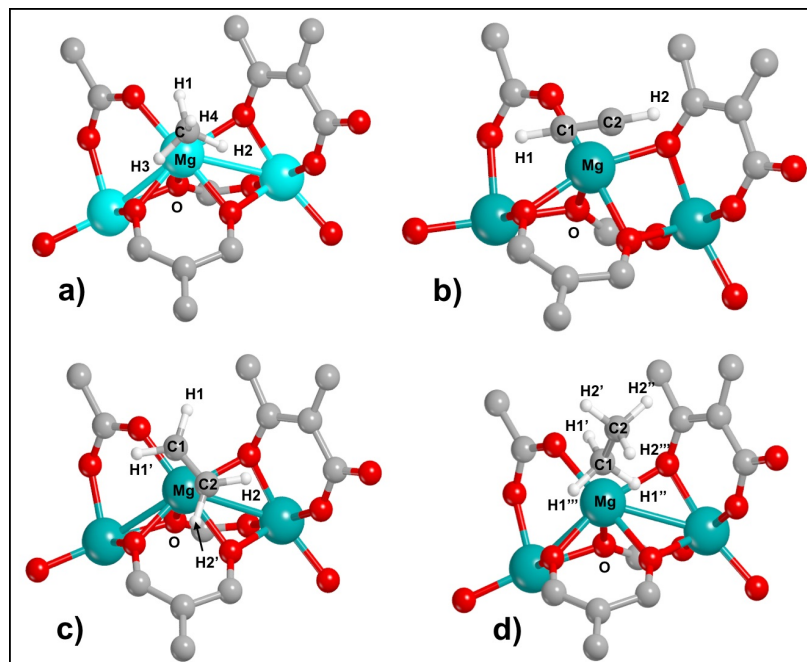


Figure 5.1 Individual general molecular arrangements for the molecules in MOF-74-Mg: (a) Methane; (b) Acetylene; (c) Ethylene; (d) Ethane. Values for the indicated bond lengths and angles are reported in Tables 5.2, 5.3, 5.4, 5.5, respectively, and discussed in each subsection.

5.2 Computational Methods and Models

First principle density functional theory PBC calculations were performed by employing the hybrid-GGA B3LYP functional⁸⁴⁻⁸⁵ *a posteriori* corrected with a semi-empirical contribution able to take into account the long range $1/r^6$ dispersion contribution⁹⁵. The Crystal14 program^{101, 114} was used where the original Grimme parametrization for the molecular species was modified to include the effect of periodic boundary conditions as reported in the work of *Valenzano et al.*¹⁰⁸. The adopted values for the modified atomic parameters were reported in previous publications^{113, 132} (see Table 3.1). While keeping

the computational cost unchanged, the functional, labeled as B3LYP-D2* has been previously successfully adopted^{56-57, 108, 113, 132, 135} to describe properties of crystalline materials involving long range (*i.e.*, London) dispersion forces¹³⁶. As previously in chapter 3 and Chapter 4,^{113, 132} a TZVP basis set was chosen for Mg, while for H, C, and O, the standard Ahlrichs TZP basis set were adopted.¹³⁷

Table 5.1 CH₄: Atomic distances (Å) and angles (°) for the different molecular loadings in the MOF. Calculated values for the molecule in the gas phase are 1.0899 Å (CH), and 109.471° (<HCH). Symbols for atoms with respect to the MOF are described in the text.

Geometrical Feature	Loading		
	1:1	1:2	1:6
C-H1	1.0901	1.0902	1.0905
C-H2	1.0910	1.0910	1.0914
C-H3	1.0905	1.0904	1.0910
C-H4	1.0891	1.0890	1.0890
Mg-C	3.0087	3.0044	3.0096
Mg-H1	2.8506	2.8437	2.8511
Mg-H2	2.8385	2.8346	2.8396
Mg-H3	2.8850	2.8849	2.8861
∠H1-C-H2	110.339	110.386	110.329
∠H1-C-H3	111.608	110.636	110.601
∠H1-C-H4	108.603	108.353	108.375
∠H1-C-H4	108.286	108.268	108.310
∠H2-C-H4	108.361	108.353	108.375
∠H3-C-H4	108.603	108.572	108.561
∠O-Mg-C	168.834	168.778	168.832

An XLGRID (75,974) pruned-grid was used for the numerical integration of the *exchange-correlation* term.⁶⁵ Full periodic boundary condition (PBC) geometry relaxation where both lattice parameters and atomic positions were allowed to relax, was performed on the 3D bulk structure of MOF-74-Mg starting from its initial experimental geometry.¹¹⁰ After full geometry relaxation, vibrational frequency calculations conducted within the harmonic approximation, were performed on the molecular adducts only. Although this choice may seem to impose a crude approximation to the calculations potentially raising legitimate doubts about their reliability, it can be justified by a few practical, yet important aspects which allow for making the calculations tractable, still preserving the required level of accuracy. In fact: (i) Given the size of the adsorbed molecules and the loss of molecular symmetry during the frequency calculation task; (ii) Observing that the very few imaginary

frequencies are negligible in value and are therefore not expected to influence the spectroscopic region of interest; (iii) Observing that the atomic metal nearest-neighbors vibrates at frequencies far from the molecular region of interest; (iv) Taking into consideration the good agreement between the enthalpies of adsorption obtained for ethane, ethylene, propane, propylene, butane, and butylene as discussed in¹³² and successfully compared with experimental heats of adsorption, we believe that our approximated approach is reliable in providing a valuable interpretation of the spectroscopic features for the presence of hydrocarbons in MOF-74-Mg. Furthermore, we will show how energetics for methane and acetylene provide for an additional valuable checkpoint. Frequency bands and peak positions are reported both according to their raw calculated values and scaled by a 0.965 which takes into consideration the effect of the adopted basis set.¹³⁸

Table 5.2 C₂H₂: Atomic distances (Å) and angles (°) for the different molecular loadings in the MOF. Calculated values for the molecule in the gas phase are 1.0633 Å (CH), 1.1981 Å (CC), and 180.000° (<HCC). Symbols for atoms with respect to the MOF are described in the text.

Geometrical Feature	Loadings		
	1:1	1:2	1:6
C1-H1	1.0640	1.0641	1.0635
C2-H2	1.0644	1.0647	1.0642
C1-C2	1.1994	1.1996	1.1994
∠H1-C1-C2	179.264	179.375	179.272
∠C1-C2-H2	178.678	178.646	178.650
C1-Mg	2.8873	2.9004	2.8868
C2-Mg	2.9922	3.0026	2.9912
∠O-Mg-C1	155.390	155.546	155.381
∠O-Mg-C2	173.049	172.049	173.047

Throughout the calculations, SCF convergence thresholds were set to 10⁻⁸ and 10⁻¹⁰ Ha for geometry optimization and vibrational frequency calculations, respectively. The Monkhorst-Pack⁹¹ shrinking factors for the reciprocal space sampling were set to 2 corresponding to eight k-points for the Hamiltonian matrix diagonalization in the reciprocal space. Tolerances for the one- and two-electron integrals were set to 7 7 7 7 18⁶⁵. Three different molecular loadings were explored (Figures 4.1), corresponding to: (i) A full (1:1) loading with six molecules adsorbed on each of the six open metal sites in the

MOF unit cell; (ii) A medium (1:2) loading with three molecules adsorbed at each other available open metal site; (iii) A low (1:6) loading with only one single molecule adsorbed on only one of the six available adsorption sites. While the first described scenario allows for preserving the overall hexagonal symmetry of the system (6 symmetry operators -still, although, breaking the molecular symmetry of the adsorbates), in the other two situations symmetry is partially and fully lost and symmetry operators reduce to three and one, respectively.

The intensity I_p for each of the p -th IR active mode is determined as the square of the first derivative of the dipole moment with respect to the normal mode coordinate Q_i which is then multiplied to the degeneracy d_i of the p -th mode itself as in Equation 2.83. Strictly related to the determination of the IR intensities, is the concept of Born effective charges which arise from the polarization associated with the atomic displacements necessary to obtain the vibrational spectrum; in simpler words, Born effective tensor charges Z_{d_1, d_2}^* can intuitively be seen as the charge that close-by atoms exchange when they vibrate, and for this reason they are often also indicated as *dynamic charges*. As such, they explicitly appear in the expression of the dynamical mass-weighted Hessian matrix as a proportionality coefficient between the polarization per unit cell (along a certain generic d_1 direction) and the displacement of an atom along the perpendicular direction d_2 . It is important to stress that, although this is a general definition that applies also when a macroscopic external electric field is applied to the system, here we are interested in the situation referring to conditions when a zero-electric field is present and for which the change in polarization arises exclusively from the atomic displacements allowing for the determination of IR intensities. Born effect charge tensors are obtained from well localized Wannier functions as reported and used in several literatures.^{101, 139-143} As a conclusive comment, it is noteworthy to mention the fulfillment of the *sum rules* which provide indications about the proper convergence of the calculations.

First, the presence of sporadic few small negative eigen-frequencies was mentioned before, and it does not constitute a concern for the discussed reasons. The second sum rule refers to the requirement of the neutrality for the sum of the Born effective charges which ensures

the reliability of the calculated IR intensities. Although not fully fulfilled (with values spanning from 0.1 to 0.2, and one case only as big as 0.5) calculated IR intensities are still expected to be accurate.¹⁰¹

Table 5.3 C₂H₄: Atomic distances (Å) and angles (°) for the different molecular loadings in the MOF. Calculated values for the molecule in the gas phase are 1.0843 Å (CH), 1.3262 Å (CC), 116.426° (<HCH), and 121.787° (<HCC). Symbols for atoms with respect to the MOF are described in the text.

Geometrical Feature	Loading		
	1:1	1:2	1:6
C1-H1	1.0828	1.0832	1.0836
C1-H1'	1.0831	1.0832	1.0833
C2-H2	1.0825	1.0830	1.0832
C2-H2'	1.0825	1.0827	1.0827
C1-C2	1.3283	1.3287	1.3288
∠H1-C1-H1'	116.482	116.515	116.560
∠H2-C2-H2'	116.763	116.669	116.787
∠H1-C1-C2	121.754	121.773	121.684
∠H2-C2-C1	121.733	121.663	121.701
∠H1'-C1-C2	121.760	121.710	121.755
∠H2'-C2-C1	121.500	121.663	121.503
C1-Mg	2.9484	2.9603	2.9265
C2-Mg	3.0731	3.0759	3.1211
∠O-Mg-C1	167.300	167.626	164.706
∠O-Mg-C2	159.139	159.984	159.067

Table 5.4 Intramolecular atomic distances (Å) for C₂H₆ the different molecular loadings in the MOF. Corresponding intramolecular angles are reported in Table 6. Calculated values for the molecule in the gas phase are 1.0928 Å (CH), and 1.5299 Å (CC). Symbols for atoms with respect to the MOF are described in the text. Arrangement of the molecules with respect to the MOF is reported in Table 7.

Geometrical Feature	Loading		
	1:1	1:2	1:6
C1-H1'	1.0944	1.0953	1.0953
C1-H1''	1.0926	1.0926	1.0928
C1-H1'''	1.0913	1.0919	1.0917
C2-H2'	1.0916	1.0908	1.0909
C2-H2''	1.0921	1.0918	1.0923
C2-H2'''	1.0922	1.0923	1.0918
C1-C2	1.5296	1.5285	1.5285

A detailed discussion and analysis of the effect that Born effective charges have on bond dipoles, molecular effective dipoles, and electro-optical parameters for several molecules adsorbed in different MOFs, together with a comparison with values obtained for formal charges and considerations on the role that various computational parameters and the

chemical environment provided by the framework play in the determination of IR intensities is currently under investigation and it will be reported in future publications.¹⁴⁴ Regardless, preliminary results confirm that data and conclusions drawn for the molecular species reported in this work are accurate and allow for the interpretation of experimental IR spectra.

5.3 Geometrical Features for Molecules in the Gas Phase and Framework

5.3.1 CH₄ – Methane

Calculated geometries for methane in the gas phase (CH bond distances of 1.0899 Å, and a HCH angle of 109.471°) and their agreement with experiments (1.087 Å¹⁴⁵, and 109.471°¹⁴⁶, respectively) provide a good ground for comparison of geometrical changes experienced by the molecule(s) when adsorbed in the MOF. When methane is in the framework and molecular symmetry is lost, the molecules are allowed to adapt to the chemical environment provided by the MOF. In order to provide the most precise possible description of the geometrical changes, it is convenient to describe the convention adopted to identify the CH bonds and the HCH angles in methane when in the MOF (Figure 5.1a and Table 4.1). With the central carbon atom sitting right on top Mg at about 3.0076 Å across the loadings, the C-H1 bond can be identified in a unique way as the bond pointing toward the carboxylate group of the organic ligand while the C-H2 and C-H3 bonds are oriented towards the carbonyl groups, and the C-H4 bond is directed toward the center of the MOF void cavity.

Overall, bond distances are only minimally affected by the presence of the framework, with the largest changes with respect to the gas phase being observed for the 1:6 loading case. Although, at first sight, this may seem counterintuitive, such a tendency can be justified by the action that the lateral interaction has on the medium and high molecular loading. For low loading scenario, the C-H2 and C-H3 bonds seem to be particularly affected, indicating a stronger long-range interaction of the molecule with respect to the carbonyl groups of the organic *linkers* which lay at an average distance of 2.8689 Å from the oxygen in the groups.

The C-H4 distances in all the three cases are barely affected; this is consistent with the fact that H4 are the hydrogens oriented toward the MOF void cavity. The discussed changes in the molecular geometries are well reflected by changes in the HCH angles which show an increase of almost 1.000° in the H1-C-H2 and H1-C-H3 angles counterbalanced by a decrease of the same amount in the other three angles involving the H4 atom.

Table 5.5 Intramolecular angles (°) for C₂H₆ the different molecular loadings in the MOF. Corresponding intramolecular distances are reported in Table 5. Calculated values for the molecule in the gas phase are 107.469° (<HCH), and 111.406° (<HCC). Symbols atoms with respect to the MOF are described in the text. Arrangement of the molecules with respect to the MOF is reported in Table 7.

Geometrical Feature	Loading		
	1:1	1:2	1:6
∠H1'-C1-H1''	109.104	109.955	110.030
∠H1'-C1-H1'''	108.053	106.268	106.334
∠H1''-C1-H1'''	107.983	106.390	106.470
∠H2'-C2-H2''	107.938	107.455	107.888
∠H2'-C2-H2'''	107.652	107.858	107.462
∠H2''-C2-H2'''	107.784	107.880	107.832
∠H1'-C1-C2	110.004	111.093	110.951
∠H1''-C1-C2	109.800	110.866	110.797
∠H1'''-C1-C2	111.826	112.066	112.072
∠H2'-C1-C2	110.842	111.273	111.282
∠H2''-C1-C2	111.322	111.078	111.116
∠H2'''-C1-C2	111.144	111.129	111.092

As a general trend, the O1-Mg-C angle (with O1 being the apical off-plane oxygen coordinating Mg) is observed to be close to 169.000° in all cases while the single methane of the 1:6 situation is consistently further in the cavity than those in the other two cases, as indicated by the atomic distances of the closest Mg neighbors (*i.e.*, C, H1, H2, and H3).

5.3.2 C₂H₂ – Acetylene

Calculated bond lengths of 1.0633 Å (CH) and 1.1981 Å (CC) for acetylene in the gas phase are in good agreement with experimental evidence (CH = 1.063 Å, and CC = 1.203 Å)¹⁴⁷ together with the angular arrangement which, as expected, is fully planar (HCC angle of 180.000°)¹⁴⁸. The convention adopted to describe the arrangement of the molecule and its geometrical changes when adsorbed in the MOF is to refer to H1 as the atom closer to the carboxylate group of the organic ligand, and to H2 as the atom pointing toward the carbonyl group in the opposite direction (Figure 5.1b and Table 5.2).

As such, H1 is the closest hydrogen atom to Mg (3.1820 Å), with H2 positioned as far as 3.4604 Å. For all cases, both chemical bonds and angles are experiencing comparable changes with the latter showing acetylene's tendency of breaking its original linear geometrical arrangement with average values for the H1-C1-C2 and C1-C2-H2 angles across the loadings equal to 179.304° and 178.658°, respectively.

Table 5.6 Arrangement (distances (Å) and angles (°)) for the different loadings of C₂H₆ with respect to the MOF. Intramolecular atomic distances and angles are reported in Tables 5 and 6. Symbols for atoms with respect to the MOF are described in the text.

Geometrical Feature	Loading		
	1:1	1:2	1:6
Mg-C1	3.0738	3.1302	3.1254
Mg-C2	4.5330	4.1184	4.1588
Mg-H1'	2.717	2.6441	2.6298
Mg-H1''	2.7169	2.6873	2.6852
Mg-H1'''	3.2525	3.8941	3.8566
Mg-H2'	4.7828	3.8879	3.9632
Mg-H2''	5.1281	4.8313	4.8602
Mg-H2'''	5.1384	4.8332	4.8755
∠O-Mg-C1	167.669	164.012	164.388
∠O-Mg-C2	170.595	177.035	177.145

This aspect, together with the elongations observed in the C1-C2 bond, can be expected to be related to changes in the electron density of the triple bond of acetylene, acting as an *electron donor* with respect to the *electron acceptor* nature of the open metal site. The asymmetric arrangement of the molecule with respect to Mg is indicated by the O-Mg-C1 and O-Mg-C2 angles (around 155° and 173°, respectively) and it can be explained by observing that, in spite of being a symmetric molecule, acetylene overall significant length (around 3.3269 Å) allows for each of its *halves* to interact differently with the chemical environment provided by the MOF and, in particular, by the organic part of the framework. This aspect, together with the softening of the triple bond, provides an additional explanation for the tendency of the molecule to break its linear arrangement. It is interesting to note how the geometry of the single acetylene molecule in the low loading scenario is

the least affected by the presence of the MOF, although laying closer to the open metal site. This effect can be related to the absence of lateral repulsive interaction between molecules.

5.3.3 C₂H₄ – Ethylene

Calculated CC double bond and CH bond lengths for ethylene in the gas phase (1.3262 Å and 1.0843 Å, respectively) are slightly overestimated with respect to experimental values (1.339 Å and 1.086 Å, respectively). While for the HCC angle the same observation applies (121.787° against 121.2°), the HCH angle appears to be underestimated by more than 1.000°¹⁴⁸. Such differences can be explained as arising from the adopted basis set which is not necessarily tailored to describe the gas phase, given its lack of very diffuse functions. The convention on the atoms for ethylene in the MOF are as follows (Figure 5.1c and Table 5.3): C1 is identified as the carbon pointing toward the carboxylate group and bonded to H1 and H1' which are the closest and the farthest hydrogen atom with respect to the open metal site; C2 is therefore identified as the carbon atom pointing towards the carbonyl part of the organic ligand and bonded to H2 and H2' which follow the same description of the other two hydrogen atoms.

The C1-C2 distances of ethylene in the MOF consistently increase in all the three molecular loadings. As observed for acetylene, this trend is a confirmation of the expected loss of electron density experienced by the CC π -bond induced by the positive charge density of the exposed metal cation. In all the three loadings, the CH σ -bonds consistently decrease with the 1:1 loading showing the largest deviation from the gas phase situation. This behavior can be ascribed, once again, to the presence of neighboring molecules which further modify the overall chemical environment each of the six molecules is subjected to. In fact, two hydrogen atoms belonging to two adjacent ethylene molecules lay as close as 2.5416 Å; such a distance is well within the long-range repulsion regime which can be therefore expected to influence not only the binding energy of the molecules (as described in previous works)^{113, 132} but also their structural adaptation and modification to the repulsive potential exerted from one onto the other. An additional confirmation for this

explanation arises from the trend observed in the 1:2 and 1:6 loading scenarios, whose geometries get to be closer to that of the molecule in the gas phase.

In addition, the tendency of the molecules to repel each other is further reflected by the Mg-C1 distances which decrease from 2.9484 Å (1:1) to 2.9265 Å (1:6), and by the Mg-C2 distances which increase from 3.0731 Å (1:1) to 3.1211 Å (1:6). These opposite trends induce on the molecule a pseudo-rotational (*i.e.*, twisting) arrangement reflected by the O-Mg-C1 and O-Mg-C2 angles. Among them, it is particularly interesting to note a difference as wide as 2.5° in the O-Mg-C1 angle between the high and low loading.

5.3.4 C₂H₆ – Ethane

Although on average slightly underestimated, calculated atomic distances and angles for ethane are, overall, in good agreement with experiments¹⁴⁸. Given the geometry of the molecule and its arrangement with respect to the MOF adsorption site, the following convention for the atoms is adopted (Figure 5.1b and Table 5.4-6): C1 is chosen as the closest to Mg carbon atom, and C2 the farthest. The hydrogen atoms bonded to C1 are identified as: H1' (the closest to Mg), H1'' (located at an intermediate distance from Mg), and H1''' (the farthest away from Mg). The same nomenclature is defined for C2 and its H2 hydrogens.

It is convenient to lead the discussion for ethane starting from its angular arrangement with respect to the framework. In the 1:1 scenario, the difference between the O-Mg-C1 and O-Mg-C2 angles is only 3°, allowing the binding interaction to occur only with the (C1H1)₃ group. This is reflected by the almost unchanged C1-C2 bond and by the small differences observed in the (C2H2)₃ group with the farthest of the hydrogens (H2''') being the least effected.

Table 5.7 Calculated (raw data), scaled (0.965), experimental vibrational modes, and difference in frequency between for the last two values for C₁-C₂ molecules. All results for frequencies are reported in cm⁻¹. The last two columns indicate the percent difference between *scaled and experimental and the corresponding absolute average of such difference*.

Molecule	Assignment Description	Calc.	Calc. Scaled	Exp. ¹⁴⁸	$\Delta\nu$	% diff.	Abs. Average % difference
CH ₄	ν_4 (F ₂) CH bending	1341.8	1294.9	1306.2	-11.3	-0.87	0.59
	ν_3 (F ₂) CH asym. stretching	3139.6	3029.7	3020.3	+9.4	+0.31	
C ₂ H ₂	ν_5 (E _u) CH bending	764.7	737.9	730.0	+7.9	+1.08	0.63
	ν_3 (A _{2u}) CH asym. stretching	3402.4	3283.3	3289.0	-5.7	-0.17	
C ₂ H ₄	ν_{10} (B _{2u}) CH ₂ rocking	836.3	807.0	826.0	-19.0	-2.30	0.94
	ν_7 (B _{1u}) CH ₂ wagging	978.7	944.4	949.3	-4.9	-0.51	
	ν_{12} (B _{3u}) CH ₂ scissoring	1478.3	1426.5	1443.5	-17.0	-1.18	
	ν_{11} (B _{3u}) CH sym. stretching	3118.9	3009.7	2988.7	+21.0	0.70	
	ν_9 (B _{2u}) CH asym. stretching	3217.5	3104.9	3105.5	-0.6	-0.02	
C ₂ H ₆	ν_9 (E _u) CH bending	832.0	802.9	821.5	-18.6	-2.26	1.08
	ν_6 (A _{2u}) CH ₃ deformation	1415.5	1365.9	1379.2	-13.3	-0.96	
	ν_8 (E _u) CH ₃ deformation	1505.3	1452.7	1472.2	-19.5	-1.32	
	ν_5 (A _{2u}) CH ₃ asym. stretching	3034.4	2928.2	2954.0	-25.8	-0.87	
	ν_7 (E _u) CH asym. stretching	3104.5	2995.8	2995.5	+0.3	+0.01	

The redistribution of charge in the (C1H1)₃ group due to the metal site, is accompanied by significant changes in the H1'-C1-H1'' and H1'-C1-H1''' angles which, not surprisingly, involve the closest neighbor atom to Mg (H1'). Such angular modifications are as wide as 1.6° for the former angle, and as small as 0.6° for the latter one. Similar comments apply to the H1'-C1-C2 and H1''-C1-C2 angles, which are now observed to decrease by 1.4° and 1.6°, respectively.

For the 1:2 and 1:6 loadings, the molecular orientation with respect to the Mg-O axis is what determine the dramatic changes in geometrical features of the adsorbates. This is

related to the reduction/absence of first neighbor ethane molecules, which induce a drastic reduction in repulsive long-range interactions and translate into the molecules' tendency to lay into a nearly parallel fashion with respect to the framework, with the O-Mg-C2 angle as large as 177°. The additional long-range interaction that the overall molecule is now subjected to, is not anymore localized only onto the (C1H1)₃ group but, instead, induces significant structural changes in the molecule as a whole. These changes can be appreciated both in terms of bond lengths and angles. Among these, the most dramatic changes are related to a decrease in the C1-C2 bond and in increases in both the C1-H1' and C1-H1''' bonds. Repulsive interactions seem to act on the (C2H2)₃. In reference to angles, it is interesting to note how the significant increase of 2.5° in the H1'-C1-H1'' angle is counterbalanced by a decrease of more than 1° in both the H1'-C1-H1''' and H1''-C1-H1''' angles to minimize the overlap between the hydrogen *s*-orbitals. These aspects are further reflected by increases in the H1'''-C1-C2 angle close to 1.5°. Overall, the new geometrical arrangement of the molecules is dramatically reflected by changes in atomic distances between the atoms in the molecules and the Mg open metal site, with changes spanning from 0.1 Å up to almost 1.0 Å.

5.4 Infrared Spectra for Molecules in the Gas Phase and in the Framework

For each of the following subsections, we first briefly discuss the IR vibrational spectra for the gas phase, and then describe observed changes in the bands structural features and frequency shifts for the molecules when adsorbed in the MOF. Note that intensities reported in Figure 5.2-4 were scaled with respect to the highest value calculated for the molecules in the MOF. Spectra are reported for the gas phase (black curves), low (green), medium (blue), and high (red) loadings. Reference to band positions refers to the calculated values which, therefore, should be scaled (multiplied by 0.965) when compared to experimental evidence.

Table 5.8 Calculated (raw data) and scaled (0.965) vibrational modes for the different molecular loadings in the MOF for C₁-C₂ molecules. Frequency shifts with respect to the gas phase are also listed. All results are reported in cm⁻¹.

Molecule	Assignment & description as in the gas phase	Frequencies w.r.t different loadings						Freq. Shifts		
		Calculated			Calculated - Scaled			$\Delta\nu$		
		1:1	1:2	1:6	1:1	1:2	1:6	1:1	1:2	1:6
CH ₄	ν_4 (F ₂) CH bending	1352.0	1353.0	1353.0	1304.7	1306.6	1305.6	+6.5	+7.4	+7.4
	ν_3 (F ₂) CH asym. stretching	3131.5	3134.0	3132.0	3021.9	3031.7	3022.4	-7.8	-5.4	-7.3
C ₂ H ₂	ν_5 (E _u) CH bending	768.0	773.0	768.0	741.1	746.0	741.1	+3.2	+8.0	+3.2
	ν_3 (A _{2u}) CH asym. stretching	3403.0	3402.0	3405.0	3283.9	3282.9	3285.8	+0.6	-0.4	+2.5
C ₂ H ₄	ν_{10} (B _{1u}) CH ₂ rocking	833.0	838.2	837.5	803.7	808.9	808.2	-3.3	+1.9	+1.2
	ν_7 (B _{1u}) CH ₂ wagging	1006.0	1008.0	1014.0	970.8	972.7	978.5	+26.3	+28.3	+34.1
	ν_{12} (B _{3u}) CH ₂ scissoring	1481.0	1480.0	1478.0	1429.2	1428.2	1426.2	+2.6	+1.7	-0.3
	ν_{11} (B _{3u}) CH sym. stretching	3156.0	3135.0	3140.0	3045.5	3025.3	3030.1	+35.9	+15.6	+20.4
	ν_9 (B _{2u}) asym. stretching	3261.0	3248.0	3242.0	3146.9	3134.3	3128.5	+42.0	+29.4	+23.6
C ₂ H ₆	ν_9 (E _u) CH bending	845.0	831.8	832.9	815.4	802.7	803.7	12.6	-0.1	-0.1
	ν_6 (A _{2u}) CH ₃ deformation	1434.6	1407.8	1408.3	1384.4	1358.5	1359.0	18.4	-7.4	-7.4
	ν_8 (E _u) CH ₃ deformation	1505.4	1503.4	1505.6	1452.6	1450.8	1452.9	-0.1	-1.9	-1.9
	ν_5 (A _{2u}) CH ₃ asym. stretching	3033.0	3035.7	3007.7	2926.9	2929.4	2902.4	-1.3	1.3	1.3
	ν_7 (E _u) CH asym. stretching	3100.0	3100.8	3104.9	2991.5	2992.3	2996.2	-4.3	-3.5	-3.5

5.4.1 CH₄ – Methane

Methane is the molecule presenting the highest symmetry among those discussed in this work (point symmetry group T_d). It is characterized by 9 vibrational modes corresponding to four normal modes classified as

$$\Gamma_v = A^R + E^R + 2F_2^{IR}$$

indicating that only the two 3-fold degenerate F₂ modes are IR active. Table 5.7 lists the calculated IR modes, together with their scaled values, and the experimental peak position for methane in the gas phase. Also indicated, are the differences observed between the calculated scaled peaks and experimental observations together with the percent difference

and the absolute average of such difference. Results are in very good agreement with experiment with an average absolute difference of 10 cm^{-1} . Agreement is also confirmed with respect to the intensities, showing that both the CH bending, and the CH asymmetric stretching modes appear as very strong bands.

Results for calculated frequencies of methane when adsorbed in the MOF with respect to the three molecular loadings are reported in Table 9. Figures 5.2a-2b show the region of the IR spectrum characterized by the presence of active modes. When in the MOF, the CH_4 CH bending mode blue-shifts by 10 cm^{-1} (1353.0 cm^{-1}) and generates a strong band referring to the double-degenerate E_u mode and the single-degenerate A_u mode. In addition, the appearance of a medium intense shoulder is observed around 1370 cm^{-1} associated to the single-degenerate A_u mode combined with the double-degenerate E_u mode. For the CH asymmetric stretching mode, no significant frequency shifts are observed, although the strong three-fold F_2 mode present in the gas phase appears far less intense in the medium

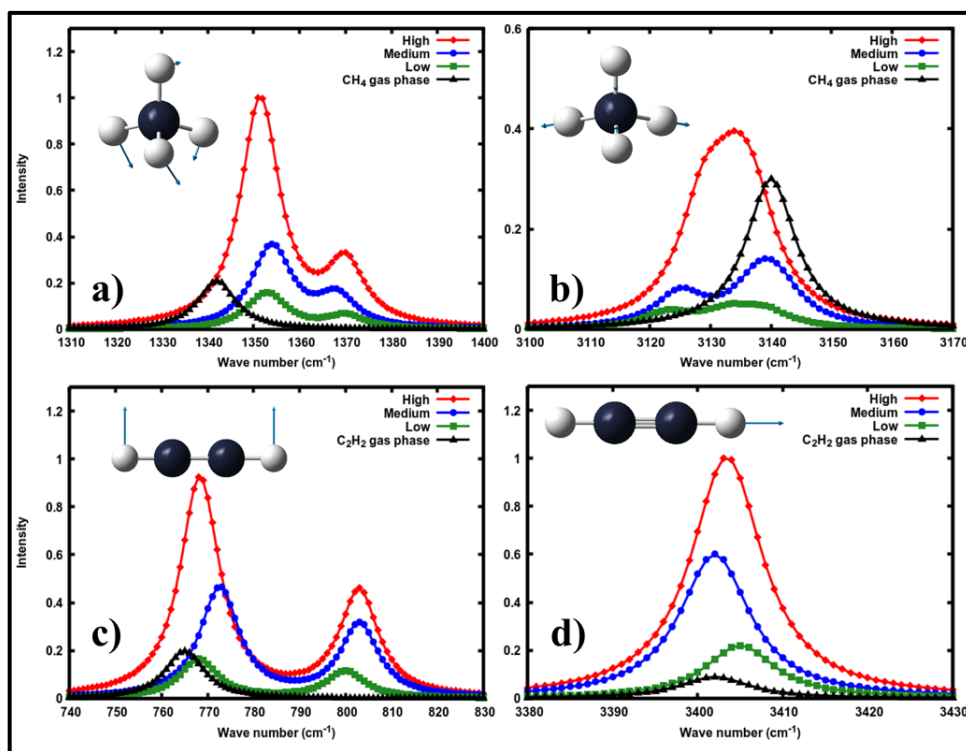


Figure 5.2 IR spectra: (a) CH_4 in the range $1310\text{--}1400\text{ cm}^{-1}$; (b) CH_4 in the range $3100\text{--}3170\text{ cm}^{-1}$; (c) C_2H_2 in the range $740\text{--}830\text{ cm}^{-1}$; (d) C_2H_2 in the range $3380\text{--}3430\text{ cm}^{-1}$.

(roughly half), and low loading (very broad band) while it is more intense in the high loading case, due to the presence of six molecules. In addition, while two bands are observed in the medium and low loading cases, only one broad band is present in the 1:1 scenario. In particular, this includes two different modes (3133 cm⁻¹ and 3137 cm⁻¹) of E_u (double-degenerate) and A_u (single-degenerate) symmetry, respectively. This feature can be related to the symmetric nature of the molecular arrangement portrayed by the 1:1 loading situation. The 1:2 loading shows two medium bands separated by roughly 14 cm⁻¹; a first broader one showing the presence of two modes (3141 cm⁻¹ double-degenerate E modes, and 3137 cm⁻¹ single-degenerate A mode), and a second centered around 3125 cm⁻¹ including a double-degenerate E and a single-degenerate A mode. The low loading, where no symmetry is involved, shows a very broad band spanning from the single-degenerate modes located at 3132 cm⁻¹ to 3139 cm⁻¹, and one of lower intensity around 3123 cm⁻¹. Although characterized by a very weak intensity, it is worth reporting that a new band appears in the spectrum corresponding to a scissoring CH vibrational mode (1580 cm⁻¹ in both the medium and low loadings); such a peak also shows a very weak shoulder at 1572 cm⁻¹ which, given its scissoring motion, indicate the degeneracy nature of the mode itself. Similar features are observed for the high loading scenario, for which as expected, the intensity is one-third lower.

5.4.2 C₂H₂ – Acetylene

Acetylene has a linear symmetric structure and belongs to the point symmetry group $D_{\infty d}$. It is characterized by seven vibrational modes corresponding to five normal modes classified as

$$\Gamma_v = E_g^R + E_u^{IR} + 2A_{Ig}^R + A_{2u}^{IR}$$

indicating that only the one 2-fold degenerate E_u and the one single-fold degenerate A_{2u} modes are IR active. Table 5.7 lists the calculated IR modes, together with their scaled values, and the experimental peak position for acetylene in the gas phase. Also indicated, are the differences observed between the calculated scaled peaks and experimental

observations together with the percent difference and the absolute average of such difference. Results are in very good agreement with experiment with an average absolute difference as small as 6.8 cm^{-1} . Agreement is also confirmed with respect to the intensities, showing the very strong band associated with the CH bending located at 737.9 cm^{-1} , and the strong band corresponding to the CH asymmetric stretching calculated at 3283.3 cm^{-1} .

Results for calculated frequencies of acetylene when adsorbed in the MOF with respect to the three molecular loadings are reported in Table 5.8. Figure 5.2c-2d shows the region of the IR spectrum characterized by the presence of active modes. The two-fold degenerate E_u bending mode observed in the gas phase for C_2H_2 (764 cm^{-1}), splits into two strong bands. While the most intense of the two remains roughly at the same position, the second one is blue-shifted by as much as 34 cm^{-1} . The most intense peak is actually formed by a two-degenerate E_u mode (768 cm^{-1}) and a single-degenerate mode (770 cm^{-1}) which, appears to be shadowed by the most intense of the bands. For this reason, the latter does not appear as a shoulder, but it is instead obscured by the E_u mode mentioned above. The intensity of the peak for the medium and low loading cases are still very strong, although reduced in intensity, as expected. For the 1:2 case, the peak blue-shifts by almost 10 cm^{-1} with respect to the corresponding mode in the gas phase, making the peak potentially determinable experimentally. This description is not applicable to the 1:1 loading scenario, for which the position of the peak is basically unchanged with respect to the gas phase. The most interesting feature showed by the modes associated with the C_2H_2 bending modes, is provided by the appearance of a medium-strong peak around 800 cm^{-1} ; with distances between the carbon in acetylene and the Mg open metal site of 2.887 \AA and 2.991 \AA , this is a proper vibrational mode due to the long-range interaction occurring between the molecule and the open metal site. Consistency in the intensity of this peak for the three different loadings is observed with the presence of the 1:1 peak at 802 cm^{-1} (E_u), the 1:2 at 802 cm^{-1} (E), and the 1:6 slightly red-shifted at 800 cm^{-1} .

In the case of the asymmetric stretching mode, all the three loadings show bands red-shifted by roughly 8 cm^{-1} with respect to the gas phase, with the most dramatic difference being

observed for the intensities. In fact, the interaction of acetylene with the framework, translates into very strong peaks for the 1:1 case referring to the two-fold degenerate E_u mode at 3403 cm^{-1} and the single-degenerate A_u mode appearing as a shoulder. These observations are well supported by the discussion about the importance of acknowledging the interaction of acetylene not only with the metal site but with part of the organic part of the framework as well. In the 1:2 case, the most intense band is the two-degenerate E mode at 3402 cm^{-1} which shows a shoulder at 3401 cm^{-1} corresponding to the single-degenerate A mode. In the 1:6 scenario, the single-degenerate mode is located at 3404 cm^{-1} . We make the hypothesis that the splitting of the degeneracy in the medium and high loading scenarios are related to the in-phase and out-of-phase interactions (*i.e.*, relative vibrations) of the C_2H_2 molecules loaded in the framework. In addition, the distance between the two closest hydrogen atoms belonging to two different C_2H_2 molecules in the full loading case, is as small as 3.589 \AA , likely indicating the effect of long-range interactions.

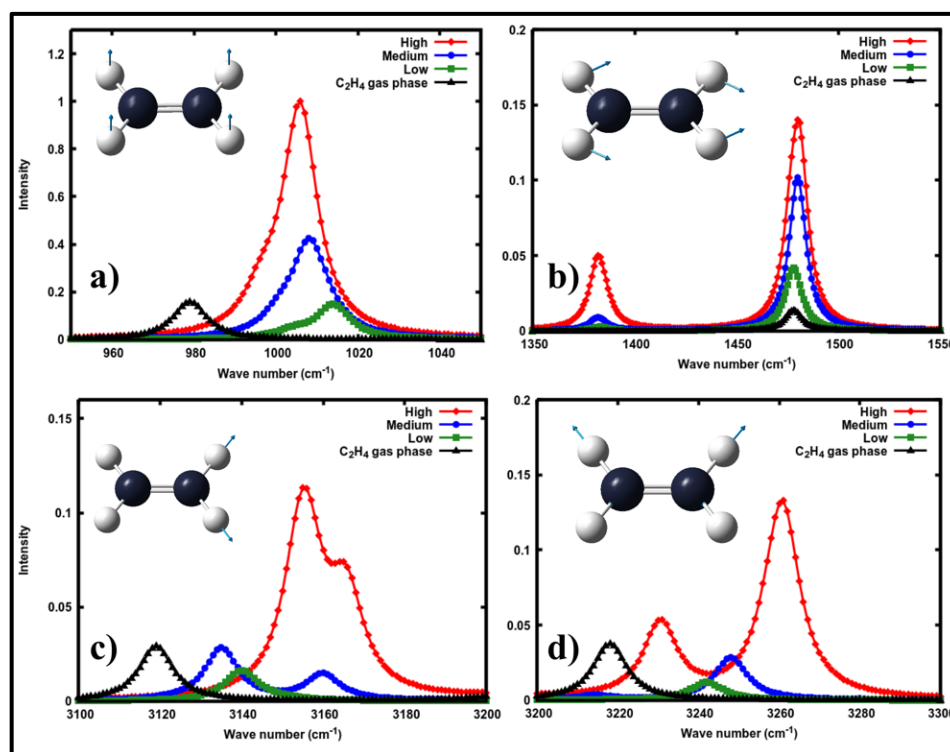


Figure 5.3 IR spectra for C_2H_4 : (a) 950-1450 cm^{-1} range; (b) 1350-1550 cm^{-1} range; (c) 3100-3200 cm^{-1} range; (d) 3200-3300 cm^{-1} range.

5.4.3 C₂H₄ – Ethylene

Ethylene's planar structure belongs to the point symmetry group D_{2h} . Ethylene is characterized by twelve vibrational modes classified as

$$\Gamma_v = 2B_{2u}^{IR} + 2B_{1g}^R + 3A_g^R + 2B_{3u}^{IR} + A_u^{silent} + B_{1u}^{IR}$$

indicating that five modes are IR active. These are: the two 2-fold degenerate B_{2u} , the two 2-fold degenerate B_{3u} , and the one single-degenerate B_{1u} modes. Table 5.7 lists the calculated IR modes, together with their scaled values, and the experimental band position for acetylene in the gas phase. Also indicated, are the differences observed between the calculated scaled bands and experimental observations together with the percent difference and the absolute average of such difference. Results are in very good agreement with experiment with an average absolute difference of only 12.5 cm⁻¹. Agreement is also confirmed with respect to the intensities which show three very strong peaks corresponding to: (i) The B_{1u} CH₂ wagging mode at 907.0 cm⁻¹; (ii) The B_{3u} CH symmetric stretching mode at 3009.7 cm⁻¹; and, (iii) The B_{2u} asymmetric stretching mode at 3104.9 cm⁻¹. The remaining two modes are the medium intense B_{3u} CH₂ scissoring at 1426.5 cm⁻¹, and the very weak (almost to the limit of being silent) B_{2u} CH₂ rocking mode at 807.0 cm⁻¹.

It is interesting to note that this latter mode seems to be affected by a dramatic uncertainty at experimental level. In fact, Herzberg¹⁴⁸ refers to the ν_{10} B_{2u} as a medium intense band located at 995 cm⁻¹ which he identifies as a band “badly” overlapping with the much stronger band at 942.2 cm⁻¹. As such, he admits that it is “not very accurately measured”. Somehow similarly, he also refers to the ν_4 A_u mode located at 825 cm⁻¹ as one of four modes “much less definitely identified”. He discusses it as not being active neither in the Raman and in the infrared spectrum, with the only chance of identifying it as a combination of band with respect to a weak Raman line at 1656 cm⁻¹ that can therefore be seen as a $2\nu_4$ mode, as suggested by Wu¹⁴⁹. This interpretation is supported by the concept of Fermi resonance. Note that in Table 5.7, we report the value of 826 cm⁻¹, labelled as ν_{10} (B_{2u}) by Sverdlov¹⁴⁶ but labelled by NIST¹⁵⁰ as ν_9 (B_{2u}) as per Ref¹⁵¹.

Results for calculated frequencies of ethylene when adsorbed in the MOF with respect to the three molecular loadings are reported in Table 5.8. Figure 5.3 shows the region of the IR spectrum characterized by the presence of active modes. For the lowest IR active mode in C_2H_4 (CH_2 rocking) lying at 836 cm^{-1} in the gas phase, no significant appreciable shifts are observed when the molecules are loaded in the MOF ($\pm 2\text{ cm}^{-1}$). The most intense mode in the gas phase (979 cm^{-1} $-CH_2$ wagging) translates into the highest intense mode in the MOF. For the low loading case, while the band is as intense as in the gas, it is now blue-shifted by as much as 34 cm^{-1} . As expected, for the medium and high loadings, the intensity triplicate and it is six-times more intense, respectively, making the band very strong. For these two cases, the bands are less blue-shifted, by around 27 cm^{-1} . For all the loadings, shoulders at frequencies smaller by roughly $5\text{-}10\text{ cm}^{-1}$ appear. The CH_2 scissoring mode at 1478 cm^{-1} is fully reproduced when ethylene is present in the MOF; such an observation is independent from the loading. Interestingly, though, a very weak band appears in all cases at 1382 cm^{-1} , although given its low intensity it may not be appreciable experimentally. Visual inspection (via graphical animations) ¹⁵², reveals this mode to correspond to the asymmetric CH_2 scissoring motion. The CH symmetric stretching modes (B_{2u} , at 3118 cm^{-1}) and the asymmetric modes at 3217 cm^{-1} , are both very weak with a maximum intensity ten-fold smaller than the most intense peak located at 979 cm^{-1} . In the low loading case, the single bands are blue-shifted by $20\text{-}23\text{ cm}^{-1}$. When more molecules are present in the framework, new bands appear indicating the strength of the interaction between the molecules. This observation is consistent with the values reported in Table 4.6-7 ^{113, 132} for the lateral interaction experienced by the molecules in the MOF. The asymmetric stretching mode is particularly interesting when its features are compared between the 1:2 and 1:1 loadings. In fact, for the former two distinct, although very weak bands (when compared to the intensities observed in the gas phase) are observed at 3134 cm^{-1} and 3160 cm^{-1} ; for the latter, the two peaks separated by 10 cm^{-1} translating into the appearance of a shoulder into the main band located at 3156 cm^{-1} . Somehow similar comments apply to the asymmetric CH_2 stretching mode with the largest shift appearing for the 1:1 loading (42

cm⁻¹), in addition to a very weak new peak appearing at 3231 cm⁻¹, still referring to the asymmetric CH stretching mode.

5.4.4 C₂H₆ – Ethane

Ethane has a three-fold axis along the CC σ-bond and, in its most stable staggered structure (point symmetry group D_{3d} #32), a center of symmetry with the two CH₃ groups rotated by 60° with respect to each other. Ethane is characterized by 18 vibrational modes classified as

$$\Gamma_v = 3E_u^{IR} + 3E_g^R + 2A_{2u}^{IR} + 3A_{1g}^R + A_{1u}^{silent}$$

indicating that the three 2-fold degenerate E_u and the one single-fold degenerate A_{2u} modes are IR active. Table 5.7 lists the calculated IR modes, together with their scaled values, and the experimental peak position for ethane in the gas phase. Also indicated, are the differences observed between the calculated scaled peaks and experimental observations together with the percent difference and the absolute average of such difference. Results are in very good agreement with experiment with an average absolute difference equal to 15.5 cm⁻¹. Once again, agreement is also confirmed with respect to the intensities, showing

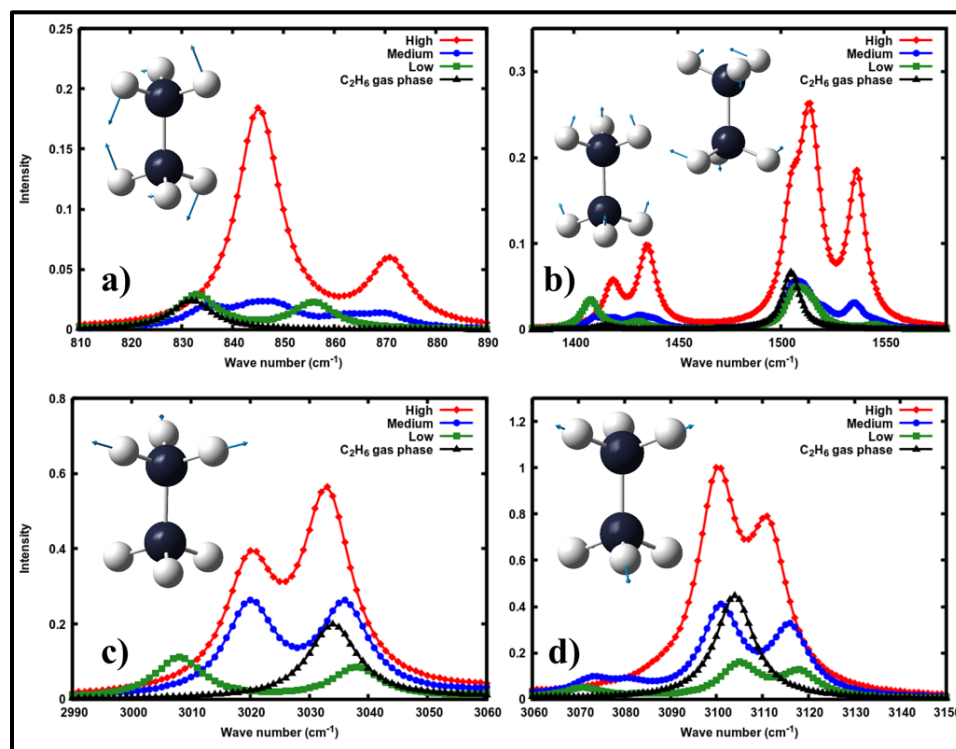


Figure 5.4 IR spectra for C_2H_6 : (a) 810-890 cm^{-1} range; (b) 1350-1600 cm^{-1} range; (c) 2990-3060 cm^{-1} range; (d) 3060-3150 cm^{-1} range.

the two strongest bands associated with the two ν_7 (E_u) and ν_5 (A_{2u}) CH asymmetric stretching modes located at 2995.8 cm^{-1} and 2928.2 cm^{-1} , respectively. The third most intense band is at intermediate frequencies (1452.7 cm^{-1}) and refers to a ν_8 (E_u) CH_3 degenerate deformation. Finally, the last two bands characterized by weaker bands are located at 1365.9 cm^{-1} and 802.9 cm^{-1} and refer to a CH_3 deformation mode and the CH bending mode, respectively. It is interesting to note that the mode reported by Sverdlov at 1472.2 cm^{-1} ¹⁴⁶, is reported by Herzberg at 1486 cm^{-1} ¹⁴⁸, indicating as already for ethylene, a good degree of uncertainty at experimental level.

Results for calculated frequencies of ethane when adsorbed in the MOF with respect to the three molecular loadings are reported in Table 5.8. Figure 5.3 shows the region of the IR spectrum characterized by the presence of active modes.

In the lowest frequency region, the E_u double-degenerate CH_3 rocking mode observed in the gas phase, splits into two individual bands in all the considered molecular loadings,

corresponding to two individual rocking modes for the two CH₃ groups. A visual inspection of the modes, reveals that the symmetric CH₃ rocking mode is drastically blue-shifted by 40 cm⁻¹ in the 1:1 case, and by roughly 25 cm⁻¹ in both the 1:2 and 1:6 cases. It is also interesting to observe that no change in intensity is recorded between the high and the medium loadings.

The most intense band referring to the CH₃ deformed rocking, seems to be a new band arising from the interaction of the molecule with the MOF open metal site. Different loadings, in this case, show not only different intensities (as expected) but also different band locations, with the high loading case blue-shifted by 13 cm⁻¹, and the other two cases not showing any appreciable shift. In the 1400-1600 cm⁻¹ region, two peaks are present in the gas phase as discussed before. The lowest of the two modes (CH₃ symmetric deformation) in the MOF situation, shows the appearance of two distinct bands in all the considered loadings with, although, different structural features. In fact, for the low and medium loadings, the stronger band is red-shifted with respect to the values reported for the gas phase, by 7 cm⁻¹, while for the high loading a medium intense band is observed as blue-shifted by 3 cm⁻¹ only. In this latter case, the most intense peak appears at 1436 cm⁻¹ (E_g) at difference with the other two loadings for which this mode is extremely weak. Such major differences in intensities will be discussed in ¹⁴⁴ and they can be quantitatively explained with the values obtained for the Born effective charges. Overall, despite the presence of two bands being observed for all the three loadings, an inversion in intensities is recorded between the high case on one hand, and both the low and medium cases on the other hand.

The second band in this region (CH₃ deformation) presents new interesting structural features for the molecules in the framework. The low loading case shows a band broader than the one observed in the gas phase, which then develops into a double-band in the medium loading, to eventually manifest itself as a strong band accompanied by a shoulder in the high loading scenario. Given the width of the band, the feature that develops into the shoulder remains at the same location in the spectrum with respect what observed in the

gas phase, but the main band is blue-shifted by 12 cm^{-1} . The framework gradually allows for a new intense band to appear in the high loading case, located 22 cm^{-1} higher than the same band observed in the gas phase. In the 3000 cm^{-1} regions, characterized by CH stretching modes, the calculated gas phase spectrum shows a medium and a strong band at 3034 cm^{-1} and 3104 cm^{-1} , respectively. The former is the A_u mode referring to the CH_3 symmetric stretching mode, while the latter is the E_u mode corresponding to the CH_3 asymmetric degenerate stretching mode.

When in the MOF, up to six bands appear across the whole $3000\text{-}3120\text{ cm}^{-1}$ range of the spectrum. The two distinct bands appearing in the low loading scenario at 3008 cm^{-1} and 3038 cm^{-1} , get closer to each other (3019 cm^{-1} and 3036 cm^{-1}) in the medium loading where they appear as minor bands of a broader band of the same intensity. Increasing the molecular loading makes for the two bands to differentiate from each other in terms of intensity, with the mode at 3020 cm^{-1} showing one-third less intensity than the peak at 3034 cm^{-1} .

The last band to be discussed is that referring to the gas phase at 3105 cm^{-1} , which develops into four distinct bands when C_2H_6 molecules are in the framework. The low loading case, shows a very weak and broad structure spanning from 3070 cm^{-1} to 3120 cm^{-1} , with the presence of a further broad band characterized by two individual peaks centered at 3105 cm^{-1} and 3118 cm^{-1} . The overall broad band, further develops for the medium loading into a long *tail* as wide as 20 cm^{-1} (from 3070 cm^{-1} to 3090 cm^{-1}) with the highest region of the band structuring into two more well-defined peaks located at 3101 cm^{-1} and 3116 cm^{-1} , respectively. The high loading appears to be characterized by only two major bands (3100 cm^{-1} and 3112 cm^{-1}) sharing a strong wide band spanning from 3070 cm^{-1} to 3130 cm^{-1} which obscures the weak structures described above for the low and medium loading cases. Overall, given the widths of the bands observed in the MOF cases, both blue-shifts and red-shifts are observed with respect to the different loadings; such differences are related to the geometrical changes and corresponding changes in intramolecular charge

redistributions induced both by the presence of the framework and by neighboring molecules.

For these small hydrocarbons (C_1 - C_2), similar study is in progress in MOF-74-Zn periodic structure to see how these molecules behave differently in the same MOF structure but different atoms at the open metal sites in the isostructural MOF-74. As demonstrated, the IR shifts for the C_1 - C_2 molecules over all didn't show significant differences with respect to different molecular loading sizes. This is due to the fact that the intermolecular distances are long for intermolecular interaction to occur. To see how intermolecular interaction of molecules in the MOF affects the IR behavior, one has to consider bigger molecules. To address this bigger hydrocarbon molecules such as propane, propene, butylene, and butane are considered in both Mg and Zn MOF-74 and are under investigation¹⁵³.

5.5 Summary

First-principle density functional theory calculations to study the IR spectra of three different molecular loadings for C_1 - C_2 hydrocarbons in MOF-74-Mg. Results such as band locations, intensities, and frequency shifts across the three 3D models, and with respect to the molecules in the gas phase are presented and described in the context of the chemical environment provided by the MOF. In addition, the effect of molecular lateral interaction between the molecules in the MOF cavity is also discussed. Both aspects provide for a rich ground of discussion which finds its roots into the geometrical arrangements that the molecules assume with respect to each other and with respect to the framework's backbone. While energetics and spectra for methane are only minimally influenced by these aspects, acetylene is found to be highly affected not only by the open metal site but by the ligands' terminations as well. For the larger ethylene and ethane molecules, wide frequency shifts are observed (up to 34 cm^{-1}) together with the gradual appearance of structured bands corresponding to the different molecular loadings. Such dramatic differences are mostly due to the geometrical arrangement of the molecules with respect to the MOF and are related to the significant lateral interaction exerted by the molecules onto each other. In reference to energetics, binding energies are corrected for BSSE, zero-point energy,

thermal correction providing for a direct comparison between calculated results and experimental heats of adsorption.

Overall, it is expected that the features of the described IR spectra can provide useful information for the interpretation of experimental spectroscopic observations which, to the authors' knowledge, is not yet published. With energetics of adsorption previously published by the same authors for C_2H_4 and C_2H_6 , this study provides an overall description of the physical-chemical nature of the interaction of C_1 - C_2 hydrocarbons with the primary binding site of MOF-74-Mg.

6 Results: Diffusion Properties of C₁-C₂ Hydrocarbon Molecules in MOF-74-Mg

6.1 Introduction

The study of the diffusion properties in solids is of broad interest and fundamental importance for the characterization of materials for industrial application such as gas storage, catalysis, and membrane technologies. Despite such importance, experimental researches pertaining to diffusion studies have been extremely challenging and there is a serious lack of reliable experimental mass diffusion statistics.¹⁵⁴ Experimental determination of the diffusion coefficient of hydrogen atoms, for instance, in metallic systems has resulted in undesirable discrepancies and scattered values over many orders of magnitude among results from different research groups.¹⁵⁵⁻¹⁵⁶ The values of such essential quantities for many important systems such as MOFs are rarely reported in the literature. Though MOFs are ideal candidate for a wide range of potential applications which include heterogeneous catalysis, gas sensing, drug delivery, fuel gas storage, and gas molecules separation which require the understanding of diffusion properties,^{51-52, 54, 120, 157} the availability of literature recorded toward their diffusion characterization is quite limited. In their experimental pulsed field gradient (PFG) NMR studies, *Stallmach et al.*, demonstrated superior diffusion properties of organic gas molecules such as methane, ethane, n-hexane and benzene in MOF-5 compared to other porous materials such as zeolites¹⁵⁸⁻¹⁵⁹. However, the scarce experimental diffusion data is confirmed by several research results coming from several computational research groups.

*The material contained in this chapter has been recently submitted to American Physical Society under Physical Review Letters by Gemechis Degaga, Kenneth Flurchick, and Loredana Valenzano.

While *Canepa et al.* reported on the diffusion of H₂, H₂O, CO₂ in MOF-74-Mg¹⁶⁰, diffusion properties the diffusion of Ar, H₂, N₂, H₂O, CO₂, and small organic molecules have been documented for MOF-2, 3, 5, and UiO-66.^{159, 161-163} While on one hand the potential of MOF-74-M toward olefin-paraffin separation has been established, to the author's knowledge, the description of the molecular transport properties of these molecules in most MOFs is still lacking from both experiment and computational research. As demonstrated in previous chapters and other literatures, the selective gas separation capability of a MOF-74-Mg/Zn was addressed and quantified in terms of relative binding energies and(or) heat of adsorption with respect to different molecules, which have been shown to interact with the metal at the open metal sites of several MOF-74-M species with a differential binding energies ranging between 15 to 20 kJ/mol.^{113 132 63, 116} As such, together with the spectroscopy studies presented in chapter 5, this work aims at presenting, for the first time, a comprehensive description of the nature of the binding and diffusion mechanisms of CH₄, C₂H₂, C₂H₄, and C₂H₆ in MOF-74-Mg. Eventually, this work is anticipated to shed some light on the prediction of the diffusion properties of larger hydrocarbons and other nano-porous materials which would otherwise be experimentally challenging.

In most cases, the synthesis of pure MOF structure is compromised due to defects, dislocations, and presence of other foreign molecules which hinder accurate characterization of MOFs for many technological applications. One of the most frequent contaminant is H₂O molecules which inevitably persistently present starting from synthesis process. At the end of this chapter, an effort particularly focused to study the influence of the pre-adsorbed H₂O molecules on diffusion process of small hydrocarbons in the MOF-74-Mg: results for ethane, and ethylene will be presented for their diffusion within a single honeycomb MOF-74-Mg cavity.

6.2 Computational Details

In order to model the molecular diffusion of small hydrocarbons in the MOF, climbing-image elastic band (CI-NEB)¹⁶⁴ method coupled with density functional theory was used

as implemented in the QUANTUM ESPRESSO¹⁶⁵ software package. Following the available literature,¹⁶⁰ in order to account for the long range interaction between the molecules and the framework, the nonlocal functional vdW-DF¹⁶⁶⁻¹⁶⁹ was adopted. Ultra-soft pseudopotentials were used with wave function and density cutoffs of 35 and 420 Ry, respectively. Convergence test shows that Γ -point calculations are sufficient and yield total energies converging within chemical accuracy with respect to denser k-point meshes. Energy differences significant to properly describe diffusion profiles and diffusion barriers converged with less than 1 meV with self-consistency tolerances set to a threshold value of 10^{-6} Ry. Atomic positions were allowed to relax until the total forces on each atom were less than 2.6×10^{-4} eV/Å. The experimentally refined MOF-74-Mg structure was considered for geometry optimization while the lattice parameters were imposed to remain constant, and corresponded to the MOF hexagonal lattice with $a = 25.881$ Å, and $c = 6.879$ Å. The bulk 3D structure of MOF-74-Mg consists of unsaturated helicoidally MgO₅ metal-oxide chains at each hexagonal corner of the longitudinal channels where these chains are connected by the dihydroxyterephthalate (DOT) organic ligand as depicted in Figure 6.1.

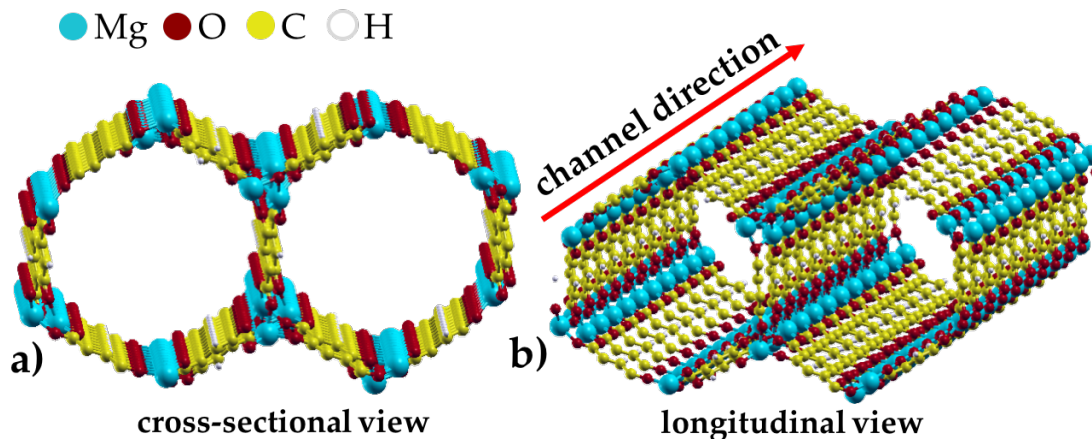


Figure 6.1 Bulk structure of MOF-74-Mg a) cross-sectional view of the channels, and b) depiction showing longitudinal channel direction.

6.3 Results and Discussion

First, the binding energies of CH_4 , C_2H_2 , C_2H_4 , and C_2H_6 were calculated and their molecular spatial arrangement at the open metal adsorption sites in the MOF were studied. This first part of the investigation was necessary to properly set the energetic scenarios which acts as the starting point for the molecular diffusion process. Recent theoretical and experimental works have explored the origin, and the binding nature of the *static* adsorption of several molecules in MOF-74-Mg.^{56, 58-59, 170-171} The computed binding energies (BE) are in an excellent agreement with available experimental and computational literatures, taking into account the zero-point energy and thermal energy corrections which can be up to 0.05 eV for such molecules¹²⁹ presented in Table 1. Figure 6.2 shows the spatial orientation of the molecules at the open metals sites. For C_2H_2 and C_2H_4 the interaction with the open metal center is through the unsaturated carbon-carbon double bond and triple bond respectively, and then the distance between the metal center and the two carbon atoms (Mg-C1, and Mg-C2) are presented. In the case of CH_4 and C_2H_6 , the interaction with the open metal center is through the two closest hydrogen atoms and then the distance between the metal center and the two hydrogen atoms (Mg-H1, and Mg-H2) are reported.

To study the molecular diffusion processes of the small hydrocarbons in the MOF, we considered diffusion mechanisms within the cavity and along the channel direction as shown in Figure 6.1. Diffusion mechanism **M1** is dedicated to the diffusion of the gas molecules within the cavity of the MOF while the diffusion mechanism **M2** is for diffusion along the longitudinal channel direction. For diffusion within the cavity (**M1**), taking the advantage provided by the structural symmetry, there are only three possible diffusion mechanisms to be considered. Diffusion mechanism **M1a** refers to the diffusion of a molecule from an open metal site to the nearest open metal site within the cavity (from Mg1 to Mg2). The consideration of this mechanism is important for two main reasons, (i) it helps in exploring the existence of secondary binding site on the ligand as in the case of CO_2 ^{160, 172} in MOF-74 and (ii) since Mg2 is slightly displaced along the longitudinal

channel direction, it gives a very important insight as to whether it is energetically favorable for a molecule to drift along the channel direction or stay within the cavity when compared to diffusion mechanism *M1b*. It is worth mentioning here that in Figure 6. 3a, the metal atoms Mg1, Mg3, and Mg5 are on the same plane perpendicular to the longitudinal axis parallel to the channel direction while Mg2, Mg4, and Mg6 share the same plane perpendicular to the longitudinal axis parallel to the channel direction slightly displaced (~ 3 Å) further into the channel direction.

Diffusion mechanism *M1b* refers to the diffusion of a molecule from one open metal site to the next nearest open metal site within the cavity (Figure 3a, from Mg1 to Mg3). Diffusion mechanism from one open metal site to the opposite site across the across-section is not important and is not considered (Figure 2a, from Mg1 to Mg4). In diffusion mechanism *M2*, the molecule hops along the longitudinal channel direction from one open metal site to the nearest open metal site along the metal-oxide chain (Figure 6.3b, from Mg1 to Mg2 and so on).

Table 6.1 Comparison of the calculated binding energies of CH_4 , C_2H_2 , C_2H_4 , and C_2H_6 to the results from experimental heat of adsorption (ΔH) and theoretical binding energy (BE) results of molecules in MOF-74-Mg and their diffusion barriers for considered diffusion mechanism.

Molecule	BE (eV)			Diffusion Barrier (eV)		
	This work	Literature		M1a	M1b	M2
		Exp. (ΔH)	Calc. (BE)			
CH_4	-0.30	-0.20 ¹¹⁰	-0.26 ⁵⁸ , -0.30 ¹⁵³	0.09	0.21	0.14
C_2H_2	-0.48	-0.43 ¹⁷³	-0.40 ⁵⁸ , -0.48 ¹⁵³	0.16	0.28	0.33
C_2H_4	-0.53	-0.45 ¹¹⁶ , -0.43 ¹¹⁷	-0.47 ¹¹³ , -0.55 ¹²⁹	0.18	0.35	0.31
C_2H_6	-0.39	-0.37 ¹¹⁶ , -0.29 ¹¹⁷	-0.31 ¹¹³ , -0.40 ¹²⁹	0.06	0.22	0.18
H_2O	-0.79	-0.76 ¹⁷⁴	-0.79 ⁵⁹	0.65	0.48	0.65

Before delving into the computational investigation of the diffusion of the small hydrocarbons, we reproduced and made a benchmarking study on the diffusion properties of H_2O molecule from CI-NEB calculation which is confirmed with experimental time-resolved IR spectroscopy.¹⁶⁰

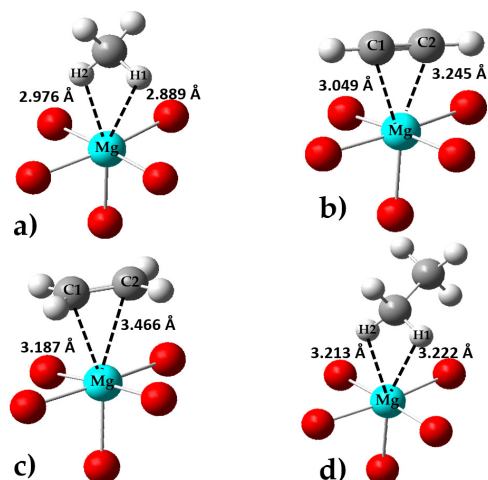


Figure 6.2 Molecular spatial orientation of CH_4 , C_2H_2 , C_2H_4 , and C_2H_6 at the open metal sites in the MOF-74-Mg.

The computed diffusion energy barrier for the diffusion mechanisms *M1a* and *M2* were found to be 0.65 eV and 0.62 eV respectively. This is an excellent agreement with the work of Canepa *et al.*¹⁶⁰ Figure 6.4 shows the diffusion profiles for the diffusion mechanisms *M1a* and *M2*. In both diffusion mechanisms, (*M1a* and *M1b*), ethylene suffers from the highest diffusion barrier while methane and ethane are energetically privileged for light diffusion barriers.

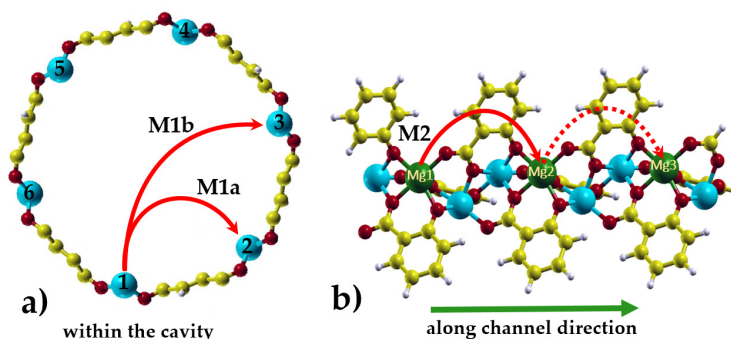


Figure 6.3 Diffusion mechanisms, (a) *M1a* refers to the diffusion mechanism from one open metal site to the nearest site while *M1b* refers to the diffusion from one open metal site to the next nearest open metal center within the cavity. (b) *M2* refers to diffusion along the channel direction when molecules hop from one open metal site the nearest open metal along the longitudinal channel direction. The green spheres represent open metal centers along the MgO_5 chain belonging to the same longitudinal channel.

Even though it isn't very distinct for CH_4 and C_2H_6 , a general trend was identified such that the stronger the binding energy of the molecules to the open metal site, the higher

diffusion barrier the molecules encountered. For all the small hydrocarbons considered in this study, diffusion mechanism *M1a* is significantly energetically favorable than *M1b* showing that it's easier for molecules to drift along the longitudinal cavity than staying cross-sectionally within the cavity.

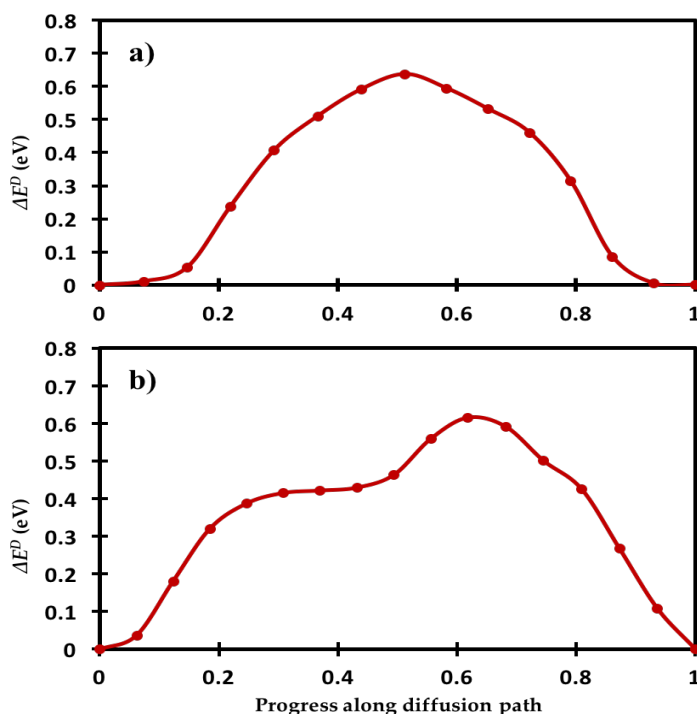


Figure 6.4 Diffusion profile of water molecule in pristine MOF-74-Mg, a) Diffusion mechanism *M1a*, diffusion mechanism where a molecule diffuses from one open metal site to the next nearest open metal site within the cavity and b) Diffusion mechanism *M2*, diffusion along the channel direction when a molecule is hopping from one open metal site the nearest open metal along the longitudinal channel direction

Figure 6.5a shows diffusion profiles of diffusion mechanism *M1a* for CH₄, C₂H₂, C₂H₄, C₂H₆ molecules. For *M1a*, the unsaturated hydrocarbons (C₂H₂ and C₂H₄) suffer from higher diffusion barrier compared to those saturated hydrocarbons (CH₄ and C₂H₆) with barrier difference ranging between 0.07 to 0.12 eV. Figure 6.5b shows diffusion profiles for *M1b* for the small hydrocarbon molecules. Similarly, for *M1b*, the unsaturated hydrocarbons exhibit higher diffusion energy barrier which can go up to 0.14 eV. For diffusion along the MOFs channel, the diffusion profiles in Figure 6.5c indicate that the unsaturated hydrocarbons suffer significantly from higher diffusion barrier when compared to the saturated molecules with differential barrier of 0.2 eV. An interesting trend is

observed across all the diffusion mechanisms in that the stronger the molecule binds to the open metal site, the higher the diffusion barrier faced. The diffusion profile of ethane exhibits a substantial depression around 45% along the diffusion path, indication a possible secondary binding site near mid away between two adjacent open metal sites along the cavity.

In all the cases of the diffusion mechanisms, ethylene and acetylene suffer from the highest diffusion barrier while methane and ethane are energetically privileged for light diffusion barriers. Even though it isn't very distinct for CH₄ and C₂H₆, a general trend was identified such that the stronger the binding energy of the molecules to the open metal site, the higher diffusion barrier the molecules encountered.

For all the small hydrocarbons considered in this study, diffusion mechanism ***M1a*** is significantly energetically favorable than ***M1b*** showing that it's easier for molecules to drift along the longitudinal cavity than staying cross-sectionally within the cavity. Particularly, looking at ethylene and ethane, diffusion properties for diffusions mechanism ***M1a***, ***M1b*** and ***M2***, reveal that ethylene suffers quit strong diffusion barriers which can be up to 0.2 eV over ethane (see Table 6.1). This indicates that a mixture of such light hydrocarbon molecules diffusing through the MOF cavities will experience significant differential diffusion barriers; as such it confirms MOF-74-Mg as a material of potential industrial application toward the efficient separation of olefin-paraffin mixtures.

To address the role played by pre-adsorbed contaminants such as H₂O molecules on the diffusion of small hydrocarbon molecules, two diffusion mechanisms were considered. In mechanism ***M1b***, molecules are allowed hopping from one open metal site to the second nearest site within the same cross-section; within this scenario, two different situations are envisioned where (a) hydrocarbon molecules diffuse under de-hydrated with no presence of water molecule on the nearest open metal site, and (b) hydrated conditions, where there is a presence of a water molecule on the nearest open metal site as show in Figure 6.6.

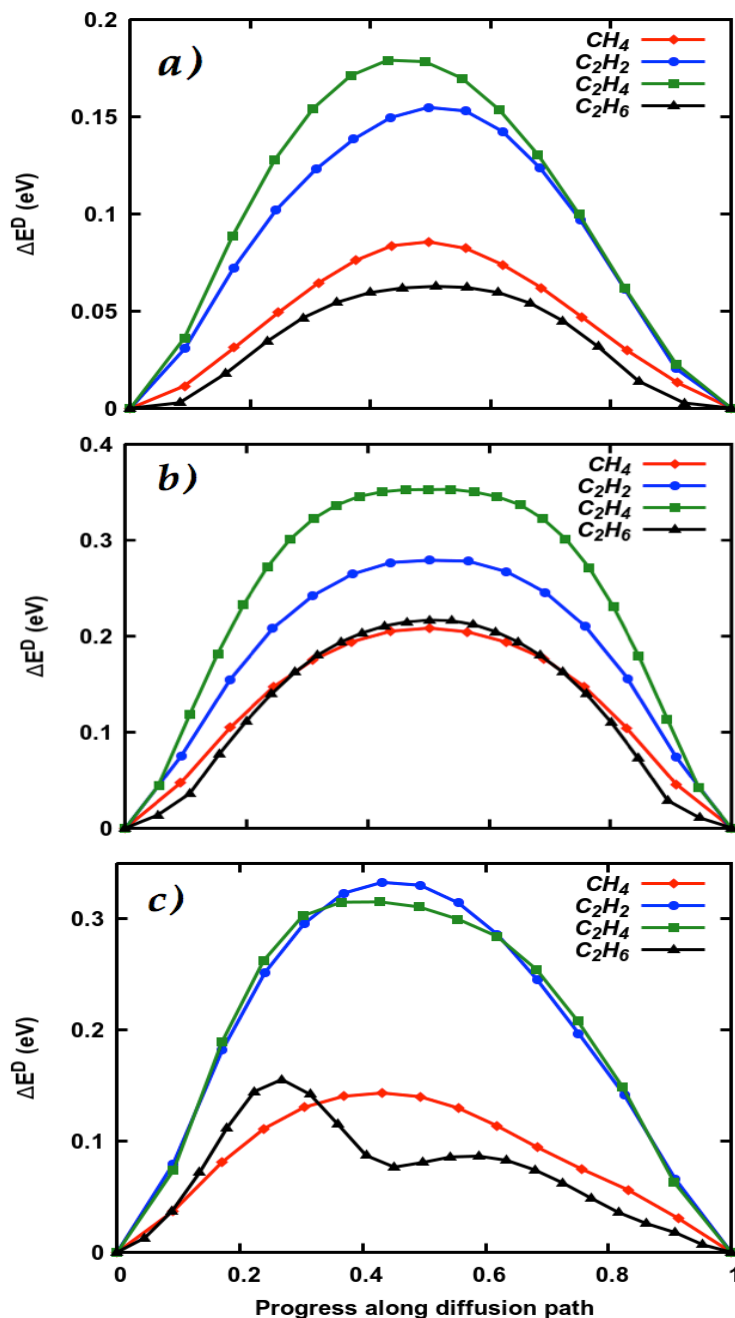


Figure 6.5 Diffusion profiles for the diffusion processes of CH_4 , C_2H_2 , C_2H_4 , and C_2H_6 for diffusion mechanism (a) *M1a* (b) *M1b* and (c) *M2* as described in Figure 6.3.

One solution to such problem would be the use of molecular cluster models containing at least three consecutive open metal sites along the metal oxide (MO_5) chain of the MOF's cavity. Even though the diffusion profiles of ethylene and ethane as in the PBC model were

accurately reproduced with use of such molecular models in the de-hydrated case, their respective diffusion calculations in the hydrated case were not successfully converged. Therefore, results pertaining to diffusing studies along hydrated MOF cavity are not reported.

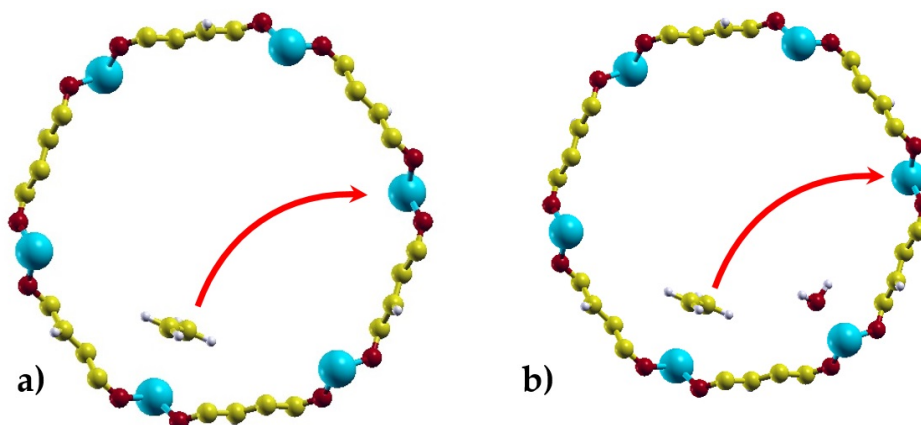


Figure 6.6 Diffusion mechanism M1b. (a) Diffusion from one open metal in the pristine periodic structure to the next nearest site (b) diffusion from one open metal site to the next nearest in Hydrated MOF where there is a presence of pre-adsorbed H₂O molecule on the nearest metal center. The aqua, red, yellow and white spheres represent Magnesium, oxygen, carbon and hydrogen atoms respectively in the unit cell of MOF-74-Mg.

Figure 6.7 shows the diffusion profiles for ethylene and ethane molecules for the diffusion mechanism *M1b* in pristine and hydrated MOF cavity. While the presence of water barely influences the diffusion of ethylene, ethane experiences an increased in energy barrier of 0.05 eV. This seemed to be mainly due to the relative steric hindrance experienced by the two hydrocarbon molecules due their size differences. As such, one can see that the bigger the size of the molecule the greater the effect of the presence of pre-adsorbed foreign molecules like water on their diffusion process.

6.4 Summary

In summary, this work provides a detailed description of the molecular transport processes of CH₄, C₂H₂, C₂H₄ and C₂H₆ within and along the cavity of MOF-74-Mg and made an effort to study the extent to which the presence pre-adsorbed foreign molecules affect the diffusion process of small hydrocarbon molecules. Throughout all the diffusion mechanisms considered, the CI-NEB diffusion property study shows that the diffusion of

paraffin molecules in MOF-74-Mg is energetically more favorable than that of olefin molecules.

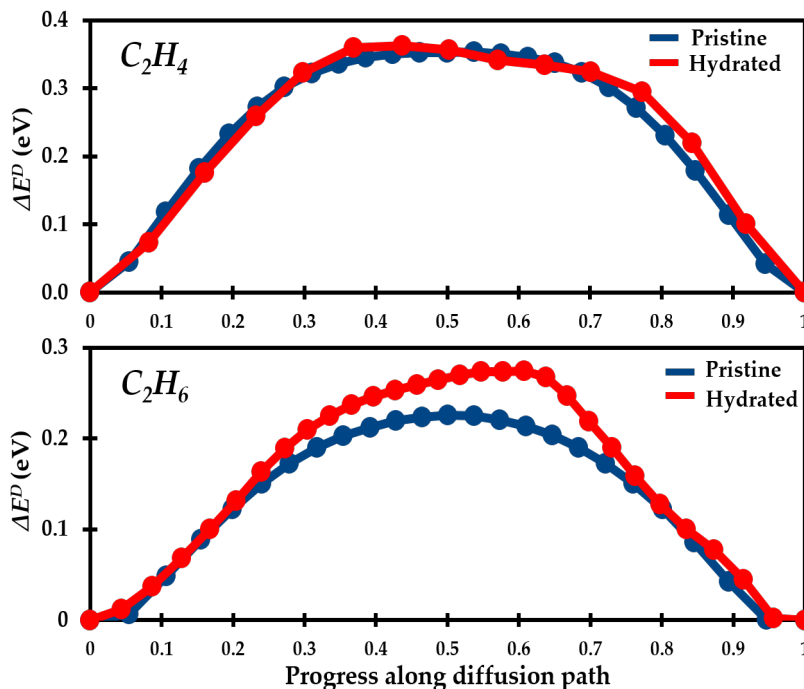


Figure 6.7 Diffusion profile comparison: pristine MOF cavity (blue) to hydrated cavity (red). C_2H_4 (upper panel) and C_2H_6 (lower panel) for diffusion mechanism *M1b*.

The differential diffusion barrier of olefin-paraffin was computed to be as significant as 0.20 eV. Together with study of the heats of adsorption, lateral interaction, and IR frequency shifts presented in previous chapters, a quantum mechanical comprehensive description of the binding and diffusion processes of these molecules in MOF-74-Mg is now made available at periodic boundary conditions approach. The same methodology can not only be successfully applied to reveal the molecular transport in other MOF-74 isostructural species, but also in the fundamental understanding of the screening of MOFs and other nano-porous materials for gas separation applications. In addition, it can be used to aid in further understanding challenging diffusion experimental results.

7 Summary and Future Perspectives

7.1 Summary

First-principle density functional theory (DFT) calculations were performed to study the physicochemical adsorption and spectroscopic properties, and diffusion mechanisms of small hydrocarbon molecules (CH_4 , C_2H_2 , C_2H_4 , C_2H_6 , C_3H_6 , C_3H_8 , C_4H_8 , and C_4H_{10}) in MOF-74-M ($\text{M}=\text{Mg}$, Zn) to assess the potential of these nanoporous frameworks as energy efficient alternative materials for hydrocarbon gas mixture separation application in petroleum refining industries.

First, the investigation was conducted with respect to two molecular cluster models representing the adsorption neighborhood of the two MOF-74 isostructural species, to investigate the relative energetic interaction of olefin and paraffin molecules at the open metal sites in MOFs. Results from this investigation showed that olefins interact more energetically to the open metal sites than their paraffin counterparts with differential binding energies ranging from 8 to 18 kJ/mol. This indicates that a mixture of light hydrocarbons flowing through the MOFs' cavities are selectively separated. Within a few kJ/mol, the same degree of separation capability is shown by both MOFs with respect to the two functionals considered (B3LYP+D2* and M06), regardless of the size of the molecular cluster models. For each hydrocarbon molecule, underestimation of the binding energy was observed to be increasing as molecular size increases, indicating the importance of considering a more chemically meaningful molecular cluster when larger molecules are studied. In addition, it was also noted how for the saturated hydrocarbons, dispersion forces are solely responsible for the strength of the binding.

In the second project, 3D PBC calculations on periodic structures of MOF-74-Mg/Zn were performed to investigate the role of the inclusion of the complete MOFs chemical environment and the influence of the lateral interaction on the binding energies of adsorbed C_1 - C_4 hydrocarbon molecules. For these purposes, three different molecular loadings were imposed. The inclusion of the full chemical environment experienced by the adsorbed

hydrocarbon molecules, allowed for a more complete appreciation of the importance of accounting for the presence of the framework, which is otherwise partially included when the molecular cluster models are adopted. In addition, binding energies corrected for the basis set superposition error (BSSE) were determined and further corrected to include the contributions due to zero-point energy (ZPE) and finite-temperature thermal energy (TE). All the listed contribution and corrections allow for the adequate comparison of calculated enthalpies with respect to available calorimetric experimental heats of adsorptions. Based on computed binding energies, the intermolecular distances between small molecules are large enough to only minimally influence the results even in the high molecular loading case. As molecular size increases a clear trend is observed where the binding energy increases with the increase of the repulsive lateral interaction, which is computed to be as high as 16 kJ/mol for butane, the biggest of the hydrocarbon considered. It is worth stressing that the lack of an accurate account of dispersion contribution may play a significant role in the underestimation of binding energies calculated from molecular cluster models when compared to that obtained within PBC approaches. When compared to the results obtained from the modeling of their corresponding PBC structures, the molecular cluster models were observed to underestimate the binding energies by as much as 25 kJ/mol. This work shows how the inclusion of the proper chemical environment plays a crucial role in estimation of the binding energies of molecules adsorbed in MOFs.

In the third project, IR spectra for CH₄, C₂H₂, C₂H₄, and C₂H₆ hydrocarbons in MOF-74-Mg were studied. Band locations, intensities, and frequency shifts across the three PBC models were presented with respect to the three different molecular loadings. Intermolecular lateral interaction and spatial arrangement of the molecules at the adsorption sites were observed to play a dramatic role for the computed energetics and IR frequency shifts. While energetics and spectra for methane are only minimally influenced by these aspects, acetylene is found to be highly affected not only by the open metal site but also by the ligands' terminations. For the larger ethylene and ethane molecules, wide frequency shifts (up to 34 cm⁻¹) are observed together with the gradual appearance of structured bands corresponding to the different molecular loadings. The analysis of the

computed IR spectra reported in this work, can provide useful information for the interpretation of experimental spectroscopic observations which is currently still lacking. In addition, this investigation can provide an aid to understand in more detail the physicochemical nature of the host-guest interactions.

In the fourth and final project, climbing-image nudge elastic band (CI-NEB) calculations were performed to study the molecular transport processes of CH₄, C₂H₂, C₂H₄ and C₂H₆ within and along the cavity of MOF-74-Mg. In addition, an effort was also made to study the extent to which the presence of pre-adsorbed foreign contaminant molecules, such as H₂O, affects the diffusion process of the hydrocarbon molecules. The study showed that the diffusion of paraffin molecules in MOF-74-Mg is energetically more favorable than that of olefin counterparts. The differential diffusion barrier of olefin-paraffin pairs was computed to be as significant as 0.20 eV (19.25 kJ/mol). Interestingly, while the presence of a water molecule barely influences the diffusion profile of ethylene, ethane experiences an increase in the diffusion energy barrier of 0.05 eV (4.8 kJ/mol) for the mechanism within the framework cavity. Such an observation can be explained as being mainly due to the different steric hindrance experienced by the larger hydrocarbon molecule.

Overall, together with the study of heats of adsorption, lateral interaction, and IR frequency shifts presented in this work, a quantum mechanical comprehensive description of the adsorptive separation ability and the diffusion processes of small hydrocarbon molecules in MOF-74-Mg (and, partially, in MOF-74-Zn) is now made available within PBC approach.

7.2 Future Perspective

In this work, it is demonstrated that MOF-74-Mg/Zn can be a promising material for energy efficient hydrocarbon gas mixture separation technology. Although the quantum mechanical description of MOF materials can be challenging and computationally demanding due to structural complexity, *e.i.*, a large number of irreducible atoms per unit

cell, and in some cases the low symmetry of the structures, there are other modeling aspects which are of scientific interest.

The investigation of the effect of different open metal sites can be an immediate extension of the work presented herein. In fact, similarly to how Mg and Zn open metals sites were explored in this work, other transition metals such as Fe, Ni, Cu, etc. can be investigated as adsorption sites. In this work, MOF-74-M was explored where M was either Mg or Zn atoms uniformly distributed throughout the MOFs' structures. However, it is possible to consider mixtures (*i.e.*, solid solutions) of different open metal centers that may be able to enhance the differential binding energies of olefin-paraffin pairs. For instance, such solid solutions can be investigated by considering 30% of Fe, 30% of Zn, and 40% of Mg metal atoms just in a single MOF structure. In addition, the insertion of open shell transition metals, may be of interest for applications involving spin polarized solutions (*i.e.*, sensors and molecular switches).

Further investigations can also be conducted by functionalizing the organic *linkers* present in the MOF structures. Ligand functionalization in MOFs has been demonstrated to enhance gas adsorption and induce promising gas adsorption phenomena. In fact, while ligand functionalization does not change the basic overall structure of the parent frameworks, it can influence their gas adsorption behavior. The functionalization of the ligand can be achieved mainly in two ways, following the concepts grounded by reticular chemistry. A first approach would consist of introducing longer and longer organic ligand chains connecting the metal nodes; this would result in the creation of isorecticular families of the original MOF (IR-MOF). This type of functionalization largely influences the porosity (surface area and pore volume) and pore structure (pore size and pore shape) which allow for the accommodation of more molecules per unit cell. Second, ligand functionalization can also be achieved by adding a functional group to the parent ligand. This second method is mainly focused on a fine-tuning of the electronic properties of the parent MOF structure and is expected to influence the interaction of the host-guest complex.

The insights arising from the diffusion study, allow for extension to bigger hydrocarbon molecules. The details of the work reported herein constitute a significant and original starting point that can be extended to other MOFs but also to other porous materials to address their potential for applications such gas storage, toxic gas sensing, and catalysis.

Appendix A Permission to use Figure 1.1

RightsLink Printable License

3/5/18, 9:04 PM

SPRINGER NATURE LICENSE TERMS AND CONDITIONS

Mar 05, 2018

This Agreement between Mr. Gemechis Degaga ("You") and Springer Nature ("Springer Nature") consists of your license details and the terms and conditions provided by Springer Nature and Copyright Clearance Center.

License Number	4300240481606
License date	Mar 01, 2018
Licensed Content Publisher	Springer Nature
Licensed Content Publication	Nature
Licensed Content Title	Reticular synthesis and the design of new materials
Licensed Content Author	Omar M. Yaghi, Michael O'Keeffe, Nathan W. Ockwig, Hee K. Chae, Mohamed Eddaoudi et al.
Licensed Content Date	Jun 12, 2003
Licensed Content Volume	423
Licensed Content Issue	6941
Type of Use	Journal/Magazine
Requestor type	academic/university or research institute
Format	print and electronic
Portion	figures/tables/illustrations
Number of figures/tables/illustrations	1
High-res required	no
Will you be translating?	no
Circulation/distribution	<501
Author of this Springer Nature content	no
Title	PHYSICOCHEMICAL, SPECTROSCOPIC PROPERTIES, AND DIFFUSION MECHANISMS OF SMALL HYDROCARBON MOLECULES IN MOF-74 ISOSTRUCTURES: A QUANTUM CHEMICAL INVESTIGATION
Author	Gemechis Degaga
Publication	Dissertation
Publisher	Michigan Technological University
Publisher imprint	
Expected publication date	May 2018

<https://s100.copyright.com/CustomerAdmin/PLF.jsp?ref=6af1c1eb-a1f1-4e06-9131-dec461970963>

Page 1 of 4

Appendix B Permission to use Figure 1.2

RightsLink Printable License

3/5/18, 8:44 PM

ROYAL SOCIETY OF CHEMISTRY LICENSE TERMS AND CONDITIONS

Mar 05, 2018

This Agreement between Mr. Gemechis Degaga ("You") and Royal Society of Chemistry ("Royal Society of Chemistry") consists of your license details and the terms and conditions provided by Royal Society of Chemistry and Copyright Clearance Center.

License Number	4302771262686
License date	Mar 05, 2018
Licensed Content Publisher	Royal Society of Chemistry
Licensed Content Publication	Chemical Society Reviews
Licensed Content Title	Multifunctional metal-organic frameworks: from academia to industrial applications
Licensed Content Author	Patrícia Silva,Sérgio M. F. Vilela,João P. C. Tomé,Filipe A. Almeida Paz
Licensed Content Date	Jul 2, 2015
Licensed Content Volume	44
Licensed Content Issue	19
Type of Use	Thesis/Dissertation
Requestor type	academic/educational
Portion	figures/tables/images
Number of figures/tables/images	1
Format	print and electronic
Distribution quantity	140
Will you be translating?	no
Order reference number	
Title of the thesis/dissertation	PHYSICOCHEMICAL, SPECTROSCOPIC PROPERTIES, AND DIFFUSION MECHANISMS OF SMALL HYDROCARBON MOLECULES IN MOF-74 ISOSTRUCTURES: A QUANTUM CHEMICAL INVESTIGATION
Expected completion date	May 2018
Estimated size	140
Requestor Location	Mr. Gemechis Degaga 1901 Woodmar Drive Apt B HOUGHTON, MI 49931 United States Attn: Mr. Gemechis Degaga

<https://s100.copyright.com/CustomerAdmin/PLF.jsp?ref=da2ec0fb-b353-43dc-bcef-a7becd0b0d7d>

Page 1 of 5

Appendix C Permission to use Figure 1.3

RightsLink Printable License

3/5/18, 5:19 PM

THE AMERICAN ASSOCIATION FOR THE ADVANCEMENT OF SCIENCE LICENSE TERMS AND CONDITIONS

Mar 05, 2018

This Agreement between Mr. Gemechis Degaga ("You") and The American Association for the Advancement of Science ("The American Association for the Advancement of Science") consists of your license details and the terms and conditions provided by The American Association for the Advancement of Science and Copyright Clearance Center.

License Number	4300400599693
License date	Mar 01, 2018
Licensed Content Publisher	The American Association for the Advancement of Science
Licensed Content Publication	Science
Licensed Content Title	Systematic Design of Pore Size and Functionality in Isoreticular MOFs and Their Application in Methane Storage
Licensed Content Author	Mohamed Eddaoudi,Jaheon Kim,Nathaniel Rosi,David Vodak,Joseph Wachter,Michael O'Keeffe,Omar M. Yaghi
Licensed Content Date	Jan 18, 2002
Licensed Content Volume	295
Licensed Content Issue	5554
Volume number	295
Issue number	5554
Type of Use	Thesis / Dissertation
Requestor type	Scientist/individual at a research institution
Format	Print and electronic
Portion	Figure
Number of figures/tables	1
Order reference number	
Title of your thesis / dissertation	PHYSICOCHEMICAL, SPECTROSCOPIC PROPERTIES, AND DIFFUSION MECHANISMS OF SMALL HYDROCARBON MOLECULES IN MOF-74 ISOSTRUCTURES: A QUANTUM CHEMICAL INVESTIGATION
Expected completion date	May 2018
Estimated size(pages)	140
Requestor Location	Mr. Gemechis Degaga 1901 Woodmar Drive Apt B HOUGHTON, MI 49931 United States

<https://s100.copyright.com/CustomerAdmin/PLF.jsp?ref=01267f7e-c356-48bd-a3ec-af735343d0c7>

Page 1 of 7

Appendix D Permission to use Figure 1.4

Gemechis <gdegaga@mtu.edu>

Mar 6 (2 days ago) ☆

to PNASpermissions ▾

Dear all,

I would like to have your permission to use Figure 2 of your paper titled '[Highly efficient separation of carbon dioxide by a metal-organic framework replete with open metal sites](#)' for my Ph.D. dissertation titled 'PHYSICOCHEMICAL, SPECTROSCOPIC PROPERTIES, AND DIFFUSION MECHANISMS OF SMALL HYDROCARBON MOLECULES IN MOF-74 ISOSTRUCTURES: A QUANTUM CHEMICAL INVESTIGATION' for my introduction/review chapter.

Thank you so much for your time and cooperation.

Gemechis

Gemechis D. Degaga
Michigan Technological University
PhD Candidate
1400 Townsend DR--49931
Houghton Michigan
USA
Tel: [+1 906 281 8149](tel:+19062818149)

PNAS Permissions

3:52 PM (49 minutes ago) ☆

to me ▾

Permission is granted for your use of the figure as described in your message. Please list a full citation for the PNAS article when re-using the material. Because this material published after 2008, a copyright note is not needed. There is no charge for this material, either. Let us know if you have any questions.

Best regards,
Kay McLaughlin for
Diane Sullenberger
Executive Editor
PNAS

Appendix E Permission to use Figure 1.5

RightsLink Printable License

3/6/18, 1:56 PM

ELSEVIER LICENSE TERMS AND CONDITIONS

Mar 06, 2018

This Agreement between Mr. Gemechis Degaga ("You") and Elsevier ("Elsevier") consists of your license details and the terms and conditions provided by Elsevier and Copyright Clearance Center.

License Number	4303181281584
License date	Mar 06, 2018
Licensed Content Publisher	Elsevier
Licensed Content Publication	Inorganica Chimica Acta
Licensed Content Title	A review on contemporary Metal–Organic Framework materials
Licensed Content Author	Kranthi Kumar Gangu, Suresh Maddila, Saratchandra Babu Mukkamala, Sreekantha B. Jonnalagadda
Licensed Content Date	1 May 2016
Licensed Content Volume	446
Licensed Content Issue	n/a
Licensed Content Pages	14
Start Page	61
End Page	74
Type of Use	reuse in a thesis/dissertation
Intended publisher of new work	other
Portion	figures/tables/illustrations
Number of figures/tables/illustrations	1
Format	both print and electronic
Are you the author of this Elsevier article?	No
Will you be translating?	No
Original figure numbers	Fig. 1. Year wise publication status from 2000 to 2015 of various aspects of MOFs (a) MOFs, (b) MOFs as luminescent materials, (c) MOFs for gas storage, (d) MOFs as magnets, (e) MOFs for drug delivery and (f) MOFs as catalyst (data source: Sci-finder, ret
Title of your thesis/dissertation	PHYSICOCHEMICAL, SPECTROSCOPIC PROPERTIES, AND DIFFUSION MECHANISMS OF SMALL HYDROCARBON MOLECULES IN MOF-74 ISOSTRUCTURES: A QUANTUM CHEMICAL INVESTIGATION
Expected completion date	May 2018

<https://s100.copyright.com/CustomerAdmin/PLF.jsp?ref=8f630c65-2e1b-4735-afed-a03a12396c97>

Page 1 of 7

Appendix F Permission to use materials in Chapter 3



[Home](#) [Account Info](#) [Help](#) 



Title: Part I: C2 C4 hydrocarbons separation addressed via molecular cluster models carved out from periodic MOF-74-Mg/Zn structures

Author: Gemechis D. Degaga, Loredana Valenzano

Publication: Chemical Physics Letters

Publisher: Elsevier

Date: 1 September 2016



© 2016 Elsevier B.V. All rights reserved.


Logged in as:
Gemechis Degaga
Account #: 3001255454


[LOGOUT](#)

Please note that, as the author of this Elsevier article, you retain the right to include it in a thesis or dissertation, provided it is not published commercially. Permission is not required, but please ensure that you reference the journal as the original source. For more information on this and on your other retained rights, please visit: <https://www.elsevier.com/about/our-business/policies/copyright#Author-rights>

Appendix G Permission to use materials in Chapter 4



[Home](#) [Account Info](#) [Help](#) 



Title: Part II: Quantum mechanical prediction of heats of adsorption for C2-C4 hydrocarbons in MOF-74-Mg/Zn periodic structures

Author: Gemechis D. Degaga, Loredana Valenzano

Publication: Chemical Physics Letters

Publisher: Elsevier

Date: 16 August 2017

© 2017 Elsevier B.V. All rights reserved.

Logged in as:
Gemechis Degaga
Account #:
3001255454

[LOGOUT](#)

Please note that, as the author of this Elsevier article, you retain the right to include it in a thesis or dissertation, provided it is not published commercially. Permission is not required, but please ensure that you reference the journal as the original source. For more information on this and on your other retained rights, please visit: <https://www.elsevier.com/about/our-business/policies/copyright#Author-rights>

Appendix H Permission to use materials in Chapter 5

RightsLink Printable License

3/6/18, 2:40 PM

SPRINGER NATURE LICENSE TERMS AND CONDITIONS

Mar 06, 2018

This Agreement between Mr. Gemechis Degaga ("You") and Springer Nature ("Springer Nature") consists of your license details and the terms and conditions provided by Springer Nature and Copyright Clearance Center.

License Number	4303200880556
License date	Mar 06, 2018
Licensed Content Publisher	Springer Nature
Licensed Content Publication	Theoretical Chemistry Accounts
Licensed Content Title	Quantum chemistry as a tool to assess energetic and spectroscopic properties of C1 and C2 hydrocarbons in MOF-74-Mg
Licensed Content Author	Gemechis D. Degaga, Loredana Valenzano
Licensed Content Date	Jan 1, 2018
Licensed Content Volume	137
Licensed Content Issue	3
Type of Use	Thesis/Dissertation
Requestor type	academic/university or research institute
Format	print and electronic
Portion	full article/chapter
Will you be translating?	no
Circulation/distribution	501 to 1000
Author of this Springer Nature content	yes
Title	PHYSICOCHEMICAL, SPECTROSCOPIC PROPERTIES, AND DIFFUSION MECHANISMS OF SMALL HYDROCARBON MOLECULES IN MOF-74 ISOSTRUCTURES: A QUANTUM CHEMICAL INVESTIGATION
Instructor name	n/a
Institution name	n/a
Expected presentation date	May 2018
Requestor Location	Mr. Gemechis Degaga 1901 Woodmar Drive Apt B HOUGHTON, MI 49931 United States Attn: Mr. Gemechis Degaga

<https://s100.copyright.com/CustomerAdmin/PLF.jsp?ref=afbef71f-bfc3-43c7-9216-f73503d8cdee>

Page 1 of 4

Bibliography

1. Yaghi, O. M., A tale of two entanglements. *Nat Mater* **2007**, 6 (2), 92-93.
2. Yaghi, O. M., Metal-Organic Frameworks and Their Applications to Energy. In *BASF Science Symposium*, SCIENCE, B., Ed. Ludwigshafen, Germany, 2015.
3. Manzeli, S.; Ovchinnikov, D.; Pasquier, D.; Yazyev, O. V.; Kis, A., 2D transition metal dichalcogenides. *Nat Rev Mater* **2017**, 2 (8).
4. Yu, X. W.; Cheng, H. H.; Zhang, M.; Zhao, Y.; Qu, L. T.; Shi, G. Q., Graphene-based smart materials. *Nat Rev Mater* **2017**, 2 (9).
5. Zhang, Q.; Huang, J. Q.; Qian, W. Z.; Zhang, Y. Y.; Wei, F., The Road for Nanomaterials Industry: A Review of Carbon Nanotube Production, Post-Treatment, and Bulk Applications for Composites and Energy Storage. *Small* **2013**, 9 (8), 1237-1265.
6. Silva, P.; Vilela, S. M. F.; Tome, J. P. C.; Paz, F. A. A., Multifunctional metal-organic frameworks: from academia to industrial applications. *Chem Soc Rev* **2015**, 44 (19), 6774-6803.
7. Janiak, C.; Vieth, J. K., MOFs, MILs and more: concepts, properties and applications for porous coordination networks (PCNs). *New J Chem* **2010**, 34 (11), 2366-2388.
8. Yaghi, O. M.; O'Keeffe, M.; Ockwig, N. W.; Chae, H. K.; Eddaoudi, M.; Kim, J., Reticular synthesis and the design of new materials. *Nature* **2003**, 423 (6941), 705-714.
9. Gangu, K. K.; Maddila, S.; Mukkamala, S. B.; Jonnalagadda, S. B., A review on contemporary Metal-Organic Framework materials. *Inorg Chim Acta* **2016**, 446, 61-74.
10. Yaghi, O. M.; Li, G. M., The Design of Open-Framework Solids Containing Channels Using Molecular Metal-Organic Building-Blocks. *Abstr Pap Am Chem S* **1995**, 209, 284-Inor.
11. Yaghi, O. M., Reticular Chemistry-Construction, Properties, and Precision Reactions of Frameworks. *Journal of the American Chemical Society* **2016**, 138 (48), 15507-15509.
12. Ferey, G., Hybrid porous solids: past, present, future. *Chem Soc Rev* **2008**, 37 (1), 191-214.
13. Forster, P. M.; Burbank, A. R.; Livage, C.; Ferey, G.; Cheetham, A. K., The role of temperature in the synthesis of hybrid inorganic-organic materials: the example of cobalt succinates. *Chem Commun (Camb)* **2004**, (4), 368-9.
14. Banerjee, D.; Hu, Z.; Li, J., Luminescent metal-organic frameworks as explosive sensors. *Dalton Trans* **2014**, 43 (28), 10668-85.
15. Cook, T. R.; Zheng, Y. R.; Stang, P. J., Metal-Organic Frameworks and Self-Assembled Supramolecular Coordination Complexes: Comparing and Contrasting the Design, Synthesis, and Functionality of Metal-Organic Materials. *Chem Rev* **2013**, 113 (1), 734-777.
16. Tranchemontagne, D. J.; Mendoza-Cortes, J. L.; O'Keeffe, M.; Yaghi, O. M., Secondary building units, nets and bonding in the chemistry of metal-organic frameworks. *Chem Soc Rev* **2009**, 38 (5), 1257-1283.
17. Berry, G. D.; Aceves, S. M., Onboard storage alternatives for hydrogen vehicles. *Energ Fuel* **1998**, 12 (1), 49-55.
18. Eddaoudi, M.; Kim, J.; Rosi, N.; Vodak, D.; Wachter, J.; O'Keeffe, M.; Yaghi, O. M., Systematic design of pore size and functionality in isoreticular MOFs and their application in methane storage. *Science* **2002**, 295 (5554), 469-472.

19. Rosi, N. L.; Eckert, J.; Eddaoudi, M.; Vodak, D. T.; Kim, J.; O'Keeffe, M.; Yaghi, O. M., Hydrogen storage in microporous metal-organic frameworks. *Science* **2003**, *300* (5622), 1127-1129.
20. Yang, S. J.; Kim, T.; Im, J. H.; Kim, Y. S.; Lee, K.; Jung, H.; Park, C. R., MOF-Derived Hierarchically Porous Carbon with Exceptional Porosity and Hydrogen Storage Capacity. *Chem Mater* **2012**, *24* (3), 464-470.
21. Guo, Z. Y.; Wu, H.; Srinivas, G.; Zhou, Y. M.; Xiang, S. C.; Chen, Z. X.; Yang, Y. T.; Zhou, W.; O'Keeffe, M.; Chen, B. L., A Metal-Organic Framework with Optimized Open Metal Sites and Pore Spaces for High Methane Storage at Room Temperature. *Angew Chem Int Edit* **2011**, *50* (14), 3178-3181.
22. An, J.; Rosi, N. L., Tuning MOF CO₂ Adsorption Properties via Cation Exchange. *Journal of the American Chemical Society* **2010**, *132* (16), 5578-+.
23. Barea, E.; Montoro, C.; Navarro, J. A. R., Toxic gas removal - metal-organic frameworks for the capture and degradation of toxic gases and vapours. *Chem Soc Rev* **2014**, *43* (16), 5419-5430.
24. Britt, D.; Tranchemontagne, D.; Yaghi, O. M., Metal-organic frameworks with high capacity and selectivity for harmful gases. *P Natl Acad Sci USA* **2008**, *105* (33), 11623-11627.
25. Britt, D.; Tranchemontagne, D.; Yaghi, O. M., INOR 762-Reticular metal-organic frameworks for air purification. *Abstr Pap Am Chem S* **2008**, 235.
26. Furukawa, H.; Cordova, K. E.; O'Keeffe, M.; Yaghi, O. M., The Chemistry and Applications of Metal-Organic Frameworks. *Science* **2013**, *341* (6149), 974-+.
27. Czaja, A. U.; Trukhan, N.; Muller, U., Industrial applications of metal-organic frameworks. *Chem Soc Rev* **2009**, *38* (5), 1284-1293.
28. Maji, T. K.; Mostafa, G.; Chang, H. C.; Kitagawa, S., Porous lanthanide-organic framework with zeolite-like topology. *Chem Commun* **2005**, (19), 2436-2438.
29. Jian-Rong Li, R. J. K. a. H.-C. Z., Selective gas adsorption and separation in metal-organic frameworks. *Chem. Soc. Rev* **2009**, *5* (38), 1477-1504.
30. Britt, D.; Furukawa, H.; Wang, B.; Glover, T. G.; Yaghi, O. M., Highly efficient separation of carbon dioxide by a metal-organic framework replete with open metal sites. *P Natl Acad Sci USA* **2009**, *106* (49), 20637-20640.
31. Fujita, M.; Kwon, Y. J.; Washizu, S.; Ogura, K., Preparation, Clathration Ability, and Catalysis of a 2-Dimensional Square Network Material Composed of Cadmium(II) and 4,4'-Bipyridine. *Journal of the American Chemical Society* **1994**, *116* (3), 1151-1152.
32. Davis, M. E., New Vistas in Zeolite and Molecular-Sieve Catalysis. *Accounts Chem Res* **1993**, *26* (3), 111-115.
33. Lee, J.; Farha, O. K.; Roberts, J.; Scheidt, K. A.; Nguyen, S. T.; Hupp, J. T., Metal-organic framework materials as catalysts. *Chem Soc Rev* **2009**, *38* (5), 1450-1459.
34. Pan, Y. Y.; Yuan, B. Z.; Li, Y. W.; He, D. H., Multifunctional catalysis by Pd@MIL-101: one-step synthesis of methyl isobutyl ketone over palladium nanoparticles deposited on a metal-organic framework. *Chem Commun* **2010**, *46* (13), 2280-2282.
35. Ribeiro, S.; Barbosa, A. D. S.; Gomes, A. C.; Pillinger, M.; Goncalves, I. S.; Cunha-Silva, L.; Balula, S. S., Catalytic oxidative desulfurization systems based on Keggin phosphotungstate and metal-organic framework MIL-101. *Fuel Process Technol* **2013**, *116*, 350-357.

36. Ishida, T.; Nagaoka, M.; Akita, T.; Haruta, M., Deposition of Gold Clusters on Porous Coordination Polymers by Solid Grinding and Their Catalytic Activity in Aerobic Oxidation of Alcohols. *Chem-Eur J* **2008**, *14* (28), 8456-8460.
37. Yuan, B. Z.; Pan, Y. Y.; Li, Y. W.; Yin, B. L.; Jiang, H. F., A Highly Active Heterogeneous Palladium Catalyst for the Suzuki-Miyaura and Ullmann Coupling Reactions of Aryl Chlorides in Aqueous Media. *Angew Chem Int Edit* **2010**, *49* (24), 4054-4058.
38. Aijaz, A.; Karkamkar, A.; Choi, Y. J.; Tsumori, N.; Ronnebro, E.; Autrey, T.; Shioyama, H.; Xu, Q., Immobilizing Highly Catalytically Active Pt Nanoparticles inside the Pores of Metal-Organic Framework: A Double Solvents Approach. *Journal of the American Chemical Society* **2012**, *134* (34), 13926-13929.
39. Hasegawa, S.; Horike, S.; Matsuda, R.; Furukawa, S.; Mochizuki, K.; Kinoshita, Y.; Kitagawa, S., Three-dimensional porous coordination polymer functionalized with amide groups based on tridentate ligand: Selective sorption and catalysis. *Journal of the American Chemical Society* **2007**, *129* (9), 2607-2614.
40. Leffler, W. L., *Petroleum refining in nontechnical language*. PennWell Books: 2008.
41. Tranchemontagne, D. J.; Hunt, J. R.; Yaghi, O. M., Room temperature synthesis of metal-organic frameworks: MOF-5, MOF-74, MOF-177, MOF-199, and IRMOF-0. *Tetrahedron* **2008**, *64* (36), 8553-8557.
42. Ren, J. W.; Langmi, H. W.; North, B. C.; Mathe, M., Review on processing of metal-organic framework (MOF) materials towards system integration for hydrogen storage. *International Journal of Energy Research* **2015**, *39* (5), 607-620.
43. Kahr, J.; Morris, R. E.; Wright, P. A., Post-synthetic incorporation of nickel into CPO-27(Mg) to give materials with enhanced permanent porosity. *Crystengcomm* **2013**, *15* (45), 9779-9786.
44. Gandara, F.; Furukawa, H.; Lee, S.; Yaghi, O. M., High Methane Storage Capacity in Aluminum Metal-Organic Frameworks. *Journal of the American Chemical Society* **2014**, *136* (14), 5271-5274.
45. Azhin, M.; Kaghazchi, T.; Rahmani, M., A review on olefin/paraffin separation using reversible chemical complexation technology. *Journal of Industrial and Engineering Chemistry* **2008**, *14* (5), 622-638.
46. Mounfield, W. P.; Walton, K. S., Effect of synthesis solvent on the breathing behavior of MIL-53(Al). *Journal of Colloid and Interface Science* **2015**, *447*, 33-39.
47. Campello, S. L.; Gentil, G.; Junior, S. A.; de Azevedo, W. M., Laser ablation: A new technique for the preparation of metal-organic frameworks Cu-3(BTC)(2)(H₂O)(3). *Materials Letters* **2015**, *148*, 200-203.
48. He, Y.; Krishna, R.; Chen, B., Metal-organic frameworks with potential for energy-efficient adsorptive separation of light hydrocarbons. *Energy & Environmental Science* **2012**, *5* (10), 9107-9120.
49. Sen Gupta, A.; Deshpande, R. K.; Liu, L. J.; Waterhouse, G. I. N.; Telfer, S. G., Porosity in metal-organic frameworks following thermolytic postsynthetic deprotection: gas sorption, dye uptake and covalent derivatisation. *Crystengcomm* **2012**, *14* (18), 5701-5704.
50. Hirscher, M., Hydrogen Storage by Cryoadsorption in Ultrahigh-Porosity Metal-Organic Frameworks. *Angew Chem Int Edit* **2011**, *50* (3), 581-582.
51. Zhang, F. M.; Jin, Y.; Shi, J.; Zhong, Y. J.; Zhu, W. D.; El-Shall, M. S., Polyoxometalates confined in the mesoporous cages of metal-organic framework MIL-

- 100(Fe): Efficient heterogeneous catalysts for esterification and acetalization reactions. *Chemical Engineering Journal* **2015**, 269, 236-244.
52. Xie, Z. G.; Ma, L. Q.; deKrafft, K. E.; Jin, A.; Lin, W. B., Porous Phosphorescent Coordination Polymers for Oxygen Sensing. *Journal of the American Chemical Society* **2010**, 132 (3), 922-+.
53. Rachel C. Huxford, J. D. R., and Wenbin Lin, Metal-Organic Frameworks as Potential Drug Carriers. *Current Opinion in Chemical Biology* **2010** 14 (2), 262–268.
54. Yildiz, Z.; Uzun, H., Prediction of gas storage capacities in metal organic frameworks using artificial neural network. *Micropor Mesopor Mat* **2015**, 208, 50-54.
55. McDonald, T. M.; Mason, J. A.; Kong, X. Q.; Bloch, E. D.; Gygi, D.; Dani, A.; Crocella, V.; Giordanino, F.; Odoh, S. O.; Drisdell, W. S.; Vlaisavljevich, B.; Dzubak, A. L.; Poloni, R.; Schnell, S. K.; Planas, N.; Lee, K.; Pascal, T.; Wan, L. W. F.; Prendergast, D.; Neaton, J. B.; Smit, B.; Kortright, J. B.; Gagliardi, L.; Bordiga, S.; Reimer, J. A.; Long, J. R., Cooperative insertion of CO₂ in diamine-appended metal-organic frameworks. *Nature* **2015**, 519 (7543), 303-+.
56. Valenzano, L.; Civalleri, B.; Chavan, S.; Palomino, G. T.; Arean, C. O.; Bordiga, S., Computational and Experimental Studies on the Adsorption of CO, N₂, and CO₂ on Mg-MOF-74. *J Phys Chem C* **2010**, 114 (25), 11185-11191.
57. Valenzano, L.; Civalleri, B.; Sillar, K.; Sauer, J., Heats of Adsorption of CO and CO₂ in Metal-Organic Frameworks: Quantum Mechanical Study of CPO-27-M (M = Mg, Ni, Zn). *J Phys Chem C* **2011**, 115 (44), 21777-21784.
58. Lee, K.; Howe, J. D.; Lin, L. C.; Smit, B.; Neaton, J. B., Small-Molecule Adsorption in Open-Site Metal-Organic Frameworks: A Systematic Density Functional Theory Study for Rational Design. *Chem Mater* **2015**, 27 (3), 668-678.
59. Lopez, M. G.; Canepa, P.; Thonhauser, T., NMR study of small molecule adsorption in MOF-74-Mg. *J Chem Phys* **2013**, 138 (15).
60. Chen, D.-L.; Shang, H.; Zhu, W.; Krishna, R., Transient breakthroughs of CO₂/CH₄ and C₃H₆/C₃H₈ mixtures in fixed beds packed with Ni-MOF-74 (Reprinted from Journal of Chemical Engineering Science, vol 117C, Pg 407-415, 2014). *Chem Eng Sci* **2015**, 124, 109-117.
61. Ma, H.; Ren, H.; Meng, S.; Sun, F.; Zhu, G., Novel Porphyrinic Porous Organic Frameworks for High Performance Separation of Small Hydrocarbons. *Scientific Reports* **2013**, 3.
62. Bloch, E. D.; Herm, Z. R.; Geier, S. J.; Mason, J. A.; Queen, W. L.; Hudson, M. R.; Wiers, B. M.; Zadrozny, J. M.; Brown, C. M.; Krishna, R.; Long, J. R., Hydrocarbon separations in metal-organic frameworks. *Abstr Pap Am Chem S* **2013**, 245.
63. Verma, P.; Xu, X. F.; Truhlar, D. G., Adsorption on Fe-MOF-74 for C₁-C₃ Hydrocarbon Separation. *J Phys Chem C* **2013**, 117 (24), 12648-12660.
64. Kim, H.; Park, J.; Jung, Y., The binding nature of light hydrocarbons on Fe/MOF-74 for gas separation. *Phys Chem Chem Phys* **2013**, 15 (45), 19644-50.
65. R. Dovesi, V. R. S., C. Roetti, R. Orlando, C. M. Zicovich-Wilson, F. Pascale, B. Civalleri, K. Doll, N. M. Harrison, I. J. Bush, P. D'Arco, M. Llunell, M. Causà and Y. Noël, CRYSTAL14 User's Manual (University of Torino, Torino . **2014**.
66. Giannozzi, P.; Cavazzoni, C., Large-scale computing with Quantum ESPRESSO. *Nuovo Cimento C* **2009**, 32 (2), 49-52.
67. Jones, R. O., Density functional theory: Its origins, rise to prominence, and future. *Rev Mod Phys* **2015**, 87 (3), 897-923.

68. Born. M; Oppenheimer, J. R., *Annalen der Physik* **1927**, 389 (20), 457-484.
69. Ostlund, A. S. a. N. S., *Modern Quantum Chemistry: Introduction to Advanced Electronic Structure Theory*. MacMillan, New York: 1982.
70. Slater, J. C., *Quantum Theory of Molecules and Solids*. McGraw-Hill: New York, 1974; Vol. 4.
71. Sham, W. K. a. L. J., Self-Consistent Equations Including Exchange and Correlation Effects. *American Physical Society* **1965**, 140 (A1133).
72. Parr, R. G. Y., Weitao, *Density-Functional Theory of Atoms and Molecules*. Oxford University Press: 1994.
73. Griffiths, D. J., *Introduction to Quantum Mechanics*. Prentice Hall: Upper Saddle River, New Jersey, 1995.
74. Becke, A. D., A new mixing of Hartree–Fock and local density-functional theories. *J Chem Phys* **1992**, 98 (1372).
75. Hughes, R. I. G., Theoretical Practice: the Bohm-Pines Quartet. *Perspectives on Science* **2006**, 14 (4), 457-524.
76. Grossman, J. C.; Mitas, L.; Raghavachari, K., Structure and stability of molecular carbon: Importance of electron correlation. *Phys Rev Lett* **1995**, 75 (21), 3870-3873.
77. A Zupan, P. B., K Schwarz, JP Perdew, Pressure-induced phase transitions in solid Si, SO₂ and Fe: Performance of local-spin-density and generalized-gradient-approximation density functionals. *Phys. Rev. B* **1998**, 58 (11266).
78. Hammer, B.; Scheffler, M.; Jacobsen, K. W.; Norskov, J. K., Multidimensional Potential-Energy Surface for H₂ Dissociation over Cu(111). *Phys Rev Lett* **1994**, 73 (10), 1400-1403.
79. E. Penev, P. K., and M. Scheffler, Effect of the cluster size in modeling the H₂ desorption and dissociative adsorption on Si(001). *J Chem Phys* **1999**, 110 (3986).
80. John P. Perdew, A. R., and Jianmin Tao, Prescription for the design and selection of density functional approximations: More constraint satisfaction with fewer fits. *J Chem Phys* **2005**, 123 (062201).
81. Grabo, T.; Gross, E. K. U., The optimized effective potential method of density functional theory: Applications to atomic and molecular systems. *Int J Quantum Chem* **1997**, 64 (1), 95-110.
82. Stadele, M.; Moukara, M.; Majewski, J. A.; Vogl, P.; Gorling, A., Exact exchange Kohn-Sham formalism applied to semiconductors. *Phys Rev B* **1999**, 59 (15), 10031-10043.
83. Becke, A. D., A new inhomogeneity parameter in density-functional theory. *J Chem Phys* **1998**, 109 (2092).
84. Becke, A. D., Density-Functional Thermochemistry .3. The Role of Exact Exchange. *J Chem Phys* **1993**, 98 (7), 5648-5652.
85. Lee, C. T.; Yang, W. T.; Parr, R. G., DEVELOPMENT OF THE COLLE-SALVETTI CORRELATION-ENERGY FORMULA INTO A FUNCTIONAL OF THE ELECTRON-DENSITY. *Phys Rev B* **1988**, 37 (2), 785-789.
86. Hammer, B.; Hansen, L. B.; Norskov, J. K., Improved adsorption energetics within density-functional theory using revised Perdew-Burke-Ernzerhof functionals. *Phys Rev B* **1999**, 59 (11), 7413-7421.
87. Perdew, J. P.; Ernzerhof, M.; Burke, K., Rationale for mixing exact exchange with density functional approximations. *J Chem Phys* **1996**, 105 (22), 9982-9985.
88. Zhao, Y.; Truhlar, D. G., The M06 suite of density functionals for main group thermochemistry, thermochemical kinetics, noncovalent interactions, excited states, and

- transition elements: two new functionals and systematic testing of four M06-class functionals and 12 other functionals. *Theor Chem Acc* **2008**, *120* (1-3), 215-241.
89. Jensen, F., Atomic orbital basis sets. *Wires Comput Mol Sci* **2013**, *3* (3), 273-295.
 90. Boys, S. F.; Bernardi, F., The calculation of small molecular interactions by the differences of separate total energies. Some procedures with reduced errors (Reprinted from *Molecular Physics*, vol 19, pg 553-566, 1970). *Molecular Physics* **2002**, *100* (1), 65-73.
 91. Pack, H. J. M. a. J. D., Special points for Brillouin-zone integrations. *Phys. Rev. B* **1976**, *13*, 5188.
 92. Schwerdtfeger, P., The Pseudopotential Approximation in Electronic Structure Theory. *Chemphyschem* **2011**, *12* (17), 3143-3155.
 93. Hamann, D. R.; Schluter, M.; Chiang, C., Norm-Conserving Pseudopotentials. *Phys Rev Lett* **1979**, *43* (20), 1494-1497.
 94. David, G., The Soft and the Hard. *Contracept Fertil S* **1990**, *18* (1), 11-14.
 95. Grimme, S., Semiempirical GGA-type density functional constructed with a long-range dispersion correction. *J Comput Chem* **2006**, *27* (15), 1787-1799.
 96. M. Dion, H. R., E. Schröder, D. C. Langreth, and B. I. Lundqvist, Van der Waals Density Functional for General Geometries. *Phys. Rev. Lett.* **2005**, *92* (24).
 97. Witte, J.; Mardirossian, N.; Neaton, J. B.; Head-Gordon, M., Assessing DFT-D3 Damping Functions Across Widely Used Density Functionals: Can We Do Better? *J Chem Theory Comput* **2017**, *13* (5), 2043-2052.
 98. Zhang, Y. a. Y., Weitao, Comment on ``Generalized Gradient Approximation Made Simple. *Phys. Rev. Lett.* **1998**, *80* (4).
 99. Kyuho Lee, É. D. M., Lingzhu Kong, Bengt I. Lundqvist, and David C. Langreth, Higher-accuracy van der Waals density functional. *Phys. Rev. B* **2010**, *82* (8).
 100. Perdew, J. P. a. Y., Wang, Accurate and simple density functional for the electronic exchange energy: Generalized gradient approximation. *Phys. Rev. B* **1986**, *33* (12).
 101. Pascale, F.; Zicovich-Wilson, C. M.; Gejo, F. L.; Civalieri, B.; Orlando, R.; Dovesi, R., The calculation of the vibrational frequencies of crystalline compounds and its implementation in the CRYSTAL code. *J Comput Chem* **2004**, *25* (6), 888-897.
 102. Zicovich-Wilson, C. M.; Torres, F. J.; Pascale, F.; Valenzano, L.; Orlando, R.; Dovesi, R., Ab initio simulation of the IR spectra of pyrope, grossular, and andradite. *J Comput Chem* **2008**, *29* (13), 2268-2278.
 103. H. Jónsson, G. M., K. W. Jacobsen, *Nudged elastic band method for finding minimum energy paths of transitions, in Classical and Quantum Dynamics in Condensed Phase Simulations, Ed. B. J. Berne, G. Ciccotti and D. F. Coker, . World Scientific: 1998.*
 104. Tauchen, G., Finite State Markov-Chain Approximations to Univariate and Vector Autoregressions. *Econ Lett* **1986**, *20* (2), 177-181.
 105. Jónsson, G. H. a. H., A climbing image nudged elastic band method for finding saddle points and minimum energy paths. *J. Chem. Phys.* **2000**, *113*, 9901-9904.
 106. Jónsson, G. H. a. H., Improved tangent estimate in the nudged elastic band method for finding minimum energy paths and saddle points. *J. Chem. Phys.* **2000**, *113*, 9978-9985.

107. Gallo, M.; Glossman-Mitnik, D., Fuel Gas Storage and Separations by Metal-Organic Frameworks: Simulated Adsorption Isotherms for H₂ and CH₄ and Their Equimolar Mixture. *J Phys Chem C* **2009**, *113* (16), 6634-6642.
108. Civalieri, B.; Zicovich-Wilson, C. M.; Valenzano, L.; Ugliengo, P., B3LYP augmented with an empirical dispersion term (B3LYP-D*) as applied to molecular crystals (vol 10, pg 405, 2008). *Crystengcomm* **2008**, *10* (11), 1693-1693.
109. Weigend, F.; Ahlrichs, R., Balanced basis sets of split valence, triple zeta valence and quadruple zeta valence quality for H to Rn: Design and assessment of accuracy. *Phys Chem Chem Phys* **2005**, *7* (18), 3297-3305.
110. Li, B.; Wen, H. M.; Wang, H. L.; Wu, H.; Tyagi, M.; Yildirim, T.; Zhou, W.; Chen, B. L., A Porous Metal-Organic Framework with Dynamic Pyrimidine Groups Exhibiting Record High Methane Storage Working Capacity. *Journal of the American Chemical Society* **2014**, *136* (17), 6207-6210.
111. Caskey, S. R.; Wong-Foy, A. G.; Matzger, A. J., Phase selection and discovery among five assembly modes in a coordination polymerization. *Inorg Chem* **2008**, *47* (17), 7751-7756.
112. Shriver, D. F. A., P. W, *Inorganic Chemistry*. Oxford University Press: 1999.
113. Degaga, G. D.; Valenzano, L., Part I: C-2-C-4 hydrocarbons separation addressed via molecular cluster models carved out from periodic MOF-74-Mg/Zn structures. *Chem Phys Lett* **2016**, *660*, 313-319.
114. R. Dovesi, R. O., A. Erba, C. M. Zicovich-Wilson, B. Civalieri, S. Casassa, L. Maschio, M. Ferrabone, M. De La Pierre, P. D'Arco, Y. Noel, M. Causa, M. Rerat, B. Kirtman. , 2014. *Int. J. Quantum Chem.* *114*, 1287.
115. Dietzel, P. D.; Johnsen, R. E.; Fjellvag, H.; Bordiga, S.; Groppo, E.; Chavan, S.; Blom, R., Adsorption properties and structure of CO₂ adsorbed on open coordination sites of metal-organic framework Ni₂(dhtp) from gas adsorption, IR spectroscopy and X-ray diffraction. *Chem Commun (Camb)* **2008**, (41), 5125-7.
116. Bao, Z.; Alnemrat, S.; Yu, L.; Vasiliev, I.; Ren, Q.; Lu, X.; Deng, S., Adsorption of ethane, ethylene, propane, and propylene on a magnesium-based metal-organic framework. *Langmuir* **2011**, *27* (22), 13554-62.
117. Geier, S. J.; Mason, J. A.; Bloch, E. D.; Queen, W. L.; Hudson, M. R.; Brown, C. M.; Long, J. R., Selective adsorption of ethylene over ethane and propylene over propane in the metal-organic frameworks M-2(dobdc) (M = Mg, Mn, Fe, Co, Ni, Zn). *Chemical Science* **2013**, *4* (5), 2054-2061.
118. Wu, H.; Zhou, W.; Yildirim, T., High-capacity methane storage in metal-organic frameworks M₂(dhtp): the important role of open metal sites. *J Am Chem Soc* **2009**, *131* (13), 4995-5000.
119. Shannon, R. D., Revised effective ionic radii and systematic studies of interatomic distances in halides and chalcogenides. *Acta Crystallographica Section A* **1976**, *32*, 751-767.
120. He, Y. B.; Krishna, R.; Chen, B. L., Metal-organic frameworks with potential for energy-efficient adsorptive separation of light hydrocarbons. *Energy & Environmental Science* **2012**, *5* (10), 9107-9120.
121. Xiang, S.; Zhou, W.; Zhang, Z.; Green, M. A.; Liu, Y.; Chen, B., Open metal sites within isostructural metal-organic frameworks for differential recognition of acetylene and extraordinarily high acetylene storage capacity at room temperature. *Angew Chem Int Ed Engl* **2010**, *49* (27), 4615-8.

122. Wu, D.; Navrotsky, A., Thermodynamics of metal-organic frameworks. *J Solid State Chem* **2015**, 223, 53-58.
123. Sumida, K.; Rogow, D. L.; Mason, J. A.; McDonald, T. M.; Bloch, E. D.; Herm, Z. R.; Bae, T. H.; Long, J. R., Carbon dioxide capture in metal-organic frameworks. *Chem Rev* **2012**, 112 (2), 724-81.
124. Suh, M. P.; Park, H. J.; Prasad, T. K.; Lim, D. W., Hydrogen storage in metal-organic frameworks. *Chem Rev* **2012**, 112 (2), 782-835.
125. Li, Y.; Yang, R. T., Gas adsorption and storage in metal-organic framework MOF-177. *Langmuir* **2007**, 23 (26), 12937-44.
126. Low, J. J.; Benin, A. I.; Jakubczak, P.; Abrahamian, J. F.; Faheem, S. A.; Willis, R. R., Virtual high throughput screening confirmed experimentally: porous coordination polymer hydration. *J Am Chem Soc* **2009**, 131 (43), 15834-42.
127. Greathouse, J. A.; Allendorf, M. D., The interaction of water with MOF-5 simulated by molecular dynamics. *J Am Chem Soc* **2006**, 128 (33), 10678-9.
128. Saha, D.; Deng, S. G., Structural Stability of Metal Organic Framework MOF-177. *J Phys Chem Lett* **2010**, 1 (1), 73-78.
129. G. D. Degaga, L. V., Part II: quantum mechanical prediction of heats of adsorption for C₂-C₄ hydrocarbons in MOF-74-Mg/Zn periodic structures. *Chem. Phys. Lett.* **2017**.
130. Duan, X.; Zhang, Q.; Cai, J. F.; Cui, Y. J.; Wu, C. D.; Yang, Y.; Qian, G. D., A new microporous metal-organic framework with potential for highly selective separation methane from acetylene, ethylene and ethane at room temperature. *Micropor Mesopor Mat* **2014**, 190, 32-37.
131. Chavan, S. M.; Shearer, G. C.; Bloch, E.; Bordiga, S., Acetylene Adsorption on CPO-27-M Metal-Organic Frameworks (M=Fe, Co and Ni). *Chemphyschem* **2012**, 13 (2), 445-448.
132. Degaga, G. D.; Valenzano, L., Part II: Quantum mechanical prediction of heats of adsorption for C-2-C-4 hydrocarbons in MOF-74-Mg/Zn periodic structures. *Chem Phys Lett* **2017**, 682, 168-174.
133. Tan, K.; Nijem, N.; Canepa, P.; Gong, Q.; Li, J.; Thonhauser, T.; Chabal, Y. J., Stability and Hydrolyzation of Metal Organic Frameworks with Paddle-Wheel SBUs upon Hydration. *Chem Mater* **2012**, 24 (16), 3153-3167.
134. Nijem, N.; Canepa, P.; Kong, L. Z.; Wu, H. H.; Li, J.; Thonhauser, T.; Chabal, Y. J., Spectroscopic characterization of van der Waals interactions in a metal organic framework with unsaturated metal centers: MOF-74-Mg. *J Phys-Condens Mat* **2012**, 24 (42).
135. Kennedy, A. J.; Valenzano, L., Computational prediction of the behavior of MOF-74 under hydrated conditions. *Abstr Pap Am Chem S* **2012**, 243.
136. London., F., *Trans. Faraday. Soc* **1937**, (33).
137. Schuchardt, K. L.; Didier, B. T.; Elsethagen, T.; Sun, L. S.; Gurumoorthi, V.; Chase, J.; Li, J.; Windus, T. L., Basis set exchange: A community database for computational sciences. *J Chem Inf Model* **2007**, 47 (3), 1045-1052.
138. Scott, A. P.; Radom, L., Harmonic vibrational frequencies: An evaluation of Hartree-Fock, Moller-Plesset, quadratic configuration interaction, density functional theory, and semiempirical scale factors. *J Phys Chem-Us* **1996**, 100 (41), 16502-16513.
139. Baranek, P.; Lichanot, A.; Orlando, R.; Dovesi, R., Structural and vibrational properties of solid Mg(OH)(2) and Ca(OH)(2) - performances of various hamiltonians. *Chem Phys Lett* **2001**, 340 (3-4), 362-369.

140. Baranek, P.; Zicovich-Wilson, C. M.; Roetti, C.; Orlando, R.; Dovesi, R., Well localized crystalline orbitals obtained from Bloch functions: The case of KNbO₃. *Phys Rev B* **2001**, *64* (12).
141. Zicovich-Wilson, C. M.; Dovesi, R.; Saunders, V. R., A general method to obtain well localized Wannier functions for composite energy bands in linear combination of atomic orbital periodic calculations. *J Chem Phys* **2001**, *115* (21), 9708-9719.
142. Zicovich-Wilson, C. M.; Bert, A.; Roetti, C.; Dovesi, R.; Saunders, V. R., Characterization of the electronic structure of crystalline compounds through their localized Wannier functions. *J Chem Phys* **2002**, *116* (3), 1120-1127.
143. Noel, Y.; Zicovich-Wilson, C. M.; Civalleri, B.; D'Arco, P.; Dovesi, R., Polarization properties of ZnO and BeO: An ab initio study through the Berry phase and Wannier functions approaches. *Phys Rev B* **2002**, *65* (1).
144. Valenzano, L., In progress **2017**.
145. Hirota, E., Anharmonic Potential Function and Equilibrium Structure of Methane. *J Mol Spectrosc* **1979**, *77* (2), 213-221.
146. L.M. Sverdlov, M. A. K., E. P. Krainov, *Vibrational Spectra of Polyatomic Molecules*. Wiley: New York, 1974.
147. Kuchitsu, K., *Structure of Free Polyatomic Molecules - Basic Data*. Springer: Berlin, 1998.
148. Herzberg, G., *Electronic spectra and electronic structure of polyatomic molecules*. Van Nostrand: New York, 1966.
149. Wu, T. Y., *Vibrational Spectra and Structure of Polyatomic Molecules*. National University of Peking: National University of Peking, Kun-Ming, China,, 1939.
150. Database, R. D. J. I. N. C. C. C. a. B., **2016**, *101*.
151. D Van Lerberghe, I. W., JL Duncan, High-Resolution Infrared Spectrum and Rotational Constants for Ethylene-H₄. *J Mol Spectrosc* **1972**, (42), 251-273.
152. Ugliengo, P., D. Viterbo and G. Chiari, MOLDRAW: Molecular graphics on a personal computer. . *Zeitschrift für Kristallographie-Crystalline Materials* **2010**, *208* (2), 383.
153. G. D. Degaga, L. V., The Study of IR Shifts of Adsorbed Small Hydrocarbon Molecules in MOF-74-Mg/Zn **2017**.
154. Wimmer, E.; Wolf, W.; Sticht, J.; Saxe, P.; Geller, C. B.; Najafabadi, R.; Young, G. A., Temperature-dependent diffusion coefficients from ab initio computations: Hydrogen, deuterium, and tritium in nickel. *Phys Rev B* **2008**, *77* (13).
155. Brauer, E.; Doerr, R.; Gruner, R.; Rauch, F., A Nuclear-Physics Method for the Determination of Hydrogen Diffusion-Coefficients. *Corros Sci* **1981**, *21* (6), 449-457.
156. Wolverton, C.; Ozolins, V.; Asta, M., Hydrogen in aluminum: First-principles calculations of structure and thermodynamics. *Phys Rev B* **2004**, *69* (14).
157. Huxford, R. C.; Della Rocca, J.; Lin, W. B., Metal-organic frameworks as potential drug carriers. *Curr Opin Chem Biol* **2010**, *14* (2), 262-268.
158. Stallmach, F.; Groger, S.; Kunzel, V.; Karger, J.; Yaghi, O. M.; Hesse, M.; Muller, U., NMR studies on the diffusion of hydrocarbons on the metal-organic framework material MOF-5. *Angew Chem Int Ed Engl* **2006**, *45* (13), 2123-6.
159. Friedemann, K.; Stallmach, F.; Karger, J., NMR diffusion and relaxation studies during cement hydration - A non-destructive approach for clarification of the mechanism of internal post curing of cementitious materials. *Cement Concrete Res* **2006**, *36* (5), 817-826.

160. Canepa, P.; Nijem, N.; Chabal, Y. J.; Thonhauser, T., Diffusion of Small Molecules in Metal Organic Framework Materials. *Phys Rev Lett* **2013**, *110* (2).
161. Skoulidas, A. I.; Sholl, D. S., Self-diffusion and transport diffusion of light gases in metal-organic framework materials assessed using molecular dynamics simulations. *J Phys Chem B* **2005**, *109* (33), 15760-8.
162. Ramsahye, N. A.; Gao, J.; Jobic, H.; Llewellyn, P. L.; Yang, Q.; Wiersum, A. D.; Koza, M. M.; Guillerm, V.; Serre, C.; Zhong, C. L.; Maurin, G., Adsorption and Diffusion of Light Hydrocarbons in UiO-66(Zr): A Combination of Experimental and Modeling Tools. *J Phys Chem C* **2014**, *118* (47), 27470-27482.
163. Rosenbach, N.; Jobic, H.; Ghoufi, A.; Devic, T.; Koza, M. M.; Ramsahye, N.; Mota, C. J.; Serre, C.; Maurin, G., Diffusion of Light Hydrocarbons in the Flexible MIL-53(Cr) Metal-Organic Framework: A Combination of Quasi-Elastic Neutron Scattering Experiments and Molecular Dynamics Simulations. *J Phys Chem C* **2014**, *118* (26), 14471-14477.
164. Henkelman, G.; Uberuaga, B. P.; Jonsson, H., A climbing image nudged elastic band method for finding saddle points and minimum energy paths. *J Chem Phys* **2000**, *113* (22), 9901-9904.
165. P. Giannozzi, S. B., N. Bonini, M. Calandra, R. Car,; C. Cavazzoni, D. C., G. L. Chiarotti, M. Cococcioni,; I. Dabo, A. D. C., S. Fabris, G. Fratesi, S.; de Gironcoli, R. G., U. Gerstmann, C. Gougoussis,; A. Kokalj, M. L., L. Martin-Samos, N. Marzari,; F. Mauri, R. M., S. Paolini, A. Pasquarello, L.; Paulatto, C. S., S. Scandolo, G. Sclauszero, A.P.; Seitsonen, A. S. P. U., and R. M. Wentzcovitch,, *J. Phys Cond. Mat.* **2009**, *39* (395502).
166. Thonhauser, T.; Cooper, V. R.; Li, S.; Puzder, A.; Hyldgaard, P.; Langreth, D. C., Van der Waals density functional: Self-consistent potential and the nature of the van der Waals bond. *Phys Rev B* **2007**, *76* (12).
167. Dion, M.; Rydberg, H.; Schroder, E.; Langreth, D. C.; Lundqvist, B. I., Van der Waals density functional for general geometries. *Phys Rev Lett* **2004**, *92* (24).
168. Dion, M.; Rydberg, H.; Schroder, E.; Langreth, D. C.; Lundqvist, B. I., Van der waals density functional for general geometries (vol 92, art no 246401, 2004). *Phys Rev Lett* **2005**, *95* (10).
169. Langreth, D. C.; Lundqvist, B. I.; Chakarova-Kack, S. D.; Cooper, V. R.; Dion, M.; Hyldgaard, P.; Kelkkanen, A.; Kleis, J.; Kong, L. Z.; Li, S.; Moses, P. G.; Murray, E.; Puzder, A.; Rydberg, H.; Schroder, E.; Thonhauser, T., A density functional for sparse matter. *J Phys-Condens Mat* **2009**, *21* (8).
170. Ma, H. P.; Ren, H.; Meng, S.; Sun, F. X.; Zhu, G. S., Novel Porphyrinic Porous Organic Frameworks for High Performance Separation of Small Hydrocarbons. *Sci Rep-Uk* **2013**, *3*.
171. al, G. D. D. e., C2-C4 Hydrocarbons Separation Addressed via Molecular Cluster Models Carved Out from Periodic MOF-74-Mg/Zn Structures. *Chem Phys Lett* **2016**.
172. Queen, W. L.; Brown, C. M.; Britt, D. K.; Zajdel, P.; Hudson, M. R.; Yaghi, O. M., Site-Specific CO₂ Adsorption and Zero Thermal Expansion in an An isotropic Pore Network. *J Phys Chem C* **2011**, *115* (50), 24915-24919.
173. Xiang, S. C.; Zhou, W.; Zhang, Z. J.; Green, M. A.; Liu, Y.; Chen, B. L., Open Metal Sites within Isostructural Metal-Organic Frameworks for Differential Recognition of Acetylene and Extraordinarily High Acetylene Storage Capacity at Room Temperature. *Angew Chem Int Edit* **2010**, *49* (27), 4615-4618.
174. Kui Tan, S. Z., Qihan Gong, Yuzhi Gao, Nour Nijem†¹, Jing L, Timo Thonhauser, and Yves J Chabal, Competitive Coadsorption of CO₂ with H₂O, NH₃, SO₂, NO, NO₂,

N₂, O₂, and CH₄ in M-MOF-74 (M = Mg, Co, Ni): The Role of Hydrogen Bonding. *Chem. Mater* **2015**, 27 (6), 2203–2217.